Modelling and Design of an Oscillating Wave Energy Converter

by
Jason Fairhurst

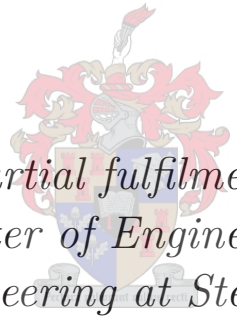

Thesis presented in partial fulfilment of the requirements for the degree of Master of Engineering (Mechanical) in the Faculty of Engineering at Stellenbosch University

Supervisor: Prof J.L. van Niekerk

December 2015

Declaration

By submitting this thesis electronically, I declare that the entirety of the work contained therein is my own, original work, that I am the sole author thereof (save to the extent explicitly otherwise stated), that reproduction and publication thereof by Stellenbosch University will not infringe any third party rights and that I have not previously in its entirety or in part submitted it for obtaining any qualification.

Signature: .....

Date: .....

Abstract

This thesis presents the experimental testing and development of a time-domain simulation model for a wave energy converter based on the principles of an oscillating water column. The device was developed and patented by Stellenbosch University hence the name, Stellenbosch Wave Energy Converter (SWEC). The main objective of this project was to produce a verified and validated simulation model for the Stellenbosch Wave Energy Converter. The device is experimentally tested and modelled in two different configurations, namely the Surface SWEC and the Submerged SWEC. Experimental testing and mathematical modelling contributed to the development of the two simulation models. These models provided a better understanding of the hydrodynamics and thermodynamics associated with the device. The experimental results show that the Surface SWEC achieved a peak conversion efficiency of 26% and a conversion efficiency of 15% at the expected operating conditions. The Submerged SWEC achieved a peak conversion efficiency of 22% and a conversion efficiency of 13% at the expected operating conditions.

The Surface SWEC simulation model predicted the transmissibility of the device with errors which ranged from 0% to 26% with the majority of the errors being less than 10%. Conversion efficiencies predicted by the Surface SWEC model achieved errors which ranged from 0% to 42% with the majority of the errors being less than 10%. The Submerged SWEC model predicted the transmissibility of the device with errors which ranged from 0% to 20% with the majority of the errors being less than 5%. The Submerged SWEC model predicted the conversion efficiency of the device with errors which ranged from 0% to 43% with the majority of the errors being less than 15%.

Opsomming

Hierdie tesis handel oor die proefondervindelike toetsing en ontwikkeling van 'n tyddomeinsimulasiemodel vir 'n golfenergieomsetter wat op die beginsels van 'n ossillerende waterkolom berus. Die toestel is deur die Universiteit Stellenbosch ontwikkel en gepatenteer, vandaar die naam Stellenbosch Golfenergieomsetter, oftewel SWEC. Die hoofoogmerk van hierdie projek was om 'n getoetste en gestaafde simulasiemodel vir die SWEC te skep. Proefondervindelike toetsing en modellering van die toestel het in twee verskillende konfigurasies, naamlik die oppervlak-SWEC en die onderwater-SWEC, plaasgevind. Met behulp van die proefondervindelike toetsing en wiskundige modellering kon twee simulasiemodelle ontwikkel word. Hierdie modelle het 'n beter begrip gebied van die hidro- en termodinamika wat met die toestel verband hou. Die proefondervindelike resultate toon dat die oppervlak-SWEC 'n topomsettingsdoeltreffendheid van 26% en 'n omsettingsdoeltreffendheid van 15% in die verwagte bedryfsomstandighede lewer. Die onderwater-SWEC het 'n topomsettingsdoeltreffendheid van 22% en 'n omsettingsdoeltreffendheid van 13% in die verwagte bedryfsomstandighede behaal.

Die simulasiemodel vir die oppervlak-SWEC het die oordraagbaarheid van die toestel voorspel met foute wat van 0% tot 26% strek, met die meeste foute onder 10%. Die omsettingsdoeltreffendhede wat deur dié model voorspel is, het binne 'n foutgrens van 0% tot 42% geval, met die meeste foute binne 10%. Die model vir die onderwater-SWEC het die oordraagbaarheid van die toestel voorspel met foute wat van 0% tot 20% strek, met die meeste foute onder 5%. Hierdie model het die omsettingsdoeltreffendhede van die toestel binne 'n foutgrens van 0% tot 43% voorspel, met die meeste foute binne 15%.

Acknowledgements

I would like to express my deep gratitude to Professor J.L. Van Niekerk, my research supervisor, for his guidance, detailed critique and interest in this research work.

I would also like to extend my thanks to the technicians of the laboratory of the Mechanical and Civil Engineering Departments of Stellenbosch University for their help throughout the project.

Finally, I wish to thank my family and friends for their support and encouragement throughout my study.

The financial assistance of the Centre of Renewable and Sustainable Energy Studies (CRSES) as well as the National Research Foundation (NRF) towards this research is hereby acknowledged. Opinions expressed and conclusions arrived at, are those of the author and are not necessarily to be attributed to the CRSES and NRF.

Contents

List of Figures

List of Tables

Nomenclature

A	Area
A_c	Cross sectional chamber area
A_d	Area of outlet duct
A_{ocean}	Area of ocean
A_{op}	Orifice plate hole area
B	Damping coefficient
C	Hydrostatic restoring coefficient
C_d	Coefficient of discharge
C_g	Wave group velocity
C_p	Heat capacity at constant pressure
C_s	Speed of sound through air
C_v	Heat capacity at constant volume
D_h	Hydraulic diameter
D_{man}	Manifold diameter
Dis_{ah}	Distance from shore
E	Total energy
E_k	Kinetic energy
E_p	Potential energy
F	Force
F_a	Added mass force
F_d	Drag force
F_{FK}	Froude - Krylov force force
$F_{\Delta p}$	Force due to pressure differential
H	Wave height
I	Invariant integral number for added mass
K	Loss coefficient
K_c	Contraction loss coefficient
K_e	Expansion loss coefficient
K_f	Friction loss coefficient
K_{op}	Orifice plate loss coefficient
K_x	Undetermined loss coefficient
L_{arm}	Chamber arm length
L_d	Orifice duct length
L_{eq}	Equivalent length
L_{mod}	Module length
L_r	Dimension scale

M_a	Added mass
M_c	Water mass in the chamber
N_{ch}	Number of chambers
N_{mod}	Number of modules
P	Power
P_w	Wave power
P_{conv}	Converted power
P_r	Power scale
Q	Heat
R^2	Measure of good-fit for a regression line
R^*	Specific gas constant
T	Wave period
U	Velocity
U_d	Outlet duct velocity
U_0	Characteristic flow velocity
V	Volume
V_{aux}	Auxiliary volume
V_c	Chamber volume
$\dot{V}$	Volumetric flow rate
$\dot{V}_d$	Volumetric flow rate through orifice duct
W	Work
Z_{ch}	Chamber lip length
Z_{cho}	Depth of chamber opening
Z_{sub}	Chamber submergence

a	Wave amplitude
a_i	Inner chamber surface displacement amplitude
a'	Chamber length
b	Wave crest width
b'	Chamber width
c	Wave phase velocity
c_s	Speed of sound through air
ce_{err}	Conversion efficiency error
d_d	Orifice duct diameter
d_1	Submergence
d_2	Draught
e_{si}	Specific internal energy
f_H	Helmholtz resonance frequency
f	Friction factor
g	Gravitational acceleration constant
g_0	Characteristic external field
h	Water depth
h_L	Head loss
h_a	Air height in chamber
h_{a0}	Static air height in chamber
k	Wave number

l_0	Characteristic length
m	Mass
m_{aux}	Mass in the auxiliary volume
m_c	Air mass in the chamber
$\dot{m}$	Mass flow rate
$\dot{m}_d$	Mass flow rate through orifice duct
Δm_{aux}	Change in mass in the auxiliary chamber
p	Pressure
p_c	Chamber pressure
p_{atm}	Atmospheric pressure
p_{aux}	Auxiliary pressure
p_r	Pressure scale
p_{wave}	Hydrodynamic pressure at the bottom of water column
Δp	Difference in pressure between chamber and auxiliary volume or atmosphere
t	Time
$t_{err}\%$	Transmissibility error
t_r	Time scale
u	Particle velocity in x plane
u_i	Fluid particle velocity
v_o	Voltage
w	Particle velocity in z plane
z	Water level displacement inside chamber

α	Simplification substitution for equation of motion
β	Simplification substitution for equation of motion
γ	Heat capacity ratio
ϵ	Surface roughness
η	Surface elevation
κ	Wave number
λ	Wavelength
ρ_a	Density of air
ρ_w	Density of water
τ_{atm}	Atmospheric temperature
τ_{aux}	Auxiliary volume temperature
τ_c	Chamber temperature
θ	Chamber angle
ϕ	Wave phase shift
ω	Angular frequency
ζ	Product of air density and gravitational constant

BNC	Bayonet Neill-Concelman
CEM	Coastal Engineering Manual
CSIR	Council for Scientific and Industrial Research
DAQ	Data acquisition
CRSES	Centre for Renewable and Sustainable Energy Studies

EH	Endress & Hauser
HBM	Hottinger Baldwin Messetechnik
LIMPET	Land Installed Marine Power Energy Transmitter
OWC	Oscillating water column
OWSC	Oscillating Wave Surge Converter
PRDW	Prestedge Retief Dresner Wijnberg
PTO	Power take off
RMSE	Root mean square error
SWEC	Stellenbosch Wave Energy Converter
SWL	Still water level
WEC	Wave energy converter

Chapter 1

Introduction

Up until the twenty-first century global electricity needs have been predominantly met by converting fossil fuels into electricity. This process has proved to be detrimental to the environment as well as unsustainable. South Africa is an example of a country that meets the majority of its electricity needs through the use of fossil fuels and is suffering due to an insufficient supply of power. The lack of power has resulted in rolling blackouts which are extremely detrimental to the country's inhabitants and economy. Thus, there is an urgent need for power from alternative, sustainable and renewable energy sources. Renewable energy is defined as energy sources which are naturally replenished on a human time-scale. This study will focus on ocean waves, which have been proved to be a source of renewable energy.

The global wave power resource is estimated at 2 teraWatt (TW), with the United Kingdom's (UK's) wave power potential ranging from 7-10 gigaWatt (GW). To put this in perspective, the UK's total grid capacity is about 80 GW, this means that up to 15% of the UK's peak electricity could be supplied using wave energy (Drew, Plummer & Sahinkaya, 2009).

The south west coast of South Africa is roughly 700 km long, with the southern tip of this coastline recording an average wave power of up to 40 kiloWatt (kW) per metre wave front (Joubert, 2008). If this energy could be efficiently harnessed it could provide major support to South Africa's electrical grid. The Stellenbosch Wave Energy Converter (SWEC) provides a means of converting this renewable source into electrical energy.

Many different wave energy converter (WEC) concepts and designs exist throughout the world, although very few have been implemented and connected to the grid. This is due to challenges which exist in three main aspects, namely the survivability, the conversion efficiency and the capital cost. In order for a WEC to be implemented it must showcase the ability to effectively convert wave energy into electrical energy as well as be able to survive in the harsh ocean environment.

This project intends on investigating the performance of the SWEC with experimental testing as well as accurately modelling the hydrodynamics and thermodynamics of the device. Various analytical, numerical and experimental approaches are

used in order to develop and verify a reliable simulation model for a single SWEC chamber.

The experimental testing and mathematical modelling will contribute to defining the viability of the device as well as providing a better understanding of the fluid dynamics present in the SWEC and oscillating water columns (OWCs) in general. This understanding is critical for the development and implementation of wave energy conversion devices such as the SWEC.

1.1 Background

The aim of this section is to provide background on the SWEC device. The section starts by giving a detailed explanation of the device and how it works. It then goes on to present a study history of the device. The section concludes with the problem statement, project aim and document layout.

1.1.1 The SWEC

Two different SWEC configurations are modelled in this project, the Surface SWEC and Submerged SWEC configuration. The Submerged SWEC serves as the priority of the study and therefore goes through a more detailed analysis and evaluation procedure. The two configurations are very similar, with the only difference being the water depth in which they operate. Due to these similarities only the Submerged SWEC is introduced in this section.

The Submerged SWEC is made up of two 160 m long submerged arms which are positioned in a 'V' like shape fixed to the sea floor. The arms consist of a number of modules, these modules each have a number of chambers which act as submerged OWCs. The turbine generator unit is vertically attached to the arms at the apex of the 'V', as illustrated in Figure 1.1. The SWEC was designed to operate off the south west coast of South Africa in wave conditions shown in Table 1.1.

As the crest of a wave moves overhead, water is forced into the submerged OWCs. This increases the pressure in the OWC's chamber and forces air into the 'high pressure duct'. As the trough of a wave passes overhead the pressure decreases again and air is sucked out of the 'low pressure duct', see Figure 1.2. Each OWC is connected to the high pressure duct and low pressure duct through one way valves.

Table 1.1: Proposed operating conditions for Submerged SWEC (Ackerman, 2009).

Wave dimension	Value	Unit
Wave height	2	m
Wave period	12.3	s
Wavelength	148.6	m
Water depth	15-20	m

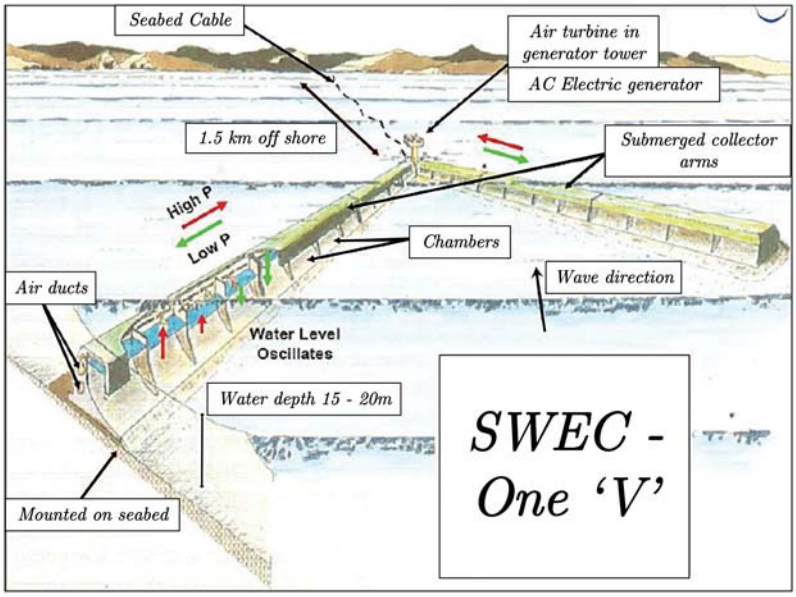

Figure 1.1: Submerged SWEC 'V' adapted from Retief *et al.* (1982).

This results in the low pressure duct staying at a lower pressure than the high pressure duct. The constant pressure differential between the two ducts induces an air flow which drives a turbine and in turn drives a generator. The Submerged SWEC has been designed to absorb only 30% of the wave passing overhead in order not to disrupt the natural motion of the waves to a large degree (Retief, Prestige, Muller, Guestyn & Swart, 1982).

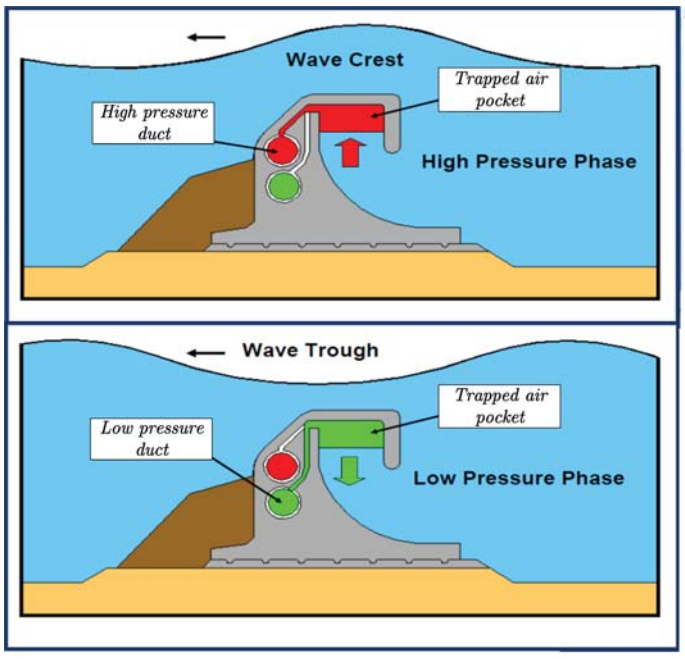

Figure 1.2: Cross section of Submerged SWEC adapted from Retief *et al.* (1982).

1.1.2 Study history of the SWEC

The SWEC concept was invented in the early 1980s by Retief *et al.* (1982). The concept has been developed throughout various studies but there is no document available which summarises the resulting advancements and conclusions to date. This section starts by presenting an overview of what Retief *et al.* (1982) achieved with their work concerning the SWEC concept. Thereafter studies done before 2014 which have drawn conclusions or made advancements relating to the SWEC are presented in a chronological order.

Work carried out prior to 2000

The following information concerning the time line of the SWEC is referenced from written correspondence received from Professor Retief. The development of the SWEC was started by a research group led by Retief *et al.* (1982) from 1983 to 1988 under the sponsorship of the De Beers Chairman's fund, Murray and Roberts and several other funders. The development of the SWEC included the flowing:

- Designing the Submerged SWEC chamber and layout
- Construction and testing of three scale models:
  - Single collector arm of scale 1:100
  - Single chamber model of scale 1:100
  - Complete 'V' array of scale 1:100
- Defining optimal operating conditions for the device

The first scale model was used to gain a better understanding of how exactly the system worked. The second single scale model compartment was tested with the aim of analysing the sensitivity of varying the geometry of a single compartment and also to test its overall design stability. The complete 'V' array was tested under irregular wave conditions in the Council for Scientific and Industrial Research (CSIR) test tank in order to gain a better understanding of how the system would react in irregular sea conditions. No numerical work was carried out on the SWEC prior to 2000. Many assumptions and estimations were made during the design phase of the very first SWEC model. Professor Retief makes the following statement in the written correspondence dated 2014:

> Unfortunately, at the time we knew so little about the potential interaction of angled wave attack with two submerged, pressurised, airflow systems under irregular waves we decided to make a lot of guesses and informal calculations on which the physical model series was based.

In 1989 a conference was held by the sponsors in order to assess the viability of proceeding with the development of the SWEC. The spike in oil prices in 1973 had driven the international effort to utilise ocean energy. The oil prices had stabilised by 1989 and the group of sponsors decided the SWEC was technically viable but

economically impractical. The proposed cost of electricity generated by the SWEC was similar to nuclear power but much more expensive than the very cheap coal fired power which ESKOM was producing at the time. The decision was therefore made to end the development of the SWEC.

In 1997 an international consulting group, Prestedge Retief Dresner Wijnberg (PRDW), picked up the SWEC project when interest in ocean energy started developing again. PRDW then updated the original cost estimates and found that SWEC power cost about the same as wind power at the time.

Work carried out post 2000

The Centre for Renewable and Sustainable Energy Studies (CRSES) was founded at Stellenbosch University in 2006 and continued the SWEC project as part of the ocean energy research. The first of the various studies which concerned the SWEC was a wave energy resource analysis carried out by Joubert (2008). The study presented the wave energy available along the south west coast of South Africa and provided justification for the proposed Submerged SWEC site seen in Figure 2.1.

Ackerman (2009) then carried out a study which attempted to numerically model the airflow system of the Submerged SWEC in order to design an appropriate turbine for the device. Ackerman (2009: 75) states:

> The airflow system numerical simulation model predicted the SWEC performance well up to wave heights of 3 m. The less accurate predictions of the model in larger wave conditions are believed to stem from inaccurate estimations of added mass and damping in these conditions.

The simulation model produced by this study relies heavily on accurate estimations for added mass and damp and becomes inaccurate when the wave height exceeds 3 m. Meyer (2012) carried out an undergraduate investigation on modelling the air and water flow of an OWC. The model results were compared with the results gathered from the testing of a scale model of the Surface SWEC. The accuracy of the model developed was defined as 'limited' and the addition of an auxiliary loss term was required to match experimental and analytical results. Meyer (2012) recommends investigating the non-linear losses due to hydrodynamic behaviour in order to find an accurate term which describes both linear and non-linear losses in the system.

Joubert (2013) carried out a study in which he further developed and adapted the design of the Surface SWEC. A wave modelling procedure was developed to determine the operational conditions and available wave power resource at the selected site. The effect of the floor inclination of the device was investigated and a comparison between the Surface SWEC and a conventional OWC converter was carried out. A numerical model was also developed, Joubert (2013: ii) stated that the "numerical model provided comparable water surface elevations inside the flume and chamber, yet predicted significantly higher internal chamber pressures and overall efficiency". Joubert (2013) concludes by stating that there is a need to better understand the

hydrodynamic characteristics of the shore SWEC as well as the need to improve the numerical and experimental model.

Fairhurst (2013) carried out an undergraduate study which tested the Submerged SWEC experimentally and evaluated the device. The aim of the testing was to define the efficiency of the submerged SWEC device as well as the optimal orientation of the device. The testing produced relevant trends although it did not provide accurate magnitudes or efficiencies due to an aspect of the experimental set-up which was overlooked. This aspect is explained in Section 2.4. The study did however provide a better understanding of the optimal operating conditions and device orientation.

A simulation model was also developed in the attempts to model the airflow in the Submerged SWEC (Fairhurst, 2013). The model predicted the volumetric flow rate in the device to a moderate degree of accuracy but overestimated the pressure differential present in the device. Recommendations were made for a more in-depth analysis on the hydrodynamics and thermodynamics model to be carried out.

There is a general trend present in all the recommendations made in the previously presented studies concerning the SWEC. The trend suggests that there is a need for an improved simulation model of the hydrodynamics and thermodynamics in both the Surface and Submerged SWEC.

1.2 Problem statement, aim of study and project objectives

The problem statement for this project is that past studies have not yet been able to accurately model the hydrodynamics and thermodynamics of the SWEC device. The previously developed models had two main shortcomings. The first is that the models were not able to produce accurate results for wave inputs with high frequencies. The second shortcoming is that an unaccounted-for loss variable was used to match the simulation results to the experimental results.

The aim of this project is to use experimental test data and mathematical modelling techniques to develop two accurate and verified simulation models. One model which describes a single Surface SWEC chamber and another that describes a single Submerged SWEC chamber. The models will be used to gain a better understanding of the energy available to the collector chamber and the ability of the chamber to convert wave power into pneumatic power.

The modelling of the Submerged SWEC chamber serves as the priority of this study but the experimental set-up allowed for the testing of the Surface SWEC configuration as well; moreover, modelling the Surface SWEC layout proved to be an effective and logical step to take before modelling the Submerged SWEC configuration. The second aim of this project is to use the experimental data to make conclusions on the energy conversion ability of the SWEC.

The objectives of this project are summarised below:

- Experimental testing of the Surface SWEC configuration using relevant wave conditions.
- Experimental testing of the Submerged SWEC configuration in various orientations using relevant wave conditions.
- Simulation modelling of both configurations.
- Verification and evaluation of both models.
- Experimentally supported conclusions made on energy conversion efficiency, operating orientation and optimal test conditions.

The term 'conversion efficiency' is used often in this thesis and refers to the ability of a WEC to convert wave power into electrical power. This value is defined by simply dividing the converted power by the power in the incident wave. It is used to evaluate a WEC by predicting the amount of energy which may be converted in a specific wave climate.

1.3 Thesis layout

This section provides more detail on the work carried out for this research project as well as a brief overview on each chapter.

Chapter 2 presents the literature review which was conducted during this research project. The review starts by presenting an investigation which was carried out on the wave energy resource available off the South African coast. It then goes on to explain the basic principles of linear wave theory and introduces various types of WECs. Relevant studies used to derive the mathematical models are summarised and the chapter is concluded with an overview of the existing experimental set-up from the study carried out by Fairhurst (2013).

Chapter 3 explains the experimental testing and processes involved in ensuring that the collected data was accurate, relevant and reliable. The chapter starts by presenting the experimental set-up of both the Surface and Submerged SWEC configurations. The chapter then introduces the SWEC chamber scale model and continues to explain the instrumentation and respective calibrations involved in the experimental process. The chapter concludes with an explanation of how the recording process took place and how the various sensors were used.

Chapter 4 introduces and explains the simulation models developed to describe the two SWEC configurations. First the model which describes the hydrodynamics in the Surface SWEC is fully derived. This is followed by the derivation of state equations which describe the thermodynamics and pneumatics of the system. These derivations are then built on in order to produce state equations which describe the Submerged SWEC behaviour.

Chapter 5 presents a discussion and overview on the simulation and experimental results produced. The thesis is concluded with Chapter 6 which presents various conclusion and recommendations.

Chapter 2

Literature review

The literature review starts with an investigation of the proposed site for the Submerged SWEC. The review then goes on to present the theory describing the formation of wind waves, linear wave theory and wave particle dynamics. Various types of WECs are presented along with an overview of the modelling procedures which are relevant to the SWEC. The chapter concludes with an overview of the existing experimental set-up.

2.1 Wave energy resource analysis

The aim of this section is to investigate the wave power available at the proposed site in order to make a provisional conclusion on the viability of implementing a WEC off the south west coast of South Africa.

The proposed site for the SWEC is shown in Figure 2.1. This site is made up of a 40 km long stretch of coastline. This site has been proposed due to it being directly exposed to the south westerly swells. Retief *et al.* (1982) states that these swells are often totally un-refracted and therefore carry a lot more energy as they have propagated directly to the site from where they were formed. Retief *et al.* (1982: 2547) describes the proposed site as "well instrumented in the past" and that "reliable wave height and direction data is available". An average wave power of about 30 kW/m is apparent near the site, which is conveniently situated near urban growth points (Cape Town and Saldanha). The proposed SWEC array will consist of 154 "V" units with a 770 MW rating and a mean winter capacity of 450 MW.

Joubert (2008) carried out a wave energy resource analysis based on the data recorded by five recording stations all situated along South Africa's coast. The recording stations are situated at Port Nolloth, Slangkop, Cape Point, FA Platform and Durban and can be seen in Figure 2.1. The Port Nolloth, Slangkop and Cape Point recording stations are situated close to the proposed SWEC site, Port Nolloth to the north and the other two stations to the south. It is assumed that the average wave power recorded by these three sites serves as an accurate representation of the wave power available at the proposed site. Joubert (2008) concludes his report with

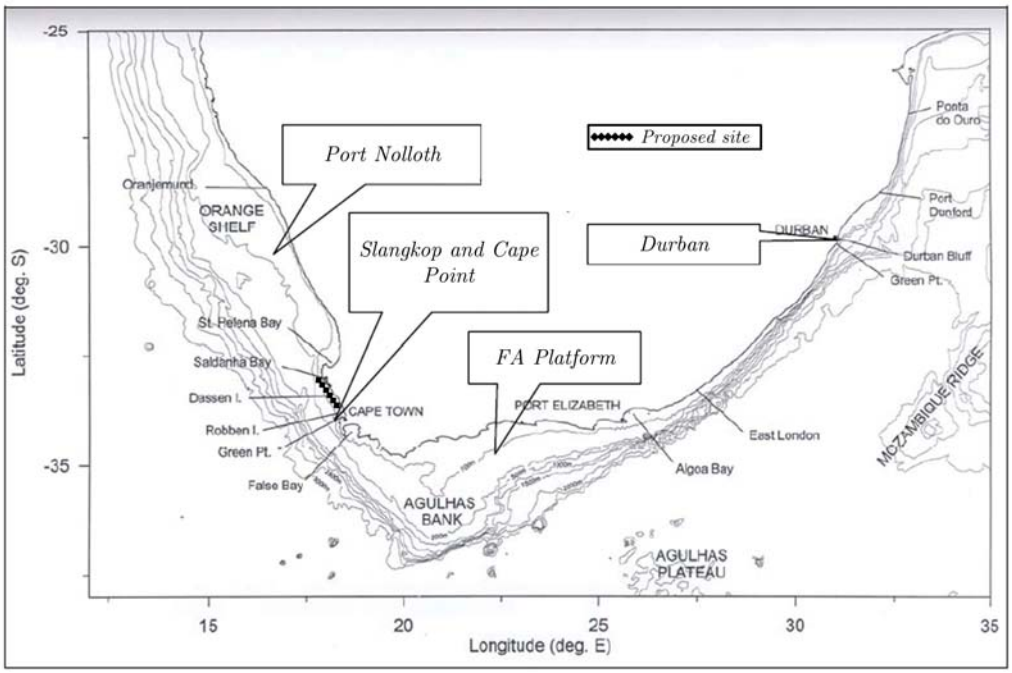

Figure 2.1: Contours of the South African seabed and the distribution of wave recording stations adapted from Westhuysen (2002).

the average wave power for these three recording sites, as can be seen in Table 2.1.

Table 2.1: Average wave power at the three relevant recording sites (Joubert, 2008).

Recording station	Average power (kW/m)
Port Nolloth	23
Slangkop	40
Cape Point	40

The values for average wave power put forward by Joubert (2008) in Table 2.1 support the 30 kW/m stated by Retief *et al.* (1982). The south-west coast of South Africa is about 700 km long stretching from Cape Point to Alexander Bay. A conservative assumption of 25 kW/m is made for the average wave power along the coast, based on this average wave power the total capacity for the South West coast is 17.5 GW. To put this into perspective, the highest ever recorded electricity consumption for South Africa is 36 GW (SAPA, 2012). The suggestion that half of this peak power is continuously available on one third of South Africa's coastline supports the proposal of wave energy conversion for South Africa.

2.2 Wave theory

This section explains how wind waves are formed and the relevant theory describing wave particle dynamics. A good understanding of how waves transfer energy is

required in order to efficiently extract wave energy. In addition, and in order to produce accurate simulation results, an accurate wave input model is required. Linear wave theory is discussed along with the main wave parameters and the equations which describe them.

2.2.1 Formation of waves

The following information is sourced from Garrison (1996). Ocean waves are formed due to three very different, naturally occurring phenomena. The three different wave forms are tidal waves, seismic sea waves (more commonly known as Tsunamis) and wind waves, each wave appropriately named after the phenomenon that forms it. Tidal waves are formed due to the gravitational pull of the moon and the sun on the ocean. Seismic sea waves/Tsunamis are caused by earthquakes beneath the ocean. They travel extremely fast in open water, have significant height in shallow water, and are devastating to the area which they propagate through. Wind waves are by far the most common type of waves found at sea. These waves are formed by gusts of wind blowing over the surface of the ocean. Literature describing the formation, the hydrodynamics and the power of wind waves is presented.

Many theories have been developed in a effort to describe the formation of wind waves and the transfer of energy from the atmosphere to the ocean's surface. The presently accepted theory involves two distinct mechanisms, named after their proponents, Phillips and Miles.

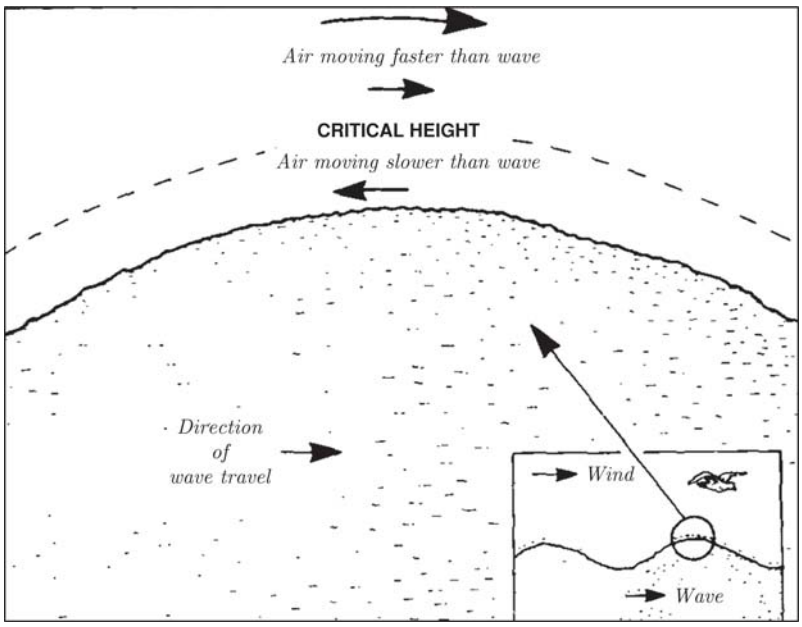

Figure 2.2: The 'critical height' mechanism adapted from Miles (1957).

Phillips (1957) developed a theory on the formation of ripples on a flat sea. His theory describes the manner in which turbulent wind agitates the sea's surface and eventually generates waves. Turbulent flow involves a randomly fluctuating velocity field superimposed on a mean flow. The fluctuations present in the velocity field

give rise to fluctuating stresses which act on the air-water interface. These stresses act in both the tangential and normal directions. The fluctuating normal stress or pressure acts as a forcing term. The growth of waves is a result of this forcing term matching a mode of vibration in the capillary-gravity waves. The matching frequency of the forcing term and the mode of the gravity wave leads to constructive interference and to resonance causing the amplitude of the wave to grow.

Unfortunately, this mechanism doesn't allow for the ripples to grow into larger waves. Even more disconcerting is the fact that in order to generate waves, this concept requires much larger pressure fluctuations than are observed at sea. Phillips (1957) explains how the ripples are formed but his concept is unable to describe the growth of wind waves. Miles (1957) continued the work of Phillips (1957) and developed a complicated theory based on the existence of a 'critical height'. Once ripples are formed (explained by Phillips (1957)) the air-water interface is endowed with surface roughness. Miles (1957) explains the interaction of the turbulent mean flow with the established ripples, or micro-waves.

Frictional forces cause the air, which is in contact with the sea, to move at the same speed as the water. As the water particles are not moving as fast as the wave itself, they are only transferring energy to the next particle, the air above the water is actually moving slower than the wave but in the same direction. The critical height marks a distance at which the wind speed is moving as fast as the wave, and faster than the wave when moving further upwards from the critical height. This interaction is shown in Figure 2.2.

Miles (1957) states that the force exerted on the sea by the wind depends on the structure of the air flow at the critical height. As the turbulent air flows over an existing wave, a low pressure is created on the leeward face and a high pressure is created on the windward face of the wave. The waves then deform due to the pressure differential, the continuous movement of the wind creates another similar pressure differential and the cycle repeats. This is the process required in order to transfer the energy from the wind to the waves. As the wind continues to blow the waves will continue to grow until equilibrium has been reached. The size and power of wind waves depend on the wind strength, duration and fetch (the distance over which the wind blows). See Figure 2.3 for a graphical display of the Miles-Phillips Mechanism.

2.2.2 Linear wave theory

Linear wave theory was developed by Airy (1845) and has been the basic theory used to mathematically describe small-amplitude surface gravity waves for the last 150 years. Water waves are of course non-linear, higher order wave theories which are more accurate at describing these waves do exist but are not used in this thesis for simplicities sake. McCormick (1981) presents the expression which describe a non-linear wave. Waves are classified as 'small amplitude' when the wave height is very small compared to the wavelength and water depth. One of the key assumptions in linear wave theory is that the motion of the water particles is irrotational. Flow

is said to be irrotational when the vorticity has magnitude zero everywhere, in this case it means that the water particles do not spin around their own axis. This assumption allows for the velocity potential equation to be used to describe the velocity of the water particles (Holthuijsen, 2007).

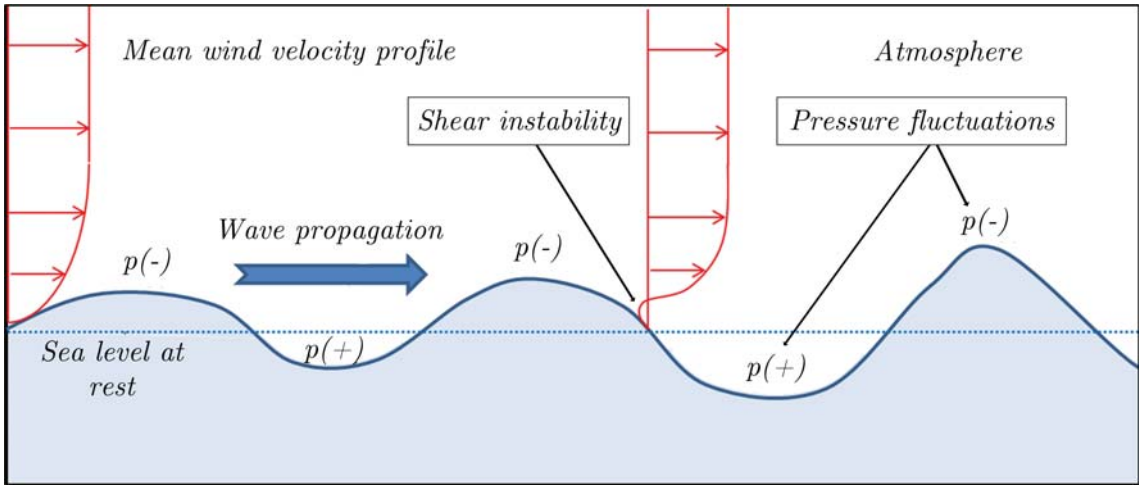

Figure 2.3: The Miles-Phillips wave formation mechanism adapted from Yang (2013).

Linear wave theory describes an ocean wave as a simple harmonic sine wave with parameters shown in Table 2.2. Figure 2.4 provides a graphical display of these parameters. The various parameters used to fully describe the physics of a wave, according to linear wave theory, are now presented.

Table 2.2: Parameters of a simple harmonic sine wave.

Parameter	Symbol	Description	Unit
Wave height	H	The vertical distance between a crest and preceding trough	m
Wave amplitude	a	The vertical distance between the SWL and a crest or trough $\left(\frac{H}{2}\right)$	m
Wavelength	λ	The horizontal distance between two successive crests or troughs	m
Wave period	T	Time it takes for a full wavelength to pass a reference point	s
Water depth	h	Vertical distance from the ocean floor to the SWL	m
Wave number	k	Describes the spatial frequency of a wave	m^{-1}
Angular frequency	ω	Describes the angular displacement rate	Rad/s

Celerity

Waves propagate in a certain direction as a result of particles transferring energy to one another. The speed at which an individual wave propagates is defined as the wave celerity. The celerity, also known as phase velocity, is defined by CEM (2006):

$$c = \frac{\lambda}{T} = \frac{gT}{2\pi} \tanh\left(\frac{2\pi h}{\lambda}\right) \tag{2.1}$$

Group velocity

Waves generally travel in groups which are made up of a collection of sinusoids with varying periods. The rate at which wave energy propagates through space and time depends on this concept. The propagation velocity of a group of waves is known as the group velocity, C_g, and is defined by CEM (2006):

$$C_g = \frac{1}{2}\left[1 + \frac{\frac{4\pi h}{\lambda}}{\sinh\left(\frac{4\pi h}{\lambda}\right)}\right] c \tag{2.2}$$

Wave number

As explained in Table 2.2, the wave number describes the spatial frequency of a wave and is defined by CEM (2006):

$$k = \frac{2\pi}{\lambda} \tag{2.3}$$

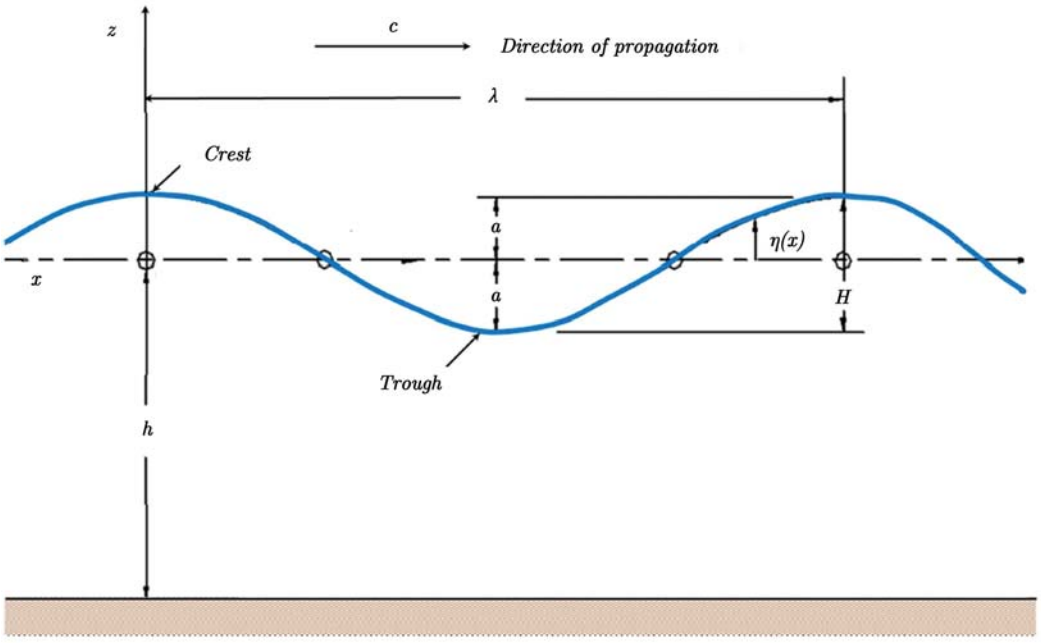

Figure 2.4: Wave parameters adapted from CEM (2006).

Particle velocity

The horizontal u and vertical w components of the individual fluid particles velocity are derived using the surface elevation equation in conjunction with the velocity potential equation. The horizontal and vertical velocity components are defined by McCormick (1981):

$$u = \frac{H}{2}\frac{gk}{\omega}\frac{\cosh\left[k(h+z)\right]}{\cosh(kh)}\cos(kx-\omega t) \tag{2.4}$$

$$w = \frac{H}{2}\frac{gk}{\omega}\frac{\sinh\left[k(h+z)\right]}{\cosh(kh)}\sin(kx-\omega t) \tag{2.5}$$

Surface elevation

Surface elevation describes the movement of the surface of the ocean as a wave propagates past a certain point. The elevation of the surface is defined relative to the still water level (SWL) and is a function of time and horizontal x. Airy (1845) defines the equation governing surface elevation for a linear sinusoidal wave as:

$$\eta(x,t) = \frac{H}{2}\cos\left(\frac{2\pi x}{\lambda} - \frac{2\pi t}{T}\right) = \frac{H}{2}\cos(kx-wt) \tag{2.6}$$

Specific energy

The total energy present in a propagating linear wave is the sum of its kinetic and potential energy. The kinetic energy includes the water particle velocity and potential energy includes the elevation of the wave above and below the SWL. The kinetic and potential energy is integrated over the depth of the fluid layer and averaged over the wave phase. Equation for kinetic energy per unit surface area:

$$E_k = \int_x^{x+\lambda}\int_{-h}^{\eta}\partial z\partial x\frac{1}{2}\rho_w(u^2+w^2) = \frac{1}{16}\rho_w g H^2 \tag{2.7}$$

The potential energy for the wave is derived by subtracting the potential energy available without the wave present, from the potential energy available with the wave present. Equation for potential energy per unit surface area:

$$\begin{aligned} E_p = \int_x^{x+\lambda}\left[\int_{-h}^{\eta}\rho_w g z\partial z - \int_{-h}^{0}\rho_w g z\partial z\right]\partial x = \\ \int_x^{x+\lambda}\left[\frac{1}{2}\rho_w g(\eta^2-h^2) + \frac{1}{2}\rho_w g h^2\right]\partial x = \frac{1}{16}\rho_w g H^2 \end{aligned} \tag{2.8}$$

Where η is surface elevation. The equation for total energy per unit surface area is therefore:

$$E = E_k + E_p = \frac{\rho_w g H^2}{8} \tag{2.9}$$

The derivation of equation 2.9 from first principles can be found in Joubert (2008).

Wave power

In order to derive the total available wave power, the total area of available wave energy must be defined. A_{ocean} is defined as the distance which the wave travels after time T, C_gT, multiplied by the crest width b. See Equation 2.10.

$$E = (E_k + E_p)A_{ocean} = \frac{\rho_w g H^2}{8}(C_gT)b \tag{2.10}$$

Thus, the total incident wave power for a linear wave per unit crest width is given by:

$$P_w = \frac{\frac{\rho_w g H^2}{8}(C_gT)}{T} = \frac{\rho_w g H^2}{8}C_g = \frac{\rho_w g H^2}{8}\frac{1}{2}\left[1 + \frac{\frac{4\pi h}{\lambda}}{\sinh\left(\frac{4\pi h}{\lambda}\right)}\right]\frac{gT}{2\pi}\tanh\left(\frac{2\pi h}{\lambda}\right) \tag{2.11}$$

Equation 2.11 shows that wave power is dependent on wave height, period, length and water depth.

Linear wave theory is considered to be an accurate representation for regular water waves for this project. It also allows for certain simplifications to be made which results in a less complex and more robust model.

2.2.3 Wave particle dynamics

Waves and the particle dynamics associated with waves change as the waves propagate from deep water to shallow water. The fact that the wave particles behave differently as the water depth changes requires a method of classifying waves by water depth. Waves are classified into the three different depth classes as shown in Table 2.3.

Table 2.3: Wave types classified by water depth.

Wave type	Criteria
Shallow water waves	$h < \frac{\lambda}{20}$
Intermediate depth waves	$\frac{\lambda}{2} > h > \frac{\lambda}{20}$
Deep water waves	$h > \frac{\lambda}{2}$

Figure 2.5 shows how the particles behave differently with a change in water depth. This is a very important factor for a WEC located on the sea floor. Figure 2.5 indicates that in deep water the water particles lose their kinetic energy at a depth of $\frac{\lambda}{2}$. Whereas for shallow water waves the horizontal velocity of water particles become increasingly dominant as water depth decreases. The particle dynamics of

a wave and how these dynamics change with a change in depth determines the type of WEC that is appropriate for different locations in the ocean. Various types of WECs and their respective principles of operation are presented in Section 2.3.

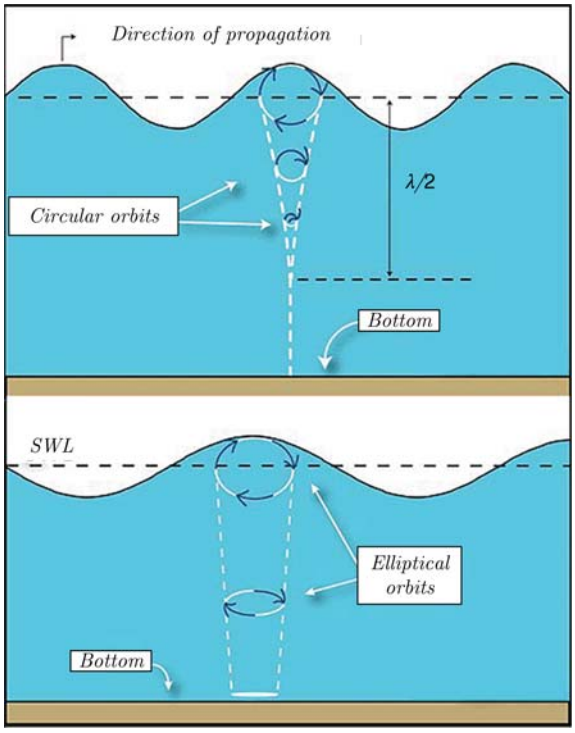

Figure 2.5: Wave particle dynamics. Top: Deep water. Bottom: Shallow Water, adapted from Zevenbergen, Lagasse and Edge (2004).

2.3 Types of WECs

Wave energy converters date back as far as the late 18th century. Modern research into harnessing the power of the waves was driven by the emerging oil crisis in the late 1970s. As mentioned previously, the SWEC was developed at Stellenbosch University during this time, however research and development was halted after the stabilisation of the oil price in the late 1980's.

Research and development of renewable energies and the pressure to find alternate energy sources has once again increase due to the following factors (Joubert, 2008):

- Predicted global climate change.
- Exponential increase in human population.
- Exhaustion of fossil fuels.
- Increase in global electricity demand.

An investigation on other types of WECs was carried out in order to fully understand how wave energy is presently extracted and converted.

2.3.1 Classification of WECs

WECs are classified by two major characteristics, their deployment location and the way that they interact with the waves (their size and orientation during operation).

There are six different deployment locations by which WECs are categorised (see Figure 2.6):

1. Shore-based
2. Near-shore and bottom-standing
3. Floating; near-shore or offshore
4. Bottom-standing or submerged on mid-depth water
5. Submerged not far from water surface
6. Hybrid; units of types 2-5 combined with an energy storage (such as a pressure tank or water reservoir) and conversion machinery on land

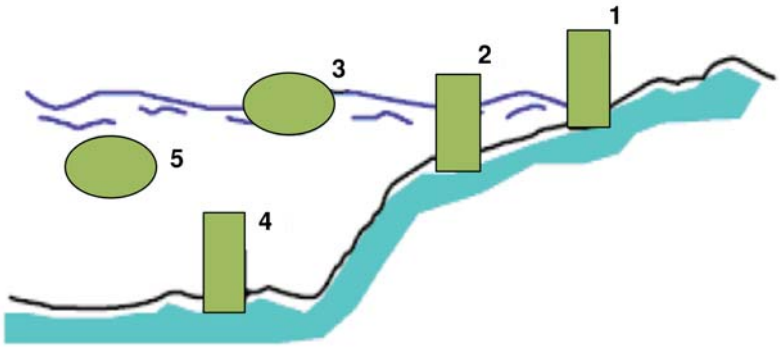

Figure 2.6: Classification by deployment location adapted from Falnes (2005).

When classifying WECs in terms of their size and orientation there are three main types (Drew et al., 2009):

- Attenuator:

  Attenuators are positioned parallel to the propagation direction of the waves. These devices 'ride' the waves, this means that they only harness the kinetic energy which is present on the surface of the ocean waves.

- Point absorber:

  Point absorbers possess small dimensions relative to the oncoming wavelength. They can be submerged below the ocean surface and rely on pressure differential or they can float at the surface of the ocean and rely on the heave up and down. The fact that these devices are so small means that wave direction is not very important and they can generate electricity from a range of varying input directions.

- Terminator

Terminator devices are orientated perpendicular to the wave propagation direction and physically intercept the oncoming waves.

These definitions are also presented in Cruz (2008). WECs can also be characterised by their mode of operation. The different modes of operation are now presented along with a WEC which uses each respective mode.

2.3.2 Submerged pressure differential

When a wave passes overhead the crest of the wave causes an increase in water depth with respect to the ocean floor. When the trough passes overhead it results in a decrease in water depth. This oscillating water depth results in an oscillating pressure differential. Point absorbers use this principle to generate electricity from wave energy. The Archimedes Wave Swing is an example of such a device and can be seen in Figure 2.7.

Figure 2.7: A submerged pressure differential WEC, the Archimedes Wave Swing (Drew et al., 2009).

The Archimedes Wave Swing comprises of two main parts, a cylinder filled with air which is fixed to the seabed and a moveable upper cylinder also filled with air. When the crest of a wave moves overhead the air inside the Wave Swing system is compressed and the moveable cylinder moves downwards. When the trough of a wave moves overhead the air inside the Wave Swing system is decompressed and the moveable cylinder moves upwards. The continuous oscillatory movement of the upper cylinder is used to drive a linear synchronous generator. The Archimedes Wave Swing would generally be deployed in position 4 in Figure 2.6.

An advantage of the Archimedes Wave Swing is that since it is fully submerged, it is not exposed to dangerous slamming forces present at the surface of the ocean. Another advantage is that the device is out of sight, therefore reducing the visual

impact (Drew et al., 2009). A disadvantage of such a device is the maintenance. Maintaining a device beneath the ocean surface could prove to be hazardous and costly. The Power Bouy is another type of point absorber similar to the Archimedes Wave Swing. Both of these designs have reached conversion efficiencies of between 30% and 35% in optimal wave conditions (Sea Grant, 2004).

2.3.3 Oscillating wave surge converter

Oscillating wave surge converters (OWSCs) use the velocity of wave particles to generate electricity. These devices are set up in the terminator position and would generally be found in deployment location 2 in Figure 2.6. Figure 2.8 shows an artist's rendition of an oscillating wave surge converter.

The oscillating wave surge converter is made up of a buoyant hinged deflector attached to the sea floor. As the waves propagate past the deflector the horizontal velocity of the wave particles impart a portion of their energy onto the deflector. This causes the deflector to rock back and forth which pumps high pressure water through a Pelton turbine onshore.

A unique feature of the OWSC is that the buoyancy of the 'buoyancy hinge' is variable, this means that the device can be 'tuned' to operate in the most efficient mode. A disadvantage of this is that the anchoring system has to be designed to withstand the most extreme buoyancy forces even if the device never operates at high buoyancy levels (Whittaker & Folley, 2011). Oscillating surge converters have achieved overall conversion efficiencies of 30% up to 60% (Folley, Whittaker & Osterried, 2004).

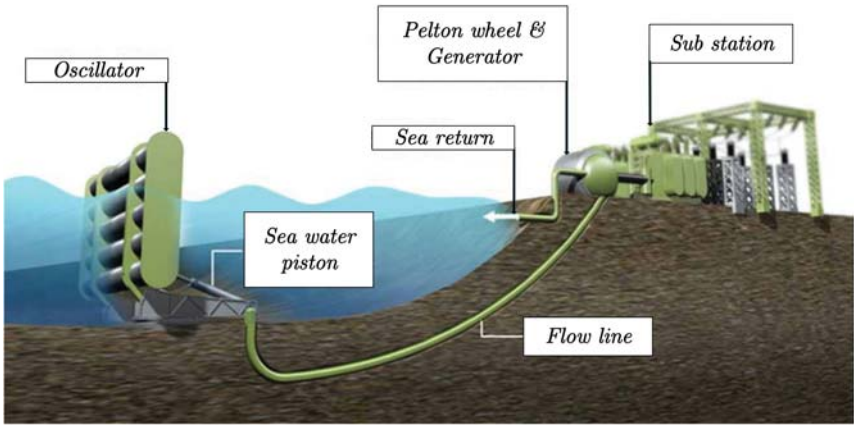

Figure 2.8: An oscillating wave surge converter adapted from Drew *et al.* (2009).

2.3.4 Oscillating water column

An OWC consists of a chamber with an opening facing the oncoming waves which lies below the waterline. OWCs are generally found on the shore in deployment

location 1 or 2 from Figure 2.6. These devices harness the kinetic energy from the moving wave particles. As a wave approaches the OWC's opening, water is forced into the OWC. The OWC's air chamber increases in pressure which forces air out through a turbine into the atmosphere. As the wave draws back the pressure inside the chamber decreases again, and air is drawn back into the air chamber. The problem of bi-directional flow is solved by using a Wells turbine which rotates in the same direction irrespective of the flow direction. An example of a shoreline mounted OWC is the Wavegen Land Installed Marine Power Energy Transmitter (LIMPET) seen in Figure 2.9.

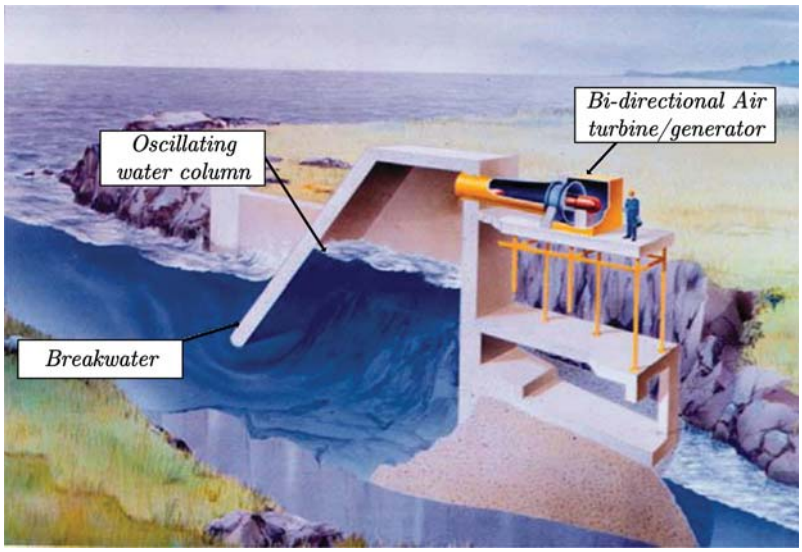

Figure 2.9: The LIMPET OWC adapted from Rodrigues (2006).

OWCs have been implemented as attenuators as well as terminators, as in the case of the LIMPET. It has been suggested that the major advantages of such a device is its robustness and simplicity (Drew et al., 2009). OWC devices such as the LIMPET have obtained overall conversion efficiencies of between 34% (Heath, 2012) and 60% (Whittaker et al., 2004).

2.3.5 Over-topping WEC

Over-topping devices float in the sea and capture water propelled by oncoming waves into a reservoir. The reservoir is located above sea level which means the water possesses potential energy. After the water is captured in the reservoir it is released back into the sea through a turbine, converting the potential energy into kinetic energy. Commonly known as the Wave Dragon, this system was invented by Friis-Madsen (2005).

The Wave Dragon is a floating, slack-moored energy converter of the terminator type. It can be deployed in a single unit or in arrays of Wave Dragon units in groups giving it the ability of being scalable. A group of such devices results in a power plant with a capacity comparable to traditional fossil based power plants(Rodrigues, 2006).

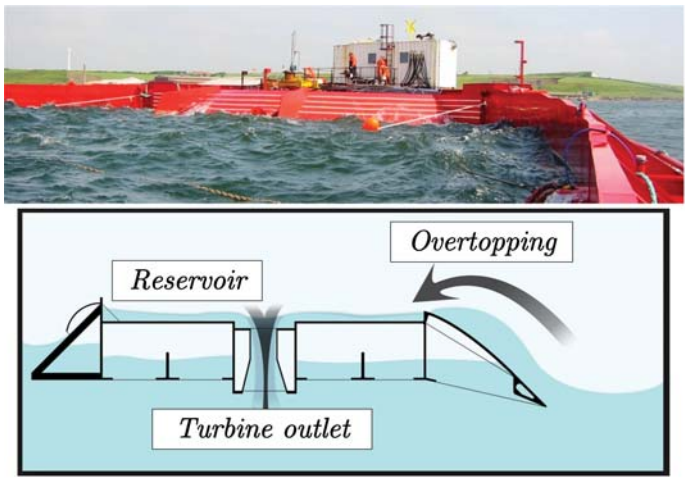

Figure 2.10: Top: Photo of the Wave Dragon. Bottom: Schematic of Wave Dragon. Adapted from Friis-Madsen (2005).

According to Figure 2.6 the Wave Dragon would be deployed in location 3 and acts as a point absorber. Figure 2.10 shows a schematic and a photo of the device. The advantages of such a device are that it is extremely easy to up-scale and due to its small size the maintenance and even major repair works can be carried out at sea. Tedd (2007) carried out an investigation on the conversion efficiency of the device. The results showed a conversion efficiency of 18%.

2.3.6 Pelamis

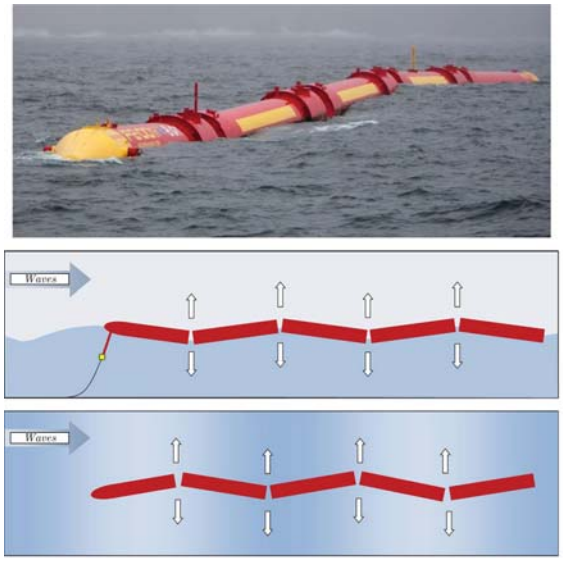

Figure 2.11: Top: Photo of the Pelamis. Bottom: Movement of Pelamis (Pelamis Wave Power Ltd, 1998).

This device gets its name from the Latin word for 'sea snake' as the motion of the device mimics the motion of the reptile. The Pelamis is a floating device made up

of multiple tubular sections connected by hinges. These tubes 'ride' the waves as they propagate past. This riding motion forces the tubes to move relative to each other. The relative motion is transferred to hydraulic pistons which drive a digitally controlled hydraulic power conversion system. Figure 2.11 shows a photo and an illustration of the movement of the device.

The Pelamis is deployed in position 3 in Figure 2.6 and operates as an attenuator. One of the main advantages of the Pelamis is that it is designed to stay out at sea throughout the year (Pelamis Wave Power Ltd, 1998). Therefore the device must be extremely robust. The robustness of the design allows for longer periods of generating electricity and cheaper maintenance costs. One of the disadvantages of the device is that it is very visible and can be visually displeasing. The device could also potentially be a threat to navigation as ships could collide with it. Conversion efficiencies up to 70% have been achieved with this device (Yemm, Pizer, Retzler & Henderson, 2011).

2.3.7 Submerged SWEC

The submerged SWEC will be deployed in location 4 in Figure 2.6. The SWEC was long thought to be a point absorber, only using the pressure differential caused from the wave passing overhead to drive the generator. Fairhurst (2013) tested a scale model of a single SWEC chamber in various orientations. The test results showed that the chamber captures far more energy with the opening facing the oncoming wave compared to facing away. This suggests that the SWEC chambers don't only capture energy due to the pressure differential of the wave passing overhead, but also due to the motion of the incoming wave. As shown in Section 2.2, wave particles have vertical as well as horizontal velocity. The velocity of the wave particles along with the pressure differential forces the water in and out of the chambers. The SWEC is classified as an attenuator.

Main advantages of the submerged SWEC:

- Hidden from view.
- Based on the concept of an OWC but does not require a bi-directional turbine due to the air flow being rectified.
- Fully submerged and therefore isn't exposed to dangerous slamming forces present at the surface of the ocean.
- Could provide structure for reef to grow in an area which would otherwise be barren.
- Can be used as a break water as well as a WEC.

Main disadvantages of the SWEC:

- Maintenance and repair work on a submerged structure like the SWEC would be hazardous, costly and time consuming.
- Grid connection could prove difficult as the device is submerged and offshore.

- Relatively low energy conversion efficiency.

2.4 Simulation methods for OWC's hydrodynamics and thermodynamics

This section introduces some of the theory required to develop a verified simulation model for a submerged OWC. Literature relevant to modelling the hydrodynamics of the SWEC is presented first, followed by literature relevant to the airflow system and thermodynamics. The section is concluded with an investigation into the experimental set-up which was used by Fairhurst (2013).

2.4.1 Hydrodynamics

The hydrodynamics of the submerged SWEC chamber refers to the interaction of the water particles with the chamber. The hydrodynamics are extremely important and need to be modelled accurately as it determines the movement of the free water surface of the OWC. The movement of the free water surface inside the chamber serves as the input to the airflow system. There have been many attempts to accurately model the hydrodynamics of OWC systems, some are presented here.

Evans (1976) carried out one of the earliest investigations on oscillating bodies used as wave energy converting devices. The study presents a simple linearised, lumped-body mechanical model which uses linear wave theory to set up expressions for optimum body motions, and power capture by an oscillating body. Various shapes and forms of oscillating bodies were investigated. The study showed that the maximum amount of power which can be absorbed by three-dimensional bodies, having a vertical axis of symmetry, is equal to $\left(\frac{\lambda}{2\pi}\right)$ times the power per unit crest length. One of the limiting factors of the presented model is that the air inside the chamber is assumed to be an incompressible adiabatic fluid.

McCormick (1981) introduces OWCs as cavity resonators and explains how they can be used to generate electricity by absorbing power from ocean water waves. He then goes on to present a model for the cavity resonators based on the same rigid-body theory as Evans (1976) and suggests that the internal surface of the OWC must be excited at its resonant frequency in order to produce maximum power. This theory models the free surface as a piston and incorporates the added mass and damping of the system in a similar way to Evans (1976).

Szumko (1982) carried out a study which examines certain aspects of the OWC modelling with particular focus on the compressibility of the air inside the chamber and the behaviour of the system at off-resonant frequencies. Similar to Evans (1976), the study was also based on linear wave theory and a lumped-body mechanical model. A previous study carried out by Revill (1978) showed that the device could be modelled by a spring, an added mass and two dash-pots rigidly connected to a fixed point and the added mass.

The one dash-pot represents the added damping and the other represents the power take-off in the system. This model was used as a basis and was modified by Szumko (1982) to allow for air-column compressibility. A spring was inserted between the added mass and the dash-pot simulating the power take-off. The mechanical model can be seen in Figure 2.12. One of the more prominent discoveries of this study was that the efficiency of the OWC was practically unaffected by compression when at resonance. It was found that at frequencies below resonance, the efficiency drops and at frequencies above resonance the efficiency and optimum damping increase at a remarkable rate (Szumko, 1982).

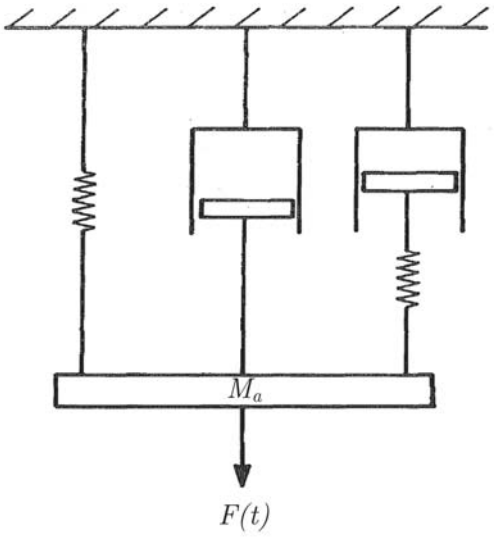

Figure 2.12: Forces acting on added mass M_a for mechanical model of "spring-dash-pot" system adapted from Szumko (1982).

Evans (1982) carried out a study focused on the efficiency absorption of a system of uniform oscillatory surface pressure distributions. The theory presented by Evans (1982) assumes the internal volume of the OWC to be small enough to allow the air to be modelled as a solid, incompressible fluid. The common practice of using an orifice plate to model the PTO device as well as a method of determining the volumetric flow rate in the OWC is also introduced.

Most of the previously mentioned studies have been developed using potential theory, based on a radiation and diffraction approach. Gervelas, Trarieux and Patel (2011) take on a different approach using well documented work carried out on trapped air cavities for marine vehicles to model an OWC in irregular waves. Gervelas *et al.* (2011) modelled a similar system compared to the SWEC system and is used as a reference in this thesis. A time-domain model for an OWC which describes the coupling between the hydrodynamic and the thermodynamic forces for an OWC is produced. The model predicts the water elevation and pressure variation inside the chamber for regular and irregular input waves. The described system is shown in Figure 2.13.

The model developed by Gervelas *et al.* (2011), like most of the studies mentioned, uses linear wave theory to represent the input waves. The model also effectively

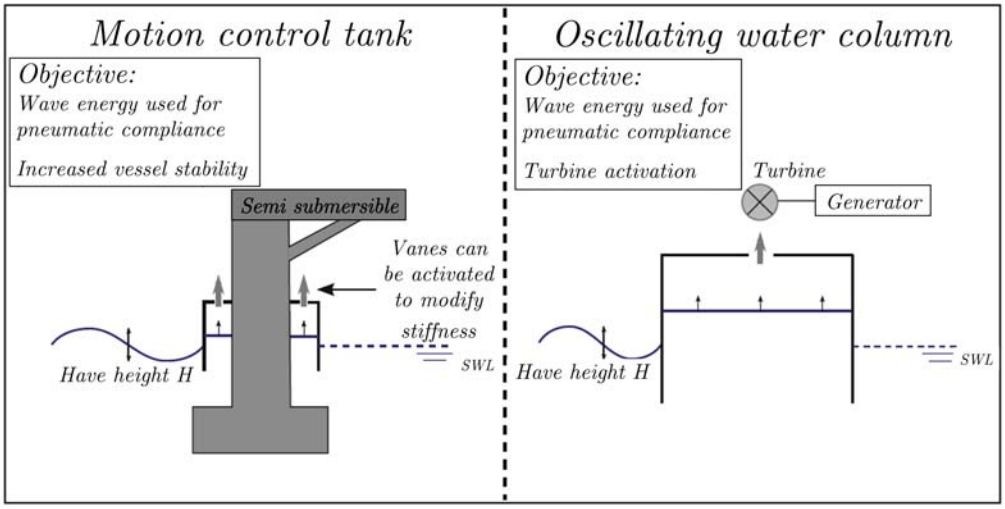

Figure 2.13: Motion control tank analogy for OWC WEC adapted from Gervelas *et al.* (2011).

incorporates the added mass phenomenon as a damping force on the system. It has proven difficult to fully define the added mass for the SWEC system in past studies, thus the concept of added mass was researched in depth.

Brennen (1982: 2) carried out an in-depth investigation on the added mass phenomenon and states that the simplest way of describing added mass is that it "determines the necessary work done to change the kinetic energy associated with the motion of the fluid". Brennen (1982) goes on to describe that any motion of a fluid that occurs due to a body moving through it requires a certain amount of non-zero kinetic energy to move. If the velocity, U, of a body through a liquid is constant, the kinetic energy, E_k, required to move the fluid will also stay constant. Also, it is clear that E_k will be proportional to U^2. One can then assume that if U is altered, the velocity, u_i at each point in the fluid relative to the body varies in direction proportional to U. This allows E_k to be expressed as

$$E_k = \rho \frac{I}{2} U^2 \text{ where } I = \int_V \frac{u_i}{U} \frac{u_i}{U} \partial V \tag{2.12}$$

Where V is the volume of the fluid which is in motion. I tends to be a simple invariant number when dealing with fluid flow solutions such as potential flow and low Reynolds number Stokes flow. However this does not hold true for more complex flows which involve vortex shedding and intermediate Reynolds numbers (Brennen, 1982). If the body in motion starts to accelerate or decelerate, clearly the kinetic energy in the fluid will also change. If the body accelerates, the kinetic energy in the fluid will in all probability also increase. This energy must be supplied from somewhere, and therefore additional work must be done on the fluid by the body. The rate of additional work required is simply the rate at which the kinetic energy of the fluid changes with respect to time, $\frac{\partial E_k}{\partial t}$.

The body in motion experiences this extra work as a drag force,$-F_d$, such that

the rate of additional work done is equal to $-F_d U$. If the pattern of flow remains constant and therefore I is constant, it follows that the 'added drag' force is simply,

$$F_d = -\frac{1}{U}\frac{\partial E_k}{\partial t} = \rho I \frac{\partial U}{\partial t} \tag{2.13}$$

Brennen (1982) goes on to show that this force has the same sign and form required to accelerate the mass, m , of the body itself namely $m\frac{\partial U}{\partial t}$. It has become common practice to visualise ρI as an added mass M_a. Brennen (1982: 3) concludes this introduction to added mass by stating that "of course, there is no such identifiable fluid mass, rather all the fluid is accelerating to some degree such that the total kinetic energy of the fluid is increasing".

The added mass specifically associated with the SWEC is explained in greater detail in Chapter 4. Accurate modelling of the hydrodynamics of the system is crucial as it provides an accurate input for the system's airflow model. This input describes the movement of the chamber's internal free surface.

2.4.2 Thermodynamics

This section presents the various studies which were investigated in order to model the SWEC's airflow system which is governed by various thermodynamic relationships.

Kim and Koo (2011) developed and applied a boundary element method to various land-based OWCs taking air compressibility into account. The non-linear internal free-surface was modelled to take into account both the viscous effect of the water column as well as the effect which the time varying pressure distribution has on the pneumatics. The energy loss due to the fluids viscosity was accounted for by imposing an artificial damping upon the free surface. The air-continuity equation was used to solve the interaction of the water columns movement and the compressed air caused by the change in volume.

The study found that the motion of the internal free surface differed quite a lot when taking into consideration the compressibility of air compared to neglecting compressibility. Thus without proper pneumatic modelling the efficiency of the device cannot be accurately predicted. Kim and Koo (2011) state that the pressure inside the chamber, $p_c(t)$, can be modelled as linearly proportional to the velocity of the air flowing inside the OWC, see Equation 2.14.

$$p_c(t) = BU_d(t) \tag{2.14}$$

Where B is the damping coefficient and $U_d(t)$ is the airflow velocity inside the outlet duct, assuming the air is incompressible. This assumption is only valid for relatively small volumes. For very large volumes the air takes on a spring-like behaviour. The continuity equation is then used to relate the volume change inside the chamber to

the air velocity. This allows for the air pressure to be written in terms of volumetric flow rate inside the chamber, see Equation 2.15.

$$p_c(t) = \frac{B\Delta V}{A_d \Delta t} \tag{2.15}$$

Sarmento and Falcao (1985) describe the springlike effects which occur due to the compressibility of the air in the OWC in the case of a very large air volume. The springlike effects are not considered in the study carried out by Kim and Koo (2011).

Ackerman (2009) presented a study which attempted to model the SWEC in order to design an appropriate turbine for the device. The airflow system was modelled by solving the continuity equation (Equation 2.16), the momentum equation (Equation 2.17) and the energy equation (Equation 2.18).

$$\frac{\partial}{\partial t}\left(\int_V \rho_a dV\right) + \int_A \rho_a U dA = 0 \tag{2.16}$$

$$\Sigma F = \frac{\partial}{\partial t}\left(\int_V U\rho_a dV\right) + \int_A U\rho_a U dA \tag{2.17}$$

$$\begin{aligned}\frac{\partial Q}{\partial t} - \frac{\partial W}{\partial t} = \frac{\partial}{\partial t}\left[\int_V \left(\frac{U^2}{2} + gz + e_{si}\right)\rho_a dV\right] + \\ \int_A \left(\frac{p}{\rho_a} + \frac{U^2}{2} + gz + e_{si}\right)\rho_a U dA\end{aligned} \tag{2.18}$$

The system is assumed to be isothermal (the temperature of the system stays constant) and adiabatic (there is no transfer of matter or heat to the systems surroundings). Equation 2.19 is an adaptation of a relationship that defines pressure and flow in an adiabatic system. It is used to show that the temperature change in the system is negligible. The pipe flow equation for flow through ducts is derived from the energy equation (Equation 2.20) and the ideal gas law (Equation 2.21) is assumed sufficient to model the pressure in the system.

$$\frac{\tau_1}{\tau_2} = \left(\frac{p_1}{p_2}\right)^{\frac{\gamma-1}{\gamma}} \tag{2.19}$$

$$p_1 + \frac{\rho_1 U_1^2}{2} + z_1 = p_o + \frac{\rho_o U_o^2}{2} + z_o + \rho_o g \Sigma h_L \tag{2.20}$$

$$p_1 V_1 = m_1 R \tau_1 \tag{2.21}$$

The losses in the system are taken into account by using the pipe flow equation along with the coefficients which describe the damping of the various pipe charac-

teristics such as bends, expansions and contraction to name a few. Ackerman (2009) concludes the airflow modelling by defining the model to be accurate up to 3 m wave height and the inaccuracies could be a result of inaccurate added mass assumptions and Froude scaling.

Holtz (2007) carried out a study which developed a simplified model of an air-spring with auxiliary chamber attached. In addition to the development of the simulation model, experimental tests were carried out in order to validate the simulation model. The significance of this study is that the air spring model relates well to the airflow system of the submerged SWEC with an attached auxiliary volume. The airflow model developed by Holtz (2007) describes the system shown in Figure 2.14. This schematic shows the similarities between the air-spring system and the submerged SWEC system where the mass load represents the OWC's inner surface level and the input to the thermodynamic system.

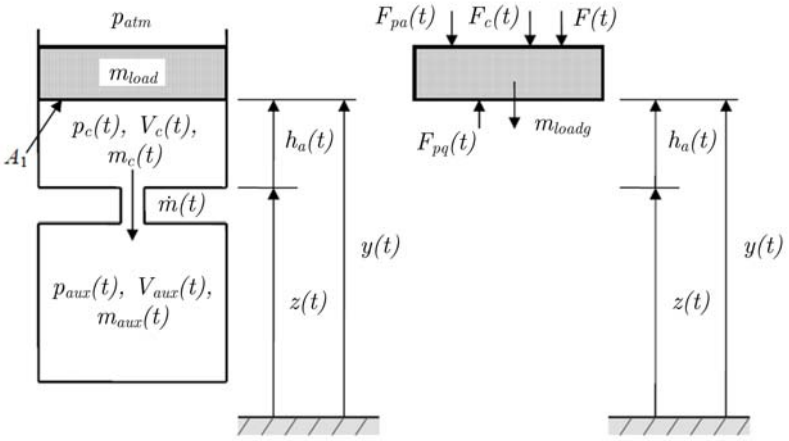

Figure 2.14: Schematic of model developed by Holtz (2007).

Holtz (2007) defines the mass flow rate through the capillary by using the expression for head loss in a pipe seen in Equation 2.22. The air flow for the submerged SWEC is also assumed to be turbulent due to the average Reynolds number being in the transient region combined with oscillatory nature of the system. The head loss equation is used to set up an expression describing the total head loss in the system (Equation 2.23). K_x is included as an undetermined loss coefficient. An expression for the mass flow rate, seen in Equation 2.24, is derived using the head loss expression in combination with the energy equation for pipe flow.

$$h_l(t) = K\frac{\dot{V}(t)^2}{2g} \tag{2.22}$$

$$h_l(t) = K_f\frac{\dot{V}(t)^2}{2g} + K_c\frac{\dot{V}(t)^2}{2g} + K_e\frac{\dot{V}(t)^2}{2g} + K_x\frac{\dot{V}(t)^2}{2g} \tag{2.23}$$

$$\dot{m}(t) = A_d \sqrt{\frac{2\rho_{avg}(t) \mid \Delta p(t) \mid}{(K_f + K_c + K_e + K_x)}} sign\left[p_c(t) - p_{aux}(t)\right] \tag{2.24}$$

where,

$$\rho_{avg}(t) = \frac{p_c + p_{aux}}{R\left(\tau_c + \tau_{aux}\right)} \tag{2.25}$$

The two models derived for this thesis were produced by combing certain aspects of the previously mentioned studies whilst making various adaptations and adjustments in order to fit the Surface and Submerged SWEC systems.

2.4.3 Existing experimental set-up

Fairhurst (2013) experimentally tested a scale model of the submerged SWEC device in various wave conditions and orientations. The aim of the study was to determine the conversion efficiency of the design.

The experimental results provided insight on the optimal orientation for power conversion but did not produce accurate results with regard to the magnitude of the wave energy converted. The magnitude of the energy converted, and therefore the efficiency of the device was restricted due to the auxiliary volume being too small. See Figure A.1 in Appendix A for the existing experimental set-up.

Chapter 3 explains how the auxiliary volume used for this study was sized and sheds light on why the smaller auxiliary volume used by Fairhurst (2013) produced unreliable results. The ability of water to flow into and out of the SWEC chamber is dependent on the compressibility of the air in the system. A small auxiliary volume and therefore small overall system volume leads to the compressibility of the air being very low. An infinitely large auxiliary volume was obviously not an option and so a compromise had to be made. Chapter 3 explains the calculations which sized the auxiliary volume which would ensure that the compressibility of the air was not restricted for this study.

Adaptations to the existing experimental set-up include:

- Increased auxiliary volume.
- Lengthened outlet duct.
- Different pressure transducers used (detailed in Chapter 3).
- Atmospheric temperature measurement added.
- Two additional orifice plates.

Chapter 3 details the experimental set-up and procedures involved in the testing of the SWEC scale model.

Chapter 3

Experimental testing

This chapter outlines the two experimental configurations and their respective experimental procedures. The chapter proceeds to detail the design, construction and adaptation of the scale model tested for this research project. The instruments and apparatus used during the experimental testing as well as their calibration processes are defined and explained in full.

3.1 Experimental set-up and procedures

This section describes the experimental set-up for both the Surface and Submerged SWEC configurations. The experimental procedures and test procedures are also detailed in full.

3.1.1 Surface SWEC configuration

The experimental set-up and test procedure for the Surface SWEC configuration is presented.

Experimental set-up

Figure 3.1 provides a schematic layout of the Surface SWEC experimental set-up and the positioning of the wave probes and differential pressure sensors. See Table 3.1 for a brief description of each instrument and its positioning. The waves produced by the wave paddle are only fully formed at a distance equal to 2 wavelengths away from the paddle. The beach starts 20 m away from the paddle and the input wavelengths range from 3 m to 8 m. A compromise had to be made and the chamber was placed 15 m away from the wave paddle.

The SWEC chamber has a width of 0.48 m while the flume is 1 m wide. It is assumed that the chamber is far enough away from the sides of the flume to ensure that there is a negligible amount of wall interference. The delicate electrical equipment used

was placed outside of the flume on the right hand side in a safe and dry wooden channel. See Figure 3.2 for a photo of the Surface SWEC configuration taken from the side of the wave paddle.

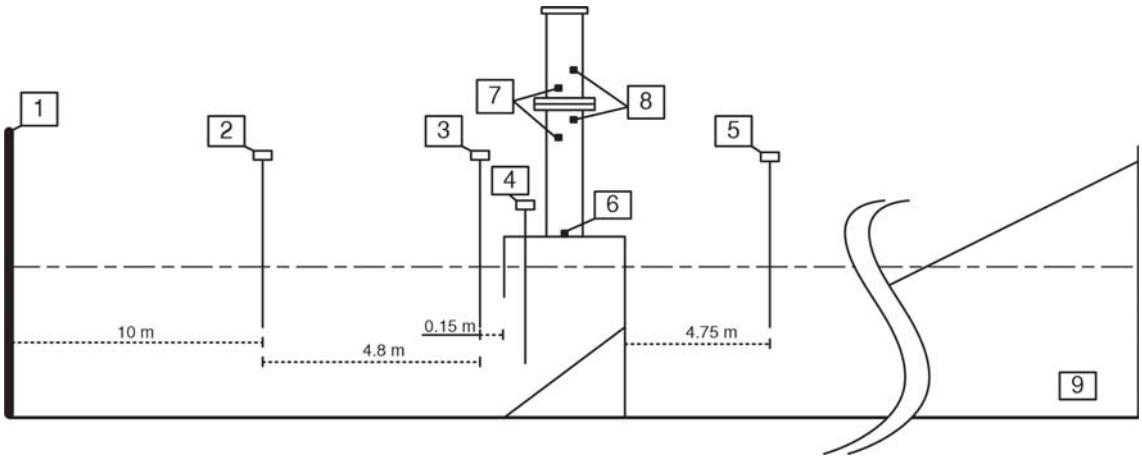

Figure 3.1: Surface SWEC experimental set-up.

Table 3.1: Surface SWEC experimental set-up parameters.

Number	Instrument	Description
1	Wave paddle	Used to create waves in the wave flume.
2	Wave probe 1	Measures surface level before wave is fully formed.
3	Wave probe 2	Measures surface level very close to the chamber.
4	Wave probe 3	Measure surface level inside the chamber.
5	Wave probe 4	Measures the wave once it has passed the chamber.
6	Pressure sensor 1	Measures differential pressure between chamber and atmosphere.
7	Pressure sensor 2	Measures differential pressure over the orifice for positive mass flow.
8	Pressure sensor 3	Measures differential pressure over the orifice for negative mass flow.
9	Beach	Situated at the end of the 30 m flume it allows for the waves to be absorbed and therefore no reflected waves are produced.

Experimental procedures and test procedure

Each day of testing started with taking atmospheric pressure and temperature readings using an extremely accurate barometer (error of less than 0.05%) and thermometer. The wave probes were calibrated and the water level of the wave flume was

checked. See Table 3.2 for the various characteristics which individually describe a test and the ranges of these characteristics which were tested.

Figure 3.2: Left: Photo of Surface SWEC experimental set-up. Right: Photo of Submerged SWEC experimental set-up.

Table 3.2: Surface SWEC tests.

Wave height (m)	Wave period (s)	Orifice hole diameter (m)	Orientation
0.03, 0.06, 0.09	1.5, 1.75, 2, 2.25, 2.5, 2.75, 3, 3.25	0.014, 0.019, 0.027, 0.038, 0.047	0°

Each test ran for 150 seconds. The measurements taken by the 4 wave probes and 3 differential pressure transducers were recorded at a rate of 100 recordings/second.

3.1.2 Submerged SWEC configuration

The experimental set-up and test procedure for the Submerged SWEC configuration is presented.

Experimental set-up

Figure 3.3 provides a schematic layout of the Submerged SWEC configuration in a similar fashion to Figure 3.1. See Table 3.3 for a short description of the elements which differ for this configuration.

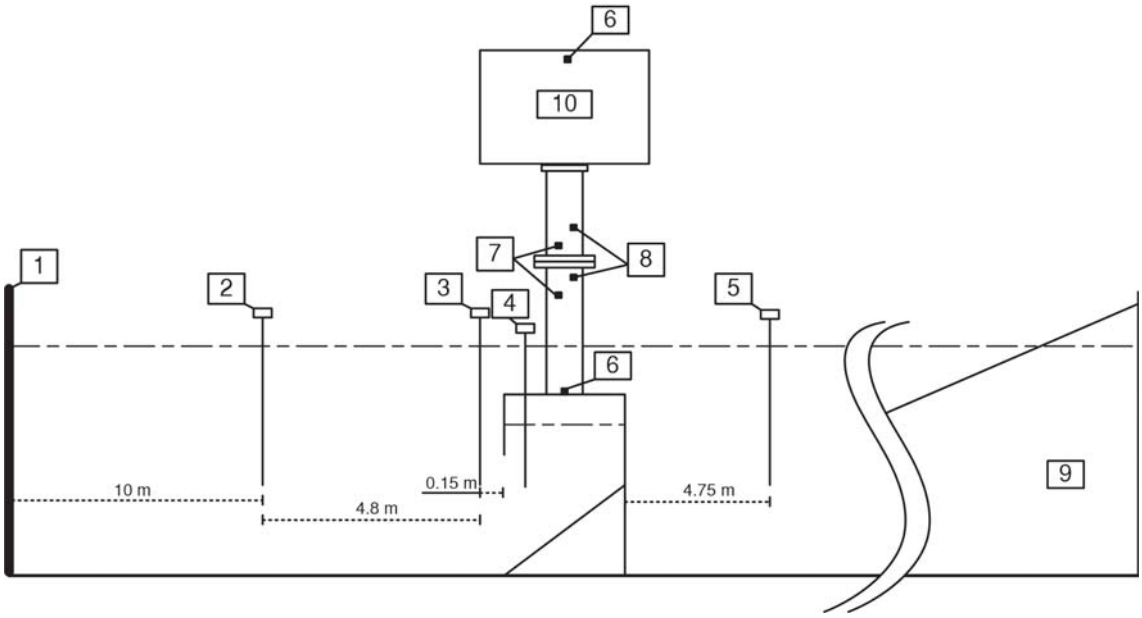

Figure 3.3: Submerged SWEC experimental set-up.

Table 3.3: Varying Submerged SWEC experimental set-up parameters.

Number	Instrument	Description
6	Pressure sensor 1	Measures differential pressure between chamber and auxiliary volume.
10	Auxiliary volume	Allows for the system to be at a higher static pressure than that of the atmosphere

In the Submerged SWEC configuration, the opening of the SWEC chamber lies 0.257 m below the flume's water level. This level was chosen in order to simulate submergence near to the expected submergence of 0.22 m. The static pressure inside the chamber had to be elevated above atmospheric pressure due to the chamber being submerged. This was done by using compressed air and raising the static chamber pressure to 1950 Pa above atmospheric pressure. See Figure 3.2 for a photo of the Submerged SWEC set-up, note that the water level in the flume has not yet been raised in this photo and the chamber top is still above the SWL.

Experimental procedures and test procedure

The daily testing procedures were the same for the Submerged SWEC configuration as for the Surface SWEC except that the system was pressurised and the water level

inside the chamber was lowered before testing. See Table 3.4 for the ranges of these characteristics which were tested for the Submerged SWEC. Each test was run for the same length of time as the Surface SWEC tests and at the same recording rate.

Table 3.4: Submerged SWEC tests.

Wave height (m)	Wave period (s)	Orifice hole diameter (m)	Orientation
0.065, 0.09, 0.11	1.5, 1.75, 2, 2.25, 2.5, 2.75, 3, 3.25	0.014, 0.019, 0.027, 0.038, 0.047	0°, 45°, 90°, 135°, 180°

3.2 Apparatus

This section starts by outlining the design and scaling of the experimental model. It then goes on to detail all the apparatus used during testing including the wave flume, wave sensors, differential pressure transducers, orifice flow meter and data acquisition unit.

3.2.1 Chamber dimensions, design and scaling

The dimensions, design and scaling of the SWEC chamber is discussed in this section.

Chamber dimensions and design

The scale model used in this project was designed and constructed by Fairhurst (2013). Fairhurst (2013) provides a full critique, analysis and drawing pack of the scale model. The model was designed to represent a single SWEC chamber with the ability to convert wave power into pneumatic power in a similar fashion to the SWEC device.

The geometry of an OWC chamber has been proved to affect the power output to a large degree (Dizadji & Sajadian, 2010). This project aims to test the existing SWEC chamber design; therefore a major effort was made to allow the test model to represent the original SWEC chamber. Ackerman (2009) provides the most current dimensions as well as the broader operating conditions of the SWEC, see Figure A.2, Table A.1 and Table A.2 in Appendix A.

Various chamber designs were conceptualised and eventually evaluated with the following aspects serving as the evaluation criteria:

- Representation of the SWEC prototype chamber
- Cost
- Manufacturability

- Sturdiness
- Weight

The various concepts and their respective scoring are available in Fairhurst (2013). The chamber design which scored the best can be seen in Figure 3.4. The chamber along with the orifice flow meter and auxiliary chamber make up the SWEC chamber representative for this project. The key aspects of the chamber design are mentioned below:

- Orthogonal base plate assists with changing the orientation.
- Wave probe positioned inside chamber to record inner chamber surface height.
- 45° Ramp used to reduce turbulence inside chamber and direct the motion of the water particles upwards.
- Chamber sides made out of perspex rendering the inner chamber surface level visible.
- Chamber pressure tapping allows for differential pressure sensor to record chamber pressure.

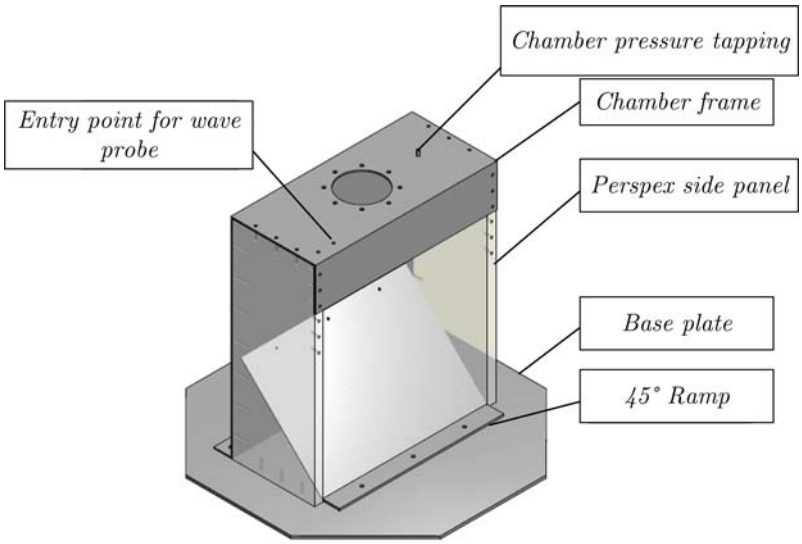

Figure 3.4: Model SWEC chamber adapted from Fairhurst (2013).

Scaling

As previously mentioned Ackerman (2009) provides the most recent chamber dimensions as well as operating conditions. A scaling method was required in order to scale both the chamber dimensions and wave conditions in order to represent the SWEC system most effectively. Froude scaling was used as it is the most common scaling method when working with water waves. This is due to the fact that ocean waves are considered as open channel flow and gravity effects are very influential (Chanson, 1999). Froude scaling was also used in the very first test done on the

SWEC design by Retief *et al.* (1982), thus supporting the choice of scaling. See Equation 3.1 for the dimensionless Froude number which characterises the ratio of internal force to the force of gravity.

$$\text{Froude number} = \frac{U_0}{\sqrt{g_0 l_0}} \tag{3.1}$$

The Froude number is used to define the relationships between the various characteristics seen in Table A.3. A dimension scale, L_r, of 25:1 was chosen for the following reasons:

- The flume has a maximum water level of 0.8 m. This scale gives the model a height of 0.6 m and therefore allows a water depth of 0.6 m to 0.8 m. This corresponds exactly with the 15 m to 20 m depth expected for the prototype chamber.
- The scale gives the model a width of 0.48 mm which allows the model to fit in the flume. The sides of the chamber are far enough away from the walls of the flume so that interference from the walls is assumed to be negligible.
- The scale provides a range of test scenarios which fit the prototype operating scenarios.
- The scaling results in a manageable size model.

See Tables A.3 through to A.5 in Appendix A for a detailed presentation of the scaling. The scaling used for this project resulted in a blockage ratio of 0.48 which was deemed acceptable as a blockage ratio of up to 0.3 is generally accepted to have negligible effects on wave flume waves. It is also assumed that the Submerged SWEC would cause less of a blockage effect compared to a structure which takes up the entire column of water due to it being submerged.

3.2.2 Wave flume

The experimental testing for this project was carried out in the glass wave flume in the Hydraulics Laboratory of the Department of Civil Engineering at Stellenbosch University. The wave flume and the available wave conditions had to be investigated in order to ensure the required wave conditions could be produced. The flume is 1 m wide, 1.2 m deep (maximum still water depth of 0.8 m) and 30 m in length. The end of the flume has a gradual slope which acts as a beach. Dolos and bricks were added to the sloping beach to improve wave absorption at the end of the flume to ensure no waves were reflected back towards the model.

The flume is equipped with a HR Wallingford wavemaker which is driven by an electric rack-and-pinion actuator paddle. Wave absorption enables the wavemaker to absorb waves reflected back towards the paddle. This helps achieve the required

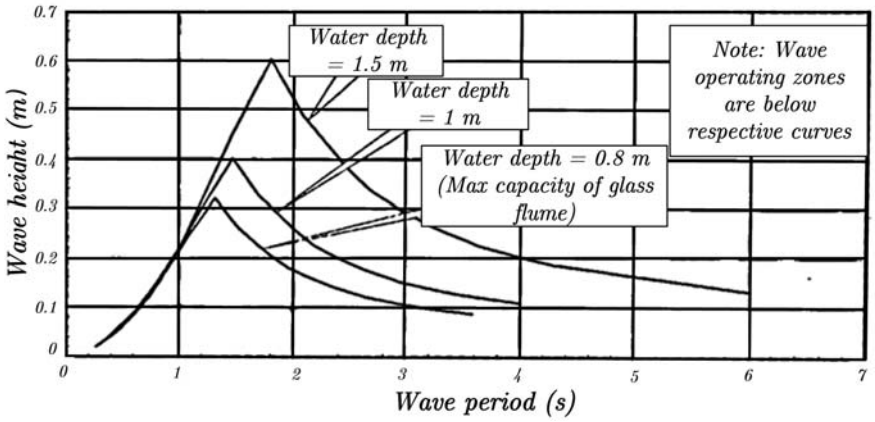

Figure 3.5: Flume operating conditions adapted from HR Wallingford Ltd (2009).

input wave height. Figure 3.5 displays the wave conditions which can be generated in the flume in various circumstances.

3.2.3 Wave probes

The wave probes used for this project allow the measurement of water surface height, $\eta(t)$, at specific locations in the wave flume. The probes were strategically placed in these specific locations for the reasons explained in Section 3.1. The wave probes operate by measuring the current flowing between the two stainless steel legs which are immersed in water. The current is then converted to an output voltage which is directly proportional to immersed depth (HR Wallingford Ltd, 2009), see Figure 3.6 for a photo of a wave probe.

Each wave probe is made up of two parallel stainless steel rods each with a plastic head and foot. The head is fixed to the calibration stem and a mounting block; this allows the calibration stem to be fixed to a vertical surface (HR Wallingford Ltd, 2009). The wave probes have an error tolerance of 2%. Although the probes are extremely sensitive and accurate, their measuring capability can be greatly affected by temperature and water salinity and therefore must be calibrated daily. The wave probes were calibrated daily for this project to ensure accurate readings; the following subsection explains the calibration process.

Calibration

Four wave probes were used during testing. Their positions and purpose is detailed in Section 3.1. Three of the probes were positioned with the rods measuring the surface level of the waves open to the atmosphere. The fourth probe was positioned inside the chamber and measured the inner chamber surface level.

The three outer wave probes were calibrated by moving them 0.02 m above and below the zero-position, the zero-position being the SWL for the next experimental

test. The probe inside the chamber was in a fixed position as the chamber was required to be air tight, this probe was therefore calibrated by changing the water level. For the Surface SWEC configuration, the water level was adjusted by draining or filling the tank. The water level inside the tank was measured using a steel ruler which is fixed to the inside of the tank. Once three known reference points were captured the HR Wallingford calibration software was used to fit a linear calibration curve. The calibration curve relates voltage, $v_o(t)$, to surface height, $\eta(t)$.

Figure 3.6: Left: Wave probe in flume. Right: Stand alone wave probe.

For the Submerged SWEC configuration, the water level was adjusted by pressuring or de-pressurising the system. The water level inside the SWEC chamber was measured using a ruler fixed to the inside of the chamber wall. The calibration was checked by recording the immersion whilst displacing the probes by a known distance. See Figure 3.7 for an example of this calibration check, the probes where moved 0.02 m above and then 0.02 m below the zero height.

Figure 3.7 confirms the probe calibration to be accurate. The variation around the 0.02 m and -0.02 m marks are due to the fact that the water in the flume was not at rest. The overshoot present for Probe 1 at 20 seconds and Probe 3 at 155 seconds is due to the probes being lowered to the corresponding levels at a rapid rate.

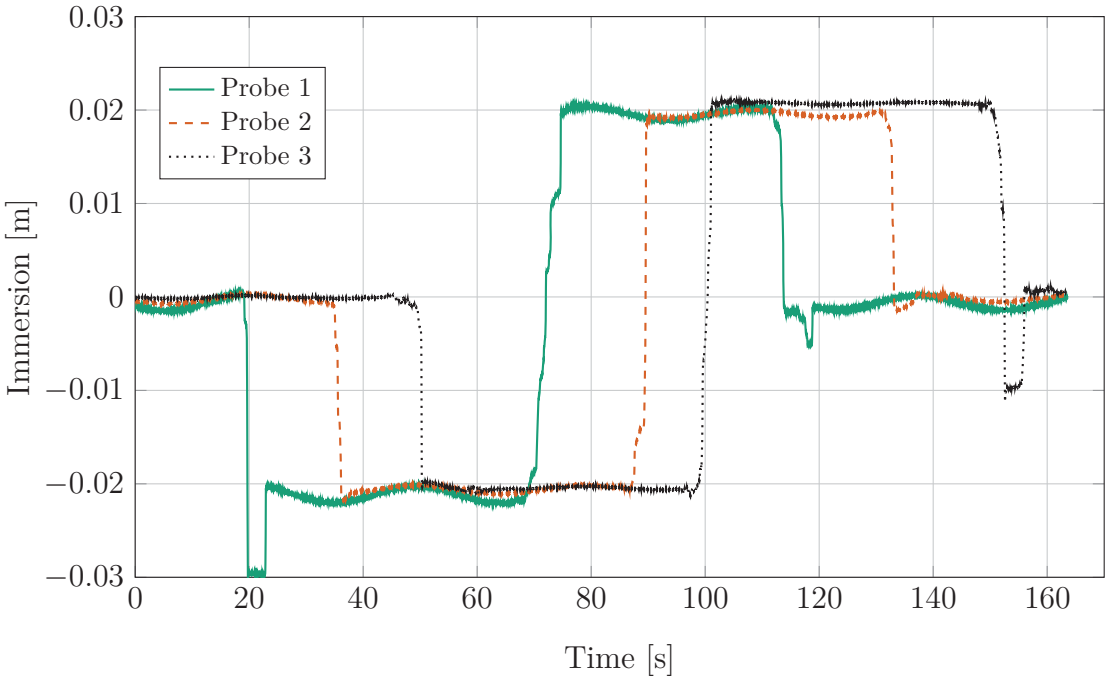

Figure 3.7: Wave probe calibration check.

3.2.4 Pressure transducers

Previous studies carried out on the SWEC device including Fairhurst (2013), Ackerman (2009), Meyer (2012), Kooverji (2011) and Joubert (2013) all used Endress & Hauser (EH) differential pressure transducers. A sensitivity analysis was carried out on the sensors to ensure their accuracy. In fact this analysis showed that the response and settling time of the sensors was indeed too slow. The analysis suggested the specific EH differential pressure transducers in question are only adequate to measure static pressure systems. This resulted in other pressure sensors being required to measure the oscillating pressures present in this study.

Firstly the EH sensors were statically calibrated using an extremely accurate Betz manometer (error of less than 0.05%). They proved to be statically accurate as the on-board visual display matched the Betz manometer readings almost exactly (less than 1% error). Three EH sensors were connected to the same pressure tapping on the SWEC device via a three way connector piece, this was done to check the consistency of the devices. The sensors were tested by inducing an oscillating pressure whilst recording the sensors measurements. The results showed a 9% variation from the mean pressure, see Figure 3.8. This suggested that the sensors had varying response times which inspired the need for a dynamic response test.

Three Hottinger Baldwin Messetechnik (HBM) differential pressure transducers were sourced. The difference between the HBM and EH sensors is that the HBM sensors use strain gauges within a very small cavity volume. The EH sensor rely on feedback from a diaphragm housed inside a cavity which is relatively larger than that of the HBM sensors. The dynamic response test involved connecting three HBM

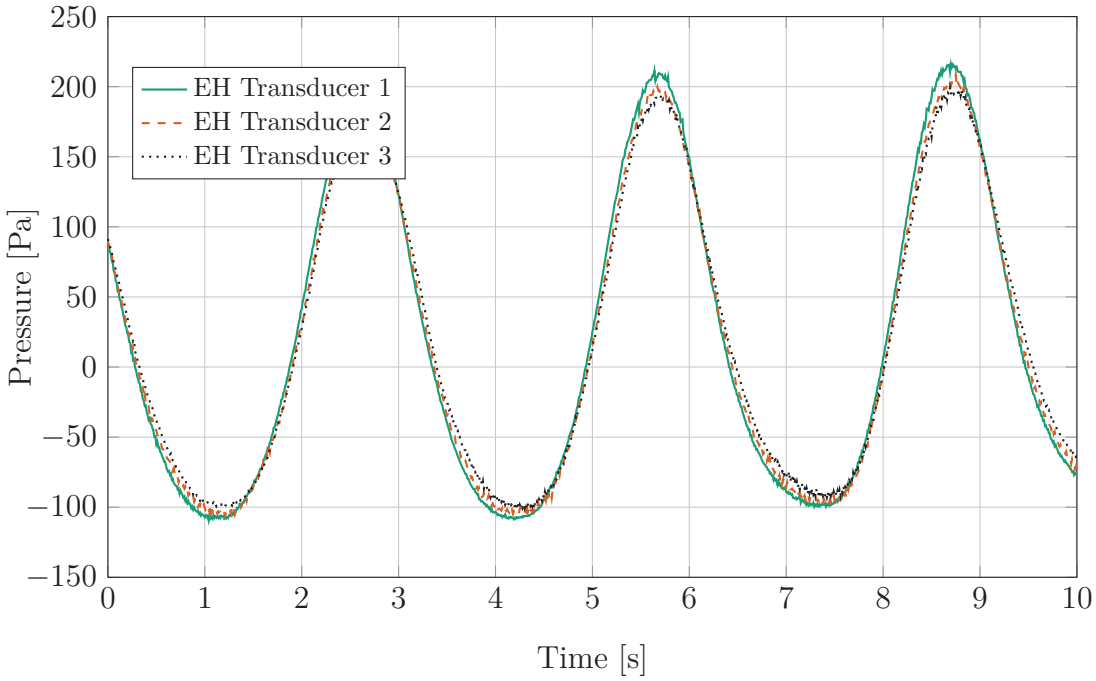

Figure 3.8: Endress & Hauser dynamic pressure consistency check.

transducers and one EH transducer to the same point. Short impulses of pressure were then applied to the devices and their pressure measurements were recorded.

Figure 3.9 shows that the three HBM pressure transducers have the same response to the various impulses. The HBM transducers display marginal overshoot but very fast response and settling time (about 6 ms) whereas the EH transducer shows a much longer response time (about 70 ms longer than the HBM sensors) as well as a longer settling time (about 300 ms longer than the HBM sensors). This proved that the HMB transducers would be a better option for recording oscillating pressures.

A final comparison was carried out by connecting all four of the transducers to the oscillating pressure point with a similar frequency to the scale model tests. Figure 3.10 confirms that the response and settling time of the two types of sensors play a major role in the pressures recorded. It shows that the EH transducers filtered out a substantial amount of data compared to the HBM transducers. The slower response time also lead to a phase shift in the measured data. These effects would have resulted in the measurement of apparent losses in the system if the EH sensors had been used.

The pressure transducers were set up in position using three clamps, as seen in Figure A.3 in Appendix A. This was done to ensure that they did not change position after calibration. The HBM transducers were calibrated three times before testing the Surface SWEC configuration, and once again before testing the Submerged SWEC configuration. The calibration curves for each transducer proved to stay unchanged throughout the various calibrations.

The transducers were connected to the SWEC device via 4 mm diameter plastic

pipes. An investigation was carried out on the effect the pipes had on the pressure measurements. This affect was analysed by applying dynamic pressures to the transducers using long pipes (3 m) compared to the recorded measurements using shorter pipe lengths (0.5 m). The results showed that the change in pipe length had a negligible effect on the measurements.

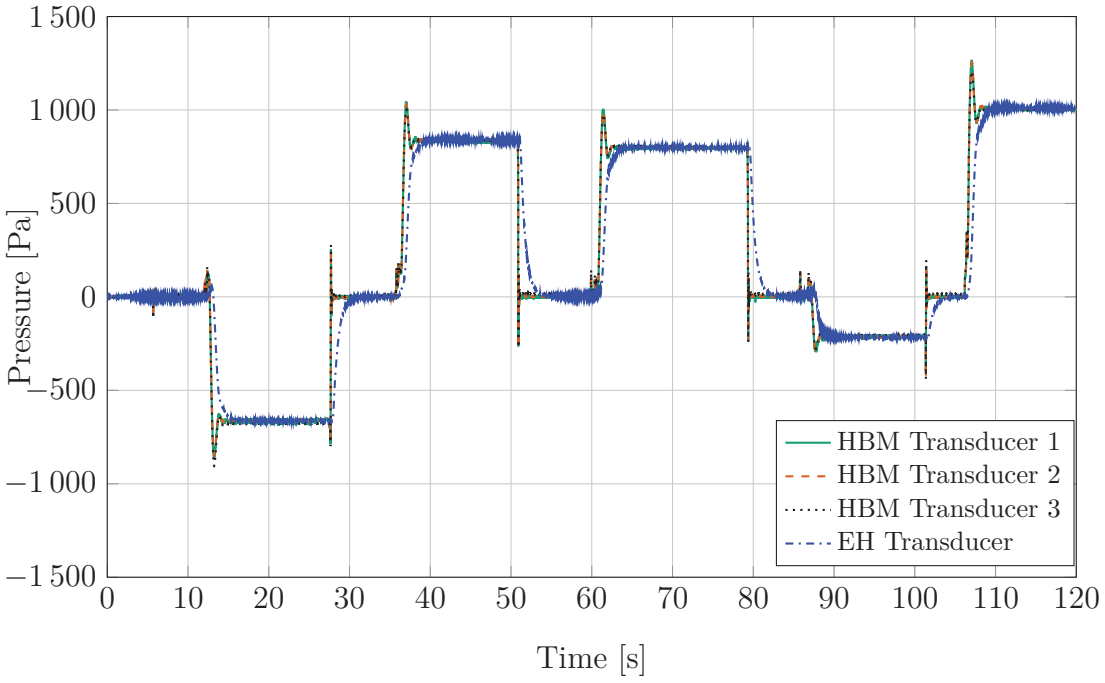

Figure 3.9: Dynamic response comparison.

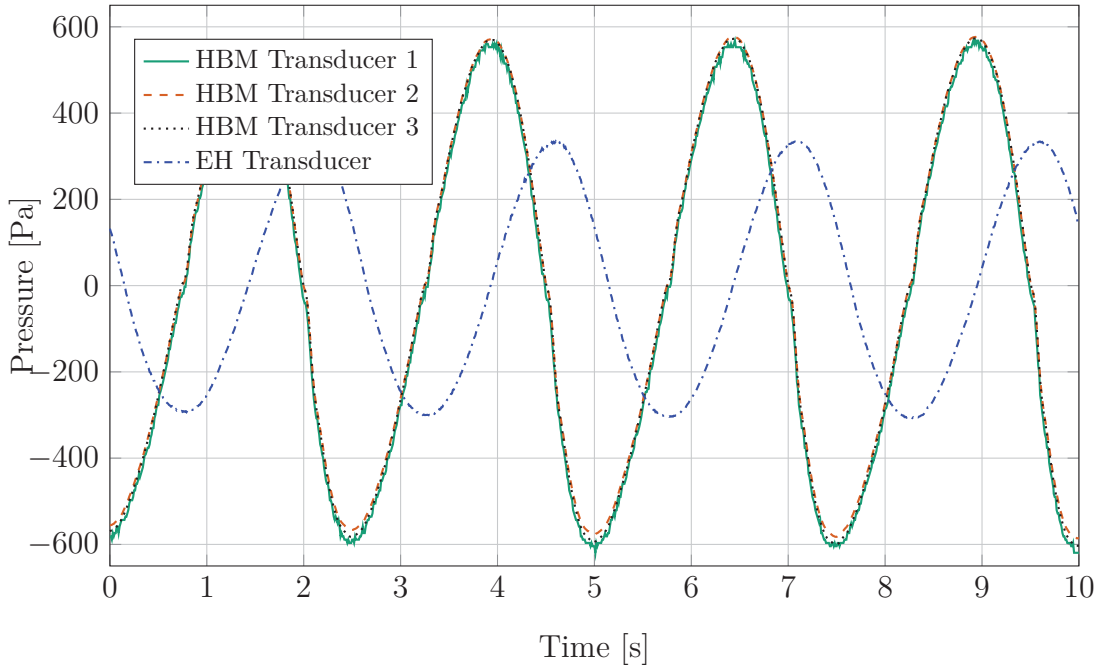

Figure 3.10: Oscillating pressure comparison.

3.2.5 Orifice flow meter

The airflow system is made up of an outlet duct leading from the chamber, an orifice plate and an additional duct which feeds into an auxiliary chamber. The orifice flow meter is made up of the two ducts, the orifice plate and 4 pressure tappings. The orifice flow meter serves two main purposes. Firstly, it allows for the volumetric flow rate in the system to be measured by calibrating the relationship of volumetric flow rate to pressure drop over the plate. Secondly, it acts as a power take-off mechanism.

An orifice plate provides a damping load similar to that of a turbine and has been successfully used to represent a turbine in many other studies (Joubert, 2013, Zhang, Zou and Greaves, 2012, Thiruvenkatasamy and Neelamani, 1997 and Kooverji, 2011). Equation 3.2 is used to describe the instantaneous pneumatic PTO and is used to determine the converted power $P_{conv}(t)$. Adaptations to the original orifice flow plate include lengthening the 'upper' duct. This was done in order to make the orifice flow meter symmetrical around the orifice plate. The orifice flow meter was constructed in adherence to international standard 5167-2 (ISO, 2003).

$$P_{conv}(t) = \dot{V}(t)\Delta p(t) \tag{3.2}$$

In Equation 3.2, $\dot{V}(t)$ is the volumetric flow rate in the system and $\Delta p(t)$ is the pressure difference between the chamber and the atmosphere or auxiliary volume. A derivation check is carried out on the units of this equation. $P_{conv}(t)$ has the unit of Watt which is equivalent to the SI units shown in Equation 3.3.

$$Watt = \frac{Nm}{s} = kg\frac{m^2}{s^3} \tag{3.3}$$

The units for volumetric flow multiplied by pressure difference can be seen in Equation 3.4,

$$\dot{V}(t)\Delta p(t) = \frac{m^3}{s}\frac{N}{m^2} = kg\frac{m^2}{s^3} \tag{3.4}$$

These two unit expressions support Equation 3.2 and due to it being widely used to compute the PTO for an orifice flow plate, it is accepted for this research. The orifice flow meter was designed and positioned based on the following aspects:

- Minimise overhead pressure influences.
- Minimise pipe losses.
- Increase versatility for various chamber orientations.
- Reduce cost.
- Ease of assembly and calibration.
- Ease of modelling the losses.

The orifice flow meter was designed to be attached to the top of the chamber based on findings from Dizadji and Sajadian (2010) which showed that placing the outlet duct on top of the chamber produced the highest volumetric flow rates. The duct diameter was chosen to reduce pipe friction while at the same time keeping the Helmholtz resonance phenomenon in mind.

The orifice flow meter was designed to ensure that the Helmholtz resonance phenomenon did not occur as exciting the meter at a resonant frequency could lead to runaway vibrations, physical damage and additional losses. This was done by sizing the ducts and the chambers accordingly. Helmholtz and Hermann (1895) show that resonance for a system with a neck leading into a larger cavity occurs at a frequency f_H shown in Equation 3.5.

$$f_H = \frac{c_s}{2\pi}\sqrt{\frac{A_d}{V_{c/aux}L_{eq}}} \tag{3.5}$$

Where the orifice flow meter duct is seen as the neck, the chamber and auxiliary volume are seen as cavities. The SWEC chamber represents the cavity when the air is travelling in the negative z-direction and the auxiliary volume represents the cavity when the airflow is positive. Calculations for the Helmholtz resonance frequency can be seen in Appendix A. The Helmholtz frequencies prove to be 65.5 Hz for the negative flow and 2.33 Hz for positive flow. The frequencies tested in this study range from 0.31 Hz to 0.67 Hz and therefore the Helmholtz resonance phenomenon was not a concern during testing.

The orifice plate is inserted between the lower and upper airflow ducts and as previously mentioned, it serves as the PTO mechanism for this study. The hole in the orifice plate has a smaller diameter than the airflow ducts. The sudden constriction and expansion of air caused by the orifice plate produces vortex regions before and after the plate. These vortex regions are the areas of energy and power dissipation. This mechanism's applied damping greatly influences the conversion efficiency of the OWC device and therefore five different orifice plates were tested.

Table 3.5: Orifice plate sizes.

Plate number	Hole diameter (m)	Area ratio (A_{op}/A_{ch})
1	0.014	0.14%
2	0.019	0.25%
3	0.027	0.5%
4	0.038	1%
5	0.047	1.5%

The orifice plates are referred to by the ratio between the orifice area and the inner surface area of the chamber. Joubert (2013) found that an orifice plate hole with an area 0.7% of the chamber surface area produced the greatest efficiency.

Thiruvenkatasamy and Neelamani (1997) found that an orifice area to chamber area ratio of 0.81% allowed for maximum power conversion. See Table 3.5 for the orifice plate sizes and the respective area ratios which were used for this project.

The calibration of the orifice flow meter was carried out in the Heat Transfer Laboratory at Stellenbosch University and is explained in the next section. Figure A.4 in Appendix A shows a 3D model of the flow meter.

Calibration

The orifice flow meter was calibrated by drawing a known volumetric flow rate of air through it whilst recording the pressure drop over the plate. The known volumetric flow rate was produced using a very accurate DISA calibration unit. Figure A.6 in Appendix A shows a photo of the calibration set-up. Figure A.5 in Appendix A shows the data which was used to generate the calibration curves described by the functions in Table 3.6.

The data in Figure A.5 was used to generate trend lines which describe the relationship between the pressure drop over a specific plate to volumetric flow rate through the system. The trend lines are assumed to apply for both forward and reverse flow due to the symmetry of the orifice plates and orifice flow meter. See Table 3.6 for the plates and the corresponding trend line function.

Table 3.6 also displays the R^2 value for each function. This is a measure of how well the trend line functions match the experimental data. All the R^2 values are above 0.99 indicating that the trend lines fit the experimental data very well. The choice between using either a polynomial or logarithmic trend-line was dependent on which trend line achieved a higher R^2 value.

Table 3.6: Orifice plate trend line functions.

Plate	Trend-line expressions	R^2
0.14%	$\dot{V}(x) = 0.005x^{0.474}$	0.999
0.25%	$\dot{V}(x) = -0.475x^6 + 1.335x^5 - 1.475x^4 + 0.786x^3 - 0.225x^2 + 0.04x$	0.998
0.5%	$\dot{V}(x) = -0.193x^4 + 0.34x^3 - 0.206x^2 + 0.062x$	0.995
1%	$\dot{V}(x) = 0.031x^{0.498}$	0.999
1.5%	$\dot{V}(x) = 0.049x^{0.515}$	0.998

3.2.6 Auxiliary volume

The Submerged SWEC configuration requires a static water level inside the chamber which is lower than the flumes static water level. In order to do this, the system had to be pressurised and therefore the system needed to be airtight. This meant that an auxiliary volume had to be added to the top of the orifice flow meter. In an ideal case, the auxiliary volume would be infinite in volume. This would allow the system to be pressurised but also allow air to flow due to the compressibility of

air. Of course an infinite volume was not possible, therefore the size of the auxiliary volume needed to be investigated.

The smaller the auxiliary volume, the more restricted the air flow would be due to a rapid build up in pressure. The system is assumed to be isentropic and thus adiabatic and reversible. This introduces the isentropic expression describing the relationship between pressure and volume, see Equation 3.6.

$$pV^{\gamma} = constant \tag{3.6}$$

Where γ is the heat capacity ratio. Various theoretical auxiliary volume sizes were investigated by analysing the static pressure increase in the system when decreasing the volume by a specific amount. The largest possible amplitude inside the chamber is equal to 0.12 m, the length of the chamber lip. Therefore 0.12 m was used to calculate the decrease in volume. An overall system pressure increase of less than 0.5% was deemed acceptable and assumed to have a negligible restricting effect on the air flow. See Table 3.7 for various auxiliary volume sizes and the overall pressure percentage increase due to the decrease in volume.

Table 3.7: Auxiliary volume sizes.

Volume decrease (m^3)	Auxiliary volume (m^3)	Percentage pressure increase (%)
0.014	0.166 (166 litre drum)	11%
0.014	1 (1 000 litre drum)	2%
0.014	2.5 (2 500 litre drum)	0.8%
0.014	4 (4 000 litre drum)	0.5%
0.014	5 (5 000 litre drum)	0.4%

The 5 000 litre drum achieved an overall percentage pressure increase of less than 0.5%. It was assumed that an auxiliary volume of that size would have a negligible restrictive effect on the mass flow rate in the system. Appendix A shows an example of the calculations used to determine the percentage increase in pressure.

3.2.7 Data acquisition unit and instrumentation connections

This section provides an overview of the data acquisition (DAQ) unit used to capture the measured data as well as a instrument schematic diagram. The DAQ unit used for this project allows for eight inputs and can be seen in Figure A.7 in Appendix A. Seven of the eight inputs were utilised; four were used for wave probes and three for differential pressure transducers. The DAQ was connected to a laptop which ran the data acquisition software (HR DAQ). The calibration of the wave probes and pressure sensors was also carried out using this software.

The measurements from the wave probes and the pressure sensors are sent to the DAQ unit which scaled the signals to a voltage value ranging between -10V and +10V. The voltage values are then sent to a laptop where the calibration curves are

applied in order to produce results expressed with the correct unit. See Figure A.8 for an instrument schematic layout.

Figure A.8 in Appendix A shows the HBM pressure transducers (1) connected to a QuantumX DAQ unit(2). This unit provides the sensors with power and allows the measured signals to be transferred to a Bayonet Neill-Concelman (BNC) cable. This was necessary as the HR Wallingford DAQ uses BNC cables as an input. Figure A.8 also shows the wave probes (3) connected to the HR Wallingford DAQ (4) which is then finally connected to a laptop (5) which records the required measurements.

3.2.8 Camera and wave speed measurements

The simulation model requires three main wave characteristic values to form an accurate input wave. These values include wave height, wave period and wavelength. The average wave height and wave period were calculated using the data recorded by the wave probes whilst the wavelength data proved to be more complex to collect.

There are various methods of recording or estimating wavelength. However the accuracy of these methods varies. The first method that was considered was using Equation 3.7 which defines wavelength for a wave produced in shallow water (McCormick, 1981). The fact that the experimental input wave conditions fall into the transitional wave depth suggested that this method would be inaccurate.

$$\lambda = \sqrt{gh}T \tag{3.7}$$

The more complex Equation 3.8 that defines wavelength for waves in any depth was consulted. This more complex equation required an iterative Matlab script to be written in order to solve for λ. The script is explained in Appendix B.

$$\lambda = \frac{gT^2}{2\pi} \tanh\left(\frac{2\pi h}{\lambda}\right) \tag{3.8}$$

An investigation into the accuracy of the previous two equations for λ was conducted. A camera was set up and recorded waves passing two marks which were placed exactly 1 m apart. This was done for a range of wave periods. The video footage was analysed and the speed of the passing waves was defined by recording the time it took for the waves to pass from one mark to the next. The wavelength was then calculated by multiplying the wave speed by wave period.

The recorded wavelengths, the wavelengths predicted by Equation 3.7 and wavelengths recorded by Equation 3.8 are shown in Figure A.9 in Appendix A. It is clear that the more complex Equation 3.8 estimates the wavelength with a higher degree of accuracy and therefore was used to estimate the wavelength for the input model.

Chapter 4

Simulation model development

This section describes the simulation models developed in order to describe both the Surface and Submerged SWEC dynamics. The Surface SWEC model is presented first followed by the Submerged SWEC model. Both models are introduced with a schematic diagram describing the respective system. This is followed by a detailed derivation of the hydrodynamic and thermodynamic aspects of the model.

4.1 Surface SWEC model

The Surface SWEC model was derived first as it is considered to be less complex than the Submerged SWEC model. The main difference between the Surface SWEC and Submerged SWEC is that the top of the Surface SWEC protrudes out of the water. For the Surface SWEC the still water level inside the chamber is in line with the still water level of the ocean. The pressure differential which causes mass to flow exists between the chamber pressure, p_c, and the atmosphere p_{atm}. See Figure 4.1 for a schematic of the Surface SWEC configuration. The equations which describe the hydrodynamic and thermodynamic relationships within the system are presented. These relationships determine the power available and power converted by the SWEC chamber.

The models developed for this project use the same principles and assumptions as the model derived in Gervelas *et al.* (2011). The most influential changes made include the changes made to the expressions used to model the orifice PTO mechanism and the added mass phenomena. The model derived by Gervelas *et al.* (2011) assumes the water in the chamber to be a solid vertical cylinder; the water column is modelled in a different manner for this project. This allows for the mass of water to be represented as a cuboid which is consistent with the shape of the chamber. The models derived in this project make use of linear wave theory in conjunction with work done on air cavities trapped in marine vehicles by Patel (1978).

Various assumptions were made in order to simplify the derivation of the state equations required to describe both systems. Firstly, incoming waves are assumed to be unaffected by the SWEC structure. In practice this is not the case as reflected

waves will have an effect on the incoming waves. Secondly, the water column inside the chamber is assumed to be a solid vertical mass with a flat water surface. The water surface was monitored during testing to ensure the validity of this assumption. The turbulence present in the water column as well as the air chamber and outlet duct is not modelled, but is instead included as a loss term.

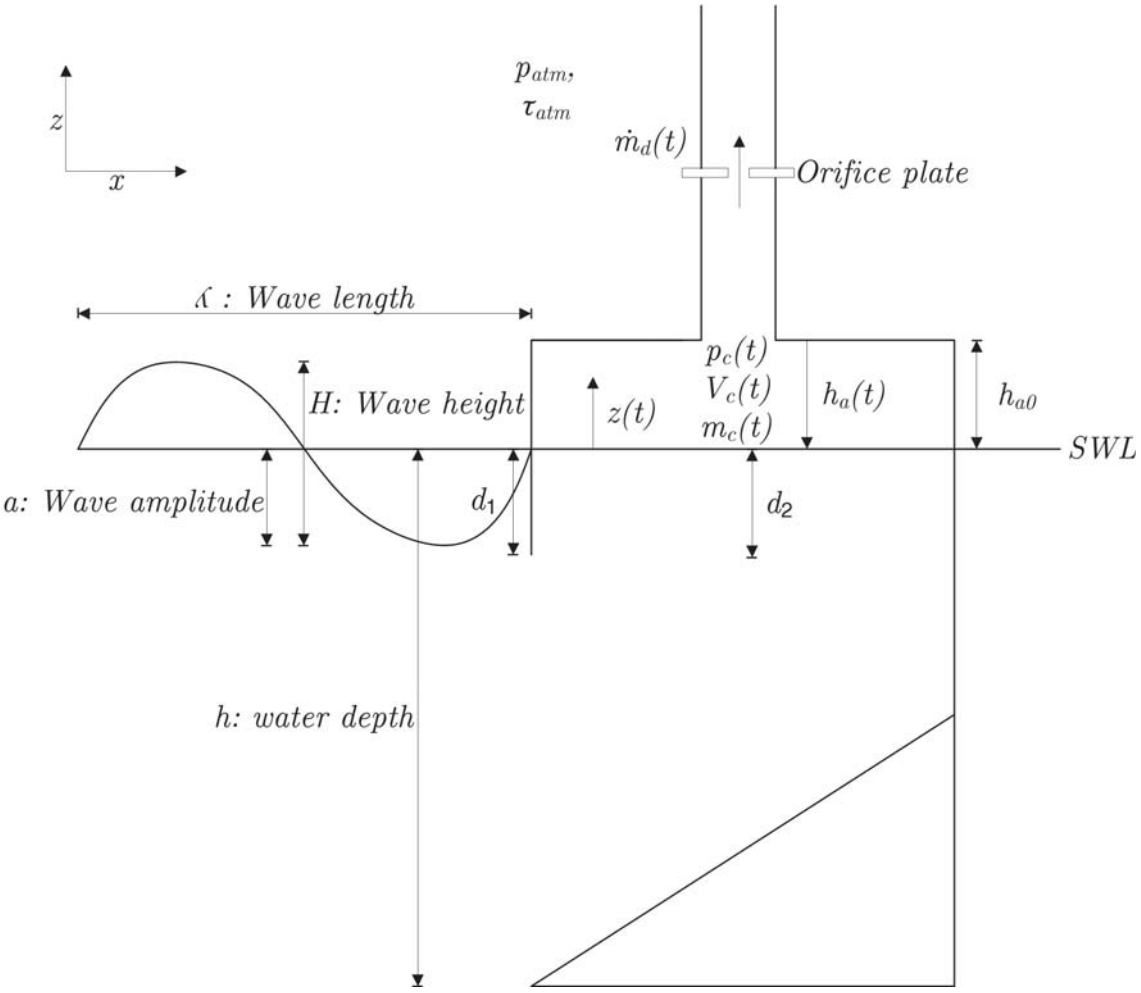

Figure 4.1: Surface SWEC schematic.

The volumetric flow rate throughout the orifice flow meter is assumed constant due to its small volume and the assumption that the change in density of the air throughout the flow meter is negligible. Finally, the compression and decompression process of the air trapped inside the chamber is considered to be an isentropic process. This means the process is assumed to be adiabatic and reversible.

The assumptions are restated in bullet form for convenience:

- Water plug in chamber represented as a solid cuboid with a flat water surface.
- Linear wave theory is assumed to be an accurate method of modelling the incoming waves.
- The incoming waves are assumed to be unaffected by the SWEC structure.

- Turbulence, viscosity and vortex shedding are not modelled but included as a combined loss term.
- Volumetric flow rate throughout orifice flow meter is assumed to be constant.
- Compression and decompression of air inside chamber is assumed to be an isentropic process.
- Flow inside the orifice meter is assumed to be turbulent due to the oscillatory nature.

4.1.1 Surface SWEC hydrodynamics

The first part of the system to be modelled is the movement of the water column inside the chamber and the corresponding water level displacement $z(t)$. Newton's second law is applied to the volume of water which presents the following,

$$M_c\ddot{z}(t) + B\dot{z}(t) + Cz(t) = F(t) \tag{4.1}$$

Where M_c is the mass of the water column, B is the damping coefficient and C is the hydrostatic restoring coefficient. The damping coefficient is assumed to be a function of the mass M_c as well as the added mass, M_a. The hydrostatic restoring force is assumed to be 10% of the critical restoring coefficient (Patel & Harrison, 1985). If $(a'b')$ represents the area of the water column, then M_c, B and C are defined as:

$$M_c = \rho_w(a'b')\left[d_2 + z(t)\right] \tag{4.2}$$

$$B = 0.2\sqrt{C(M_c + M_a)} \tag{4.3}$$

$$C = \rho_w g(a'b') \tag{4.4}$$

Past studies have shown that the added mass associated with the SWEC proved to be a difficult characteristic to define. The theory of added mass was therefore researched in detail and is presented in Chapter 2. Dong (1978) shows that the added mass for a system such as the SWEC is dependent on the area of the chamber's free water surface and the density of water. Equation 4.5 is used to calculate the added mass relevant to this system.

$$M_a = \frac{0.84}{2}\rho_w \pi a' \frac{b'^2}{4} \tag{4.5}$$

The total force acting on the bottom of the water column is made up of three forces. Firstly the added mass force $F_a(t)$ which acts as a damping force. Secondly the Froude-Krylov force, $F_{FK}(t)$, which is present at the bottom of the water column and drives the water upwards and thirdly the force due to varying air pressure in the

chamber, $F_{\Delta p}(t)$. See Figure 4.2 for a free body diagram which shows the column of water and the three forces acting on it when moving in the positive z-direction.

Setting up a force balance equation results in,

$$F(t) = F_{FK}(t) - F_a - F_{\Delta p}(t) \tag{4.6}$$

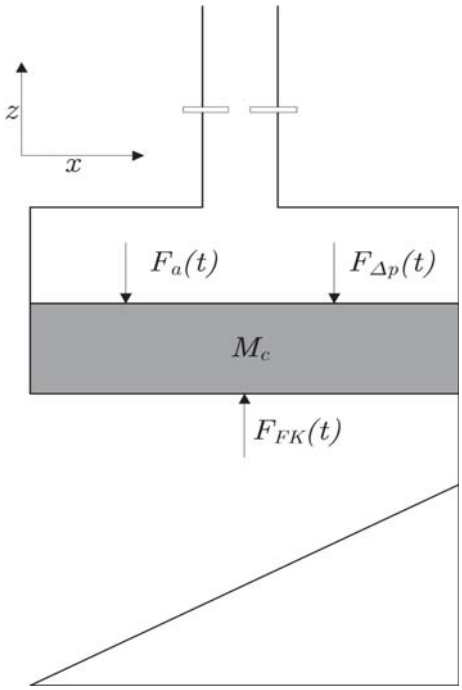

Figure 4.2: Surface SWEC free body diagram.

The Froude-Krylov force is caused by the water particle movement and is expressed by,

$$F_{FK}(t) = p_{wave}(t) \times (a'b') \tag{4.7}$$

Where $p_{wave}(t)$ is the hydrodynamic pressure at the bottom of the water column. The expression for $p_{wave}(t)$ is provided by linear wave theory and can be seen in Equation 4.8.

$$p_{wave}(t) = \rho_w g a \frac{cosh\left[k(h - d_1)\right]}{cosh(kh)} cos(\omega t + \phi) \tag{4.8}$$

The general expression for the added mass force is defined as,

$$F_a(t) = M_a[\dot{w}(t) - \ddot{z}(t)] \tag{4.9}$$

Where $\dot{w}(t) - \ddot{z}(t)$ represents the relative vertical acceleration of the surrounding

fluid to the acceleration of the water column. Linear wave theory is used once again to express $w(t)$ and $\dot{w}(t)$.

$$w(t) = \omega a \frac{sinh\left[k(h-d_1)\right]}{sinh(kh)} sin(\omega t + \phi) \tag{4.10}$$

$$\dot{w}(t) = \omega^2 a \frac{sinh\left[k(h-d_1)\right]}{sinh(kh)} cos(\omega t + \phi) \tag{4.11}$$

Where ω is angular frequency, a is the wave amplitude, k is the wave number and ϕ is the wave phase shift. By combining Equations 4.11 and 4.9, an expression for the added mass force is derived.

$$F_a(t) = M_a \left(\omega^2 a \frac{sinh\left[k(h-d_1)\right]}{sinh(kh)} cos(\omega t + \phi) - \ddot{z}(t) \right) \tag{4.12}$$

Finally the air force on the column due to the differential pressure present can be expressed as,

$$F_{\Delta p}(t) = \Delta p(t) \times (a'b') \tag{4.13}$$

Where $\Delta p(t) = p_c(t) - p_{atm}$. In order to simplify the equation of motion, α and β are introduced (Gervelas et al., 2011).

$$\alpha = d_2 + \frac{M_a}{(a'b')} \tag{4.14}$$

$$\beta = \frac{g \times cosh\left[k(h-d_1)\right]}{cosh(kh)} - \frac{M_a \omega^2}{(a'b')\rho_w} \frac{sinh[k(h-d_1)]}{sinh(kh)} \tag{4.15}$$

Substituting α and β into the equation of motion results in a simplification in the form,

$$[\alpha + z(t)]\ddot{z}(t) + 0.2\sqrt{g[\alpha + z(t)]}\dot{z}(t) + gz(t) = \beta a \times cos(\omega t + \phi) - \frac{\Delta p(t)}{\rho_w} \tag{4.16}$$

Rearranging,

$$\ddot{z}(t) = -0.2\sqrt{\frac{g}{[\alpha + z(t)]}}\dot{z}(t) - \frac{gz(t)}{[\alpha + z(t)]} + \frac{\beta a \times cos(\omega t + \phi)}{[\alpha + z(t)]} - \frac{\Delta p(t)}{\rho_w[\alpha + z(t)]} \tag{4.17}$$

Equation 4.17 is the first state equation introduced and contains three unknown time varying variables, $z(t)$, $\dot{z}(t)$ and $\Delta p(t)$. $z(t)$ and $\dot{z}(t)$ are solved using a graphical

programming environment for modelling dynamic systems, SIMULINK. An expression for $\Delta p(t)$ is derived in the next section. All state equations are highlighted again towards the end of this chapter.

4.1.2 Surface SWEC thermodynamics

This section describes the governing equations used to model the thermodynamic relationships for the Surface SWEC system. The procedures follow the same methodology presented in Gervelas *et al.* (2011). The state equation used to describe $\Delta p(t)$ is derived using the ideal gas equation seen in Equation 4.18.

$$p_c(t)V_c(t) = m_c(t)R^*\tau_c(t) \tag{4.18}$$

Where $p_c(t)$ is the pressure inside the chamber, $V_c(t)$ is the volume of air inside the chamber and $m_c(t)$ is the mass of air inside the chamber. R^* is the specific gas constant for air and $\tau_c(t)$ is the temperature of the air inside the chamber. Differentiating the ideal gas equation with respect to time leads to,

$$p_c(t)\frac{\partial V_c(t)}{\partial t} + V_c(t)\frac{\partial p_c(t)}{\partial t} = R^*\tau_c(t)\frac{\partial m_c(t)}{\partial t} + m_c(t)R^*\frac{\partial \tau_c(t)}{\partial t} \tag{4.19}$$

Dividing through by $V_c(t)$ and substituting Equation 4.20 into Equation 4.19 results in Equation 4.21.

$$\frac{p_c(t)}{\tau_c(t)} = \frac{m_c(t)R^*}{V_c(t)} \tag{4.20}$$

$$\frac{p_c(t)}{V_c(t)}\frac{\partial V_c(t)}{\partial t} + \frac{\partial p_c(t)}{\partial t} = \frac{R^*\tau_c(t)}{V_c(t)}\frac{\partial m_c(t)}{\partial t} + \frac{p_c(t)}{\tau_c(t)}\frac{\partial \tau_c(t)}{\partial t} \tag{4.21}$$

In the same fashion as Gervelas *et al.* (2011), the compression and decompression process of the air trapped inside the chamber is considered to be an isentropic process. This means the process is assumed to be adiabatic and reversible. This assumption allows for the following expression to hold true,

$$p_c(t)V_c(t)^\gamma = constant \tag{4.22}$$

Where γ is the heat capacity value. A manipulated form of the ideal gas law, seen in Equation 4.23, is substituted into Equation 4.22, resulting in Equation 4.24.

$$V_c(t)^\gamma = \left[\frac{m_c(t)R^*\tau_c(t)}{p_c(t)}\right]^\gamma \tag{4.23}$$

$$p_c(t)^{1-\gamma}\tau_c(t)^\gamma = constant \tag{4.24}$$

Taking the log on both sides of Equation 4.24 and then differentiating with regards to time results in,

$$\frac{p_c(t)}{\tau_c(t)}\frac{\partial \tau_c(t)}{\partial t} = \frac{\gamma - 1}{\gamma}\frac{\partial p_c(t)}{\partial t} \tag{4.25}$$

Substituting Equation 4.25 into Equation 4.21 results in,

$$\gamma\frac{p_c(t)}{V_c(t)}\frac{\partial V_c(t)}{\partial t} + \frac{\partial p_c(t)}{\partial t} = \frac{\gamma R^* \tau_c(t)}{V_c(t)}\frac{\partial m_c(t)}{\partial t} \tag{4.26}$$

An expression used to describe the relationship between the differential pressure and the mass flow rate through the orifice duct is required. Firstly the mass flow rate is defined as positive when air leaves the chamber. The flow is assumed to be turbulent due to its oscillatory nature with relatively high frequencies. An equation was set up to define the losses which occur due the various restrictions present in the system. The loss expression comprises of three main components namely, friction losses, contraction losses and expansion losses.

A methodology similar to that found in Holtz (2007) is followed in order to define the various loss coefficients in the system. Losses in a flowing fluid are often presented as a pressure drop, $\Delta p(t)$. They can also be defined in the form of a head loss which is related to pressure drop though the fluid mechanic relationships seen in Equation 4.32 (Cengel & Cimbala, 2006). The losses are first presented in the form of a head loss and then in the form of a pressure drop. Equation 4.27 shows the general form of the head loss equation.

$$h_L(t) = K\frac{[U_d(t)]^2}{2g} \tag{4.27}$$

Where K is the loss coefficient and $U_d(t)$ is the velocity of the air in the outlet duct. The friction loss coefficient, K_f, is defined using the Darcy-Weisbach equation, valid for both laminar and turbulent flows (Potter & Wiggert, 2002).

$$K_f = f\frac{L_d}{d_d} \tag{4.28}$$

Where f is the friction factor, L_d is the length of the orifice duct and d_d is the diameter of the orifice duct. The friction factor is determined by using Equation 4.29.

$$f = \frac{1}{\left[-0.86ln\left(\frac{\epsilon}{3.7d_d}\right)\right]^2} \tag{4.29}$$

Where ϵ is the surface roughness. Due to the flow being oscillatory, the losses at the junction between the chamber and orifice flow meter are seen as contraction

losses when the flow is positive and expansion losses when the flow is negative. Loss coefficients for both contraction and expansion had to be determined. Jenkinson (2014) shows that Equation 4.30 is used to calculate the expansion coefficient and Figure 4.3 is used to define a contraction coefficient.

$$K_e = \left(1 - \frac{A_d}{A_c}\right) \tag{4.30}$$

Where A_c is the cross sectional area of the chamber and A_d is the cross sectional area of the orifice flow duct protruding from the chamber.

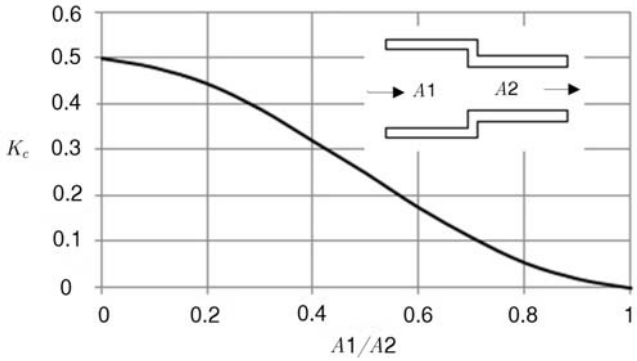

Figure 4.3: Contraction loss coefficient (Amirault, 2015).

Due to the fact that the head loss components vary in cross sectional area, the velocity of the air differs for different loss components. This knowledge lead to the use of volumetric flow rate, $\dot{V}_d(t)$, divided by the specific area of each loss component to represent the velocity at that component. Combing the various losses in the system results in a total head loss equation, see Equation 4.31.

The K_{op} loss factor in Equation 4.31 represents all the losses over the orifice plate. This value was determined by analysing the pressure drop over the various orifice plates and then comparing them to the volumetric flow rate. The K_{op} factor was the only variable which was adjusted when matching the experimental and simulation results. It must be stated that this value was only adjusted once for each orifice plate and was kept constant when simulating the Submerged SWEC.

$$h_L(t) = K_f \frac{\left[\dot{V}_d(t)\right]^2}{A_d^2 \times 2g} + K_{ec} \frac{\left[\dot{V}_d(t)\right]^2}{A_d^2 \times 2g} + K_{op} \frac{\left[\dot{V}_d(t)\right]^2}{A_{op}^2 \times 2g} \tag{4.31}$$

K_{ec} represents the contraction coefficient when flow is positive and the expansion coefficient when flow is negative. A_{op} is the area of the hole in the orifice plate. The energy equation for pipe flow (Equation 4.32) is introduced in order to describe the relationship between head loss, volumetric flow rate and the pressure differential between the chamber and the atmosphere.

$$h_L(t) = \frac{\Delta p(t) + \zeta L_d}{\zeta} \tag{4.32}$$

Where $\zeta = \rho_a(t)g$ and $\Delta p(t) = p_c(t) - p_{atm}$, thus $\dot{\Delta} p(t) = \dot{p_c}(t)$, the rate of change of pressure in the chamber. The height difference L_d due to the orifice duct is neglected since the specific weight of air is very small. Substituting Equation 4.32 into Equation 4.31 whilst making $\dot{V_d}(t)$ the subject of the equation results in,

$$\dot{V_d}(t) = \sqrt{\frac{2g\Delta p(t)}{\zeta\left(\frac{K_f + K_{ec}}{A_d^2} + \frac{K_{op}}{A_{op}^2}\right)}} \tag{4.33}$$

Using Equation 4.33 one multiplies by $\rho_a(t)$ to find an expression for mass flow rate $\dot{m_d}(t)$.

$$\dot{m_d}(t) = \sqrt{\frac{2\rho_a(t)|\Delta p(t)|}{\left(\frac{K_f + K_{ec}}{A_d^2} + \frac{K_{op}}{A_{op}^2}\right)}} \times sign[\Delta p(t)] \tag{4.34}$$

Substituting the expression for mass flow into Equation 4.26 results in the state equation for the pressure change in the chamber,

$$\dot{\Delta} p(t) = \frac{-C_s^2 C_d}{(a'b')[h_{a0} - z(t)]}\sqrt{2\rho_a(t)|\Delta p(t)|} \times sign[\Delta p(t)] + \gamma\frac{\Delta p(t) + p_{atm}}{h_{a0} - z(t)}\dot{z}(t) \tag{4.35}$$

Where C_s is the speed of sound through air and is substituted for $\gamma R^* \tau_c(t)$ (assuming the temperature change in the system to be negligible). C_d is the coefficient of discharge and can be seen in Equation 4.36. The density of air inside the chamber is used for $\rho_a(t)$ and is defined in Equation 4.37. Finally in order to produce Equation 4.35, $V_c(t)$ was substituted by $a'b'[h_{ao} - z(t)]$ and $\dot{V_c}(t)$ was substituted accordingly.

$$C_d = \frac{1}{\sqrt{\frac{K_f + K_{ec}}{A_d^2} + \frac{K_{op}}{A_{op}^2}}} \tag{4.36}$$

$$\rho_a(t) = \frac{p_c(t)}{R^* \tau_c(t)} \tag{4.37}$$

A simple diagram showing the inputs, the outputs and the theories used to produce these various outputs is shown in Figure 4.4. The full mathematical model diagram for the Surface SWEC is not presented as it is the less complex model of the two; instead the full Submerged SWEC model diagram is presented and referred to in Section 4.2.

The state equations are presented and highlighted below:

$$\dot{z}(t) = \frac{\partial z(t)}{\partial t} \tag{4.38}$$

$$\ddot{z}(t) = -0.2\sqrt{\frac{g}{[\alpha + z(t)]}}\dot{z}(t) - \frac{gz(t)}{[\alpha + z(t)]} + \frac{\beta a \times cos(\omega t + \phi)}{[\alpha + z(t)]} - \frac{\Delta p(t)}{\rho_w[\alpha + z(t)]} \tag{4.39}$$

$$\dot{m_d}(t) = \sqrt{\frac{2\rho_a(t)|\Delta p(t)|}{\left(\frac{K_f + K_{ec}}{A_d^2} + \frac{K_{op}}{A_{op}^2}\right)}} \times sign[\Delta p(t)] \tag{4.40}$$

$$\dot{m_c}(t) = -\dot{m_d}(t) \tag{4.41}$$

$$p_c(t) = \Delta p(t) + p_{atm} \tag{4.42}$$

$$\dot{\Delta p}(t) = \frac{-C_s^2 C_d}{(a'b')[h_{a0} - z(t)]}\sqrt{2\rho_a(t)|\Delta p(t)|} \times sign[\Delta p(t)] + \gamma\frac{\Delta p(t) + p_{atm}}{h_{a0} - z(t)}\dot{z}(t) \tag{4.43}$$

$$\rho_a(t) = \frac{p_c(t)}{R^* \tau_c} \tag{4.44}$$

States: $z(t), \dot{z}(t), m_c(t), \Delta p(t)$

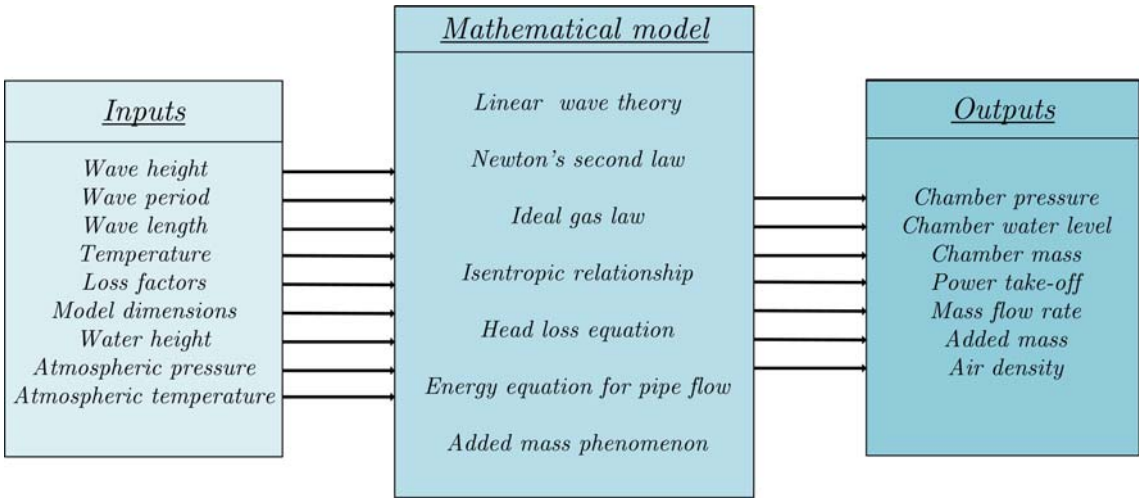

Figure 4.4: Simplified Surface SWEC model diagram.

4.2 Submerged SWEC model

As previously mentioned, the main difference between the Surface SWEC and Submerged SWEC is that the Submerged SWEC lies on the sea floor, with the top of the chamber beneath the surface of the waves. Due to this fact, d_1 and d_2 do not equal the same distance. The still water level inside the Submerged SWEC chamber

is not in line with the still water level of the ocean. The system needs to have a higher static pressure than p_{atm} and therefore an auxiliary volume is required. The pressure differential which causes mass to flow exists between the chamber pressure, p_c, and the auxiliary volume p_{aux}. See Figure 4.5 for a schematic of the Submerged SWEC configuration. The adaptations to the Surface SWEC model are presented.

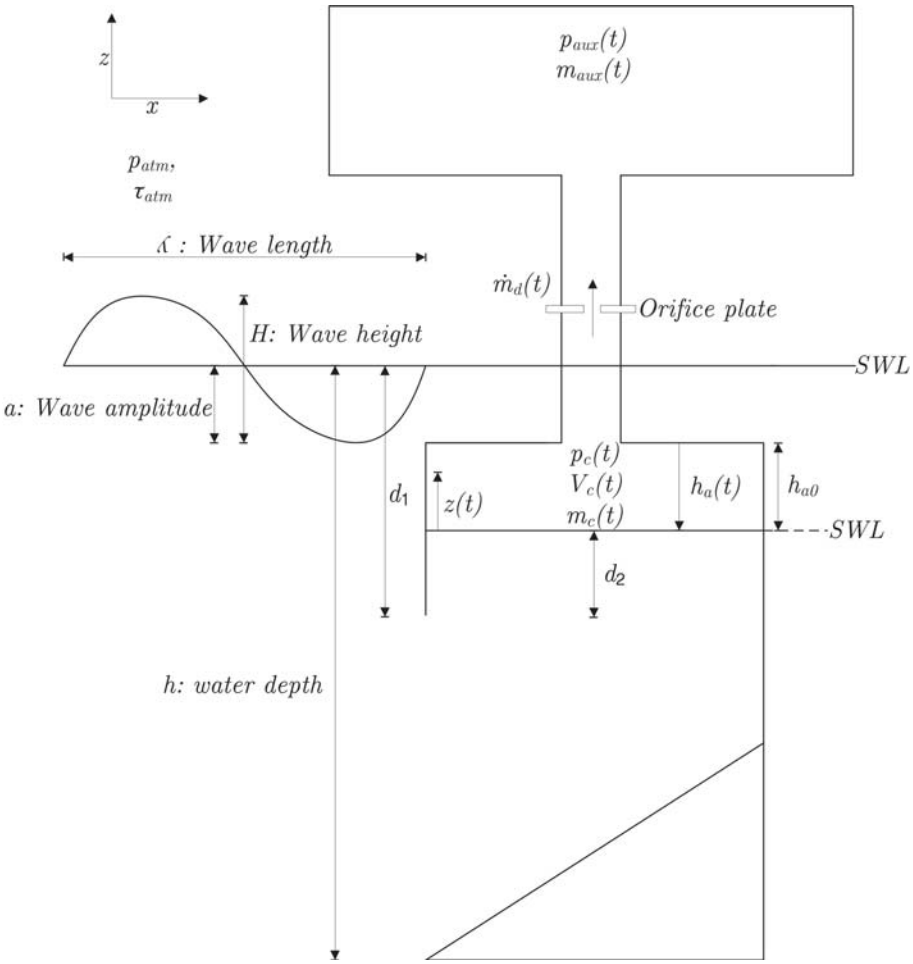

Figure 4.5: Submerged SWEC schematic.

4.2.1 Submerged SWEC hydrodynamics

The same procedure carried out on the Surface SWEC model is carried out on the hydrodynamics of the Submerged SWEC. The equations used to describe the hydrodynamics stay the same although the values used for certain characteristics change. The assumptions made as well as the state equation describing the displacement of the chamber's free water surface are repeated for convenience:

- Water plug in chamber represented as a solid cuboid with a flat water surface.
- Linear wave theory is assumed to be an accurate method of modelling the the incoming waves.
- The incoming waves are assumed to be unaffected by the SWEC structure.

- Turbulence, viscosity and vortex shedding are not modelled but included as a combined loss term.
- Volumetric flow rate throughout orifice flow meter is assumed to be constant.
- Compression and decompression of air inside chamber is assumed to be an isentropic process.
- Flow inside the orifice meter is assumed to be turbulent due to the oscillatory nature.
- The auxiliary chamber temperature is assumed to stay constant at room temperature.

$$\alpha = d_2 + \frac{M_a}{(a'b')} \tag{4.45}$$

$$\beta = \frac{g \times cosh\left[k(h-d_1)\right]}{cosh(kh)} - \frac{M_a\omega^2}{(a'b')\rho_w}\frac{sinh[k(h-d_1)]}{sinh(kh)} \tag{4.46}$$

$$\ddot{z}(t) = -0.2\sqrt{\frac{g}{[\alpha+z(t)]}}\dot{z}(t) - \frac{gz(t)}{[\alpha+z(t)]} + \frac{\beta a \times cos(\omega t+\phi)}{[\alpha+z(t)]} - \frac{\Delta p(t)}{\rho_w[\alpha+z(t)]} \tag{4.47}$$

The values which differ in this model compared to the Surface SWEC model are d_1, h and $\Delta p(t)$ which equals $p_c(t) - p_{aux}(t)$. The following subsection details the thermodynamic equations that describe the system.

4.2.2 Submerged SWEC thermodynamics

There are two significant differences between the thermodynamic models of the Surface SWEC and Submerged SWEC. The first is that there is an extra loss coefficient included in the mass flow rate equation due to the expansion and contraction into the auxiliary chamber, see Equation 4.48.

$$\dot{m}_d(t) = \sqrt{\frac{2\rho_a(t)|\Delta p(t)|}{\left(\frac{K_f+K_{ec1}+K_{ec2}}{A_d^2} + \frac{K_{op}}{A_{op}^2}\right)}} \times sign[\Delta p(t)] \tag{4.48}$$

The other significant difference is that the auxiliary chamber acts as a new 'atmosphere' for the system. Due to the fact that the auxiliary volume is very small compared to the actual atmosphere, it cannot simply be assumed that the pressure inside the auxiliary volume will stay constant. Therefore the state equation used to describe $\dot{\Delta p}(t)$ is manipulated rather to describe $p_c(t)$ and an expression for $p_{aux}(t)$ is defined. See Equations 32 and 33.

$$\dot{p}_c(t) = \frac{-C_s^2 C_d}{(a'b')[h_{a0} - z(t)]}\sqrt{2\rho_a(t)|p_c(t) - p_{aux}(t)|} \times sign[p_c(t) - p_{aux}(t)] + \gamma\frac{p_c(t)}{h_{a0} - z(t)}\dot{z}(t) \tag{4.49}$$

$$p_{aux}(t) = p_{atm} + \rho_w g(d_1 - d_2) + \frac{\Delta m_{aux}(t) R^* \tau_{aux}}{V_{aux}} \tag{4.50}$$

Where $\Delta m_{aux}(t)$ is the difference of mass in the auxiliary volume compared to static conditions and τ_{aux} is assumed to stay constant at room temperature. The air density $\rho_a(t)$ is defined by using the average density between the chamber and auxiliary volume and assuming the system temperature to be constant, see Equation 4.51.

$$\rho_a(t) = \frac{p_c(t) + p_{aux}(t)}{2R^* \tau_c} \tag{4.51}$$

The Submerged SWEC simulation model is made up of six main sub routines, and the only additional output compared to the Surface SWEC model is the time-dependent pressure inside the auxiliary volume. As the Submerged SWEC is considered the more complex system, only the simulation model diagrams for this configuration are presented in Appendix B. The state equations as well as the simplified model diagram (Figure 4.6) is repeated for the sake of consistency.

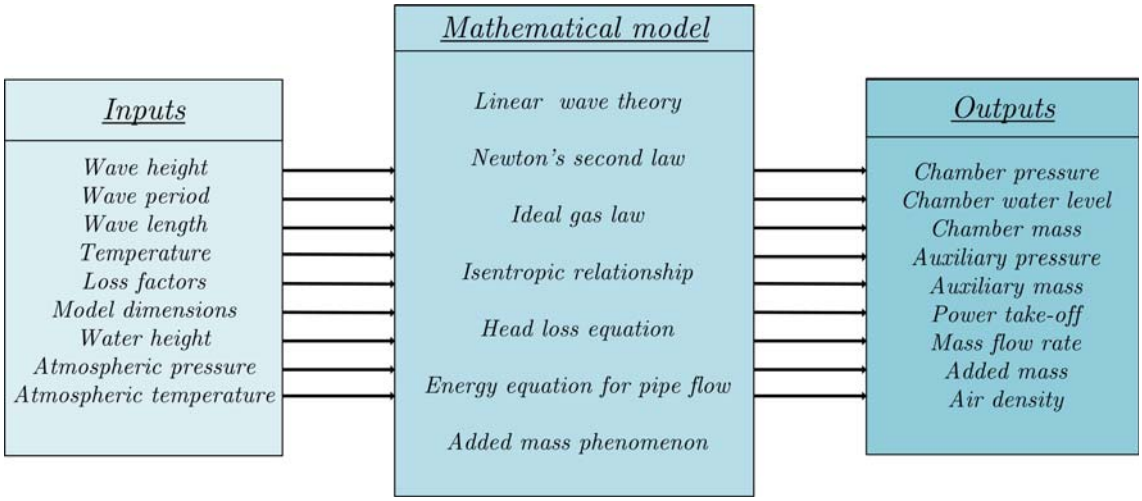

Figure 4.6: Simplified Submerged SWEC model diagram.

$$\dot{z}(t) = \frac{\partial z(t)}{\partial t} \tag{4.52}$$

$$\ddot{z}(t) = -0.2\sqrt{\frac{g}{[\alpha + z(t)]}}\dot{z}(t) - \frac{gz(t)}{[\alpha + z(t)]} + \frac{\beta a \times cos(\omega t + \phi)}{[\alpha + z(t)]} - \frac{\Delta p(t)}{\rho_w[\alpha + z(t)]} \tag{4.53}$$

$$\dot{m}_d(t) = \sqrt{\frac{2\rho_a(t)|\Delta p(t)|}{\left(\frac{K_f + K_{ec1} + K_{ec2}}{A_d^2} + \frac{K_{op}}{A_{op}^2}\right)}} \times sign[\Delta p(t)] \tag{4.54}$$

$$\dot{m}_c(t) = -\dot{m}_d(t), \text{ and } \dot{m_{aux}}(t) = \dot{m}_d(t) \tag{4.55}$$

$$p_{aux}(t) = p_{atm} + \rho_w g(d_1 - d_2) + \frac{\Delta m_{aux}(t) R^* \tau_{aux}}{V_{aux}} \tag{4.56}$$

$$\dot{p_c}(t) = \frac{-C_s^2 C_d}{(a'b')[h_{a0} - z(t)]}\sqrt{2\rho_a(t)|p_c(t) - p_{aux}(t)|} \times sign[p_c(t) - p_{aux}(t)] + \gamma \frac{p_c(t)}{h_{a0} - z(t)}\dot{z}(t) \tag{4.57}$$

$$\rho_a(t) = \frac{p_c(t) + p_{aux}(t)}{2R^*\tau_c} \tag{4.58}$$

States: $z(t), \dot{z}(t), m_c(t), m_{aux}(t), p_c(t), p_{aux}(t)$

Chapter 5

Results and discussion

This chapter starts with the evaluation of the time-dependent predictions made by the Surface and Submerged SWEC simulation models. The chapter goes on to present the transmissibility and conversion efficiency results produced by the experimental testing and simulation models. The chapter concludes with a discussion on these results and a final validation of the simulation models.

5.1 Simulation model evaluation

Three different wave scenarios for each orifice plate were used as input wave conditions for the simulation models. These wave conditions were chosen with the intention of testing the simulation models through a range of conditions which are expected to be found at the proposed deployment sites. The input wave conditions for the Surface SWEC configuration can be seen in Table 5.1.

Table 5.1: Surface SWEC simulation model input wave conditions.

Test number	Configuration	Orifice plate	H	T
1	Surface SWEC	0.25%	0.03 m	2 s
2	Surface SWEC	0.25%	0.06 m	2.5 s
3	Surface SWEC	0.25%	0.09 m	2.75 s
4	Surface SWEC	0.5%	0.03 m	2 s
5	Surface SWEC	0.5%	0.06 m	2.5 s
6	Surface SWEC	0.5%	0.09 m	2.75 s
7	Surface SWEC	1%	0.03 m	2 s
8	Surface SWEC	1%	0.06 m	2.5 s
9	Surface SWEC	1%	0.09 m	2.75 s

The input wave conditions for the Submerged SWEC configuration can be seen in Table 5.2. The wave conditions in Tables 5.1 and 5.2 not only represent the range of expected operating conditions but also allow for the simulation models to be tested

through a range of input wave power. Full scale and scaled down expected operating conditions can be found in Appendix A.

Table 5.2: Submerged SWEC simulation model input wave conditions.

Test number	Configuration	Orifice plate	H	T
10	Submerged SWEC	0.25%	0.065 m	2 s
11	Submerged SWEC	0.25%	0.09 m	2.5 s
12	Submerged SWEC	0.25%	0.11 m	2.75 s
13	Submerged SWEC	0.5%	0.065 m	2 s
14	Submerged SWEC	0.5%	0.09 m	2.5 s
15	Submerged SWEC	0.5%	0.11 m	2.75 s
16	Submerged SWEC	1%	0.065 m	2 s
17	Submerged SWEC	1%	0.09 m	2.5 s
18	Submerged SWEC	1%	0.11 m	2.75 s

The most important results include the transmissibility and conversion efficiencies. These results are calculated using four time-dependent variables namely, chamber water level $z(t)$, pressure differential $\Delta p(t)$, volumetric flow rate through the orifice flow meter $\dot{V}_d(t)$ and the converted pneumatic power $P_{conv}(t)$.

The time-dependent variables are evaluated by investigating the root mean square error (RMSE) between the simulation and experimental results. The RMSE serves as a measure of how far away, on average, the error is from zero. The RMSE% describes the error as a percentage of the RMS value of the measured data. When discussing the error between the measured and predicted time-dependent variables, it is this RMSE% which is refereed to. Equations 5.1, 5.2 and 5.3 describe the computation of RMSE, $\text{RMS}_{\text{measured}}$ and RMSE% respectively.

$$RMSE = \sqrt{\frac{\sum_{i=1}^{n}(\hat{X}_i - X_i)^2}{n}} \tag{5.1}$$

$$RMS_{measured} = \sqrt{\frac{\sum_{i=1}^{n}(X_i)^2}{n}} \tag{5.2}$$

$$RMSE\% = \frac{RMSE}{RMS_{measured}} \times 100 \tag{5.3}$$

Where $\hat{X}_i$ is the value of a certain variable X predicted by the simulation model, X_i is the experimentally measured value of the same variable and n is the number of data points. The RMSE method is used to evaluate the model's time-dependent predictions for two reasons. Firstly, it is considered to be a critical method of analysis as it compares every point of data predicted and experimentally recorded, these data points were captured at a frequency of 100 hz. Secondly, it allows for

simultaneous analysis of the model's ability to predict both form and amplitude of an oscillating variable.

Table 5.3 and Table 5.4 show the errors achieved by the Surface SWEC and Submerged SWEC simulation models. The errors higher than 20% are in bold. The error percentages for both configurations are compared and discussed and time-dependent plots are presented when necessary.

The high errors found in Tables 5.3 and 5.4 suggest that the simulation models struggle to accurately predict the time-dependent variables. Although a certain degree of error will always be present throughout the simulation results, the error percentages found in Tables 5.3 and 5.4 can be misleading.

Table 5.3: Surface SWEC simulation model error results.

Test number	$z(t)$	$\Delta p(t)$	$\dot{V}_d(t)$	$P_{conv}(t)$
1	11%	14%	15%	11%
2	13%	9%	12%	12%
3	17%	**33**%	18%	**38**%
4	6%	**26**%	**29**%	20%
5	6%	20%	14%	20%
6	**22**%	**39**%	**34**%	**48**%
7	10%	17%	20%	16%
8	10%	**26**%	18%	**21**%
9	14%	20%	20%	**32**%

Table 5.4: Submerged SWEC simulation model error results.

Test number	$z(t)$	$\Delta p(t)$	$\dot{V}_d(t)$	$P_{conv}(t)$
10	12%	12%	16%	**24**%
11	14%	18%	17%	11%
12	19%	11%	10%	17%
13	17%	**22**%	18%	**22**%
14	10%	19%	16%	18%
15	16%	20%	18%	**21**%
16	19%	**27**%	16%	**24**%
17	14%	**41**%	20%	**40**%
18	17%	**46**%	**27**%	**48**%

The RMSE value is calculated at every data point in the range of data and therefore if the simulation data's phase leads or lags the phase of the measured data by just 1 ms it can result in an increase in error of up to 5%. This means that the simulation data and experimental data must have phases that match exactly. Another reason for large errors is that the magnitude of the $\text{RMS}_{\text{measured}}$ values are in some cases extremely small and therefore the error signal needs to be extremely small.

Lastly, the errors are calculated over 150 seconds and the measured data is produced by 'non-perfect' sinusoidal waves generated in the wave flume whilst the simulation data is produced by 'perfect' sinusoidal waves. This inevitability leads to small variations throughout the test period and an accumulation of errors.

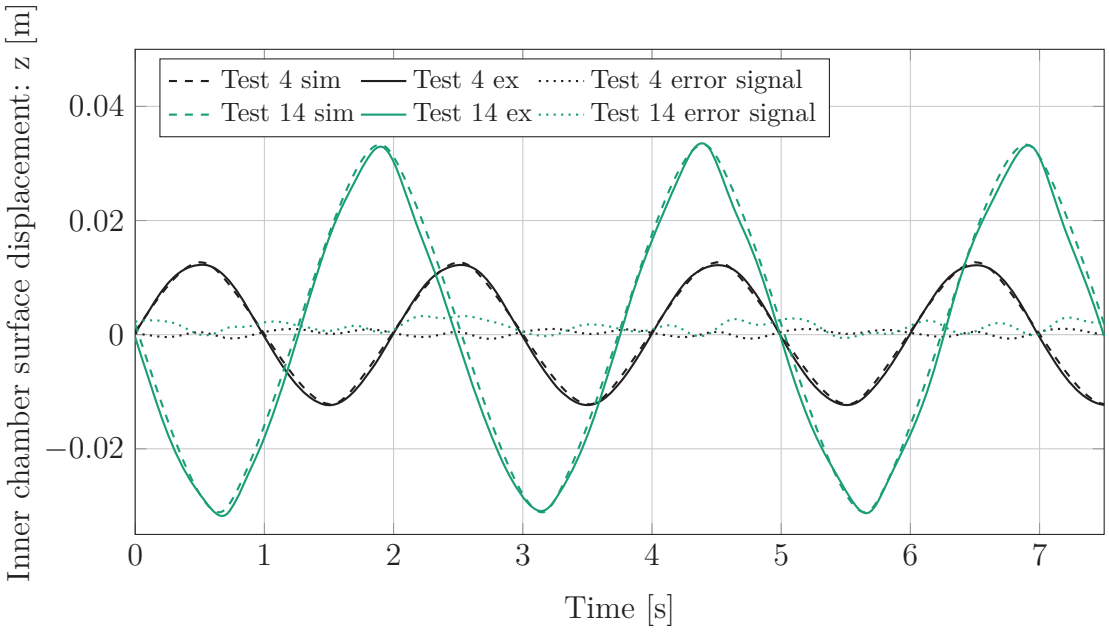

Figure 5.1: Inner chamber surface displacement. Test 4: Surface SWEC error of 6%. Test 14: Submerged SWEC error of 10%.

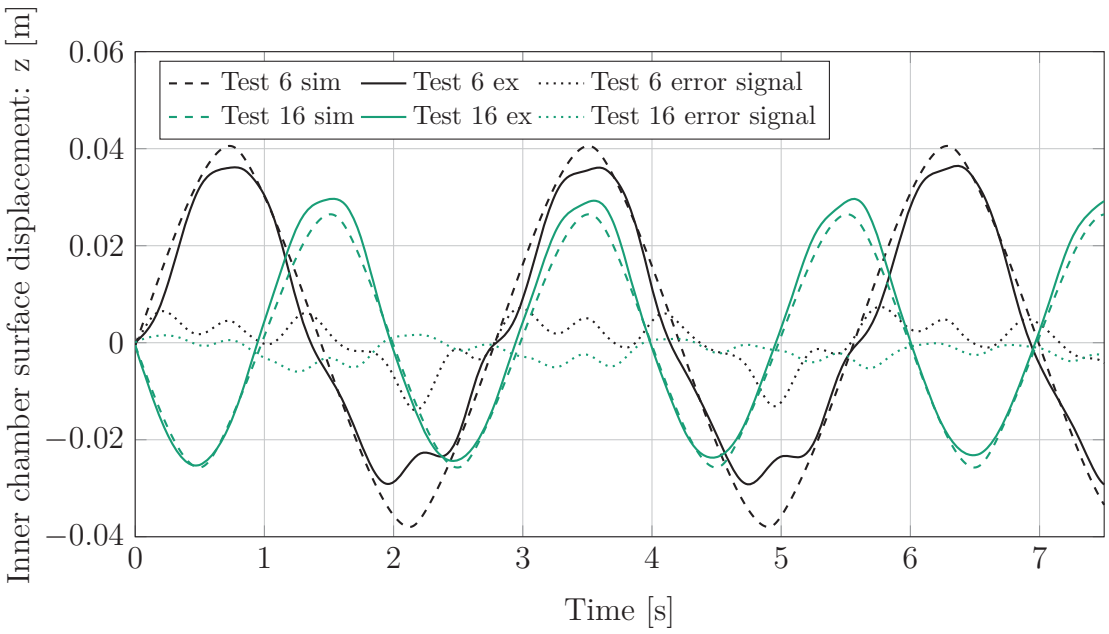

Figure 5.2: Inner chamber surface displacement. Test 6: Surface SWEC error of 20%. Test 16: Submerged SWEC error of 19%.

The time-dependent plots were investigated and are presented in order to showcase various errors and the time-dependent signals which they represent. Test scenarios which produced the lowest errors are presented first followed by test scenarios which produced the highest errors.

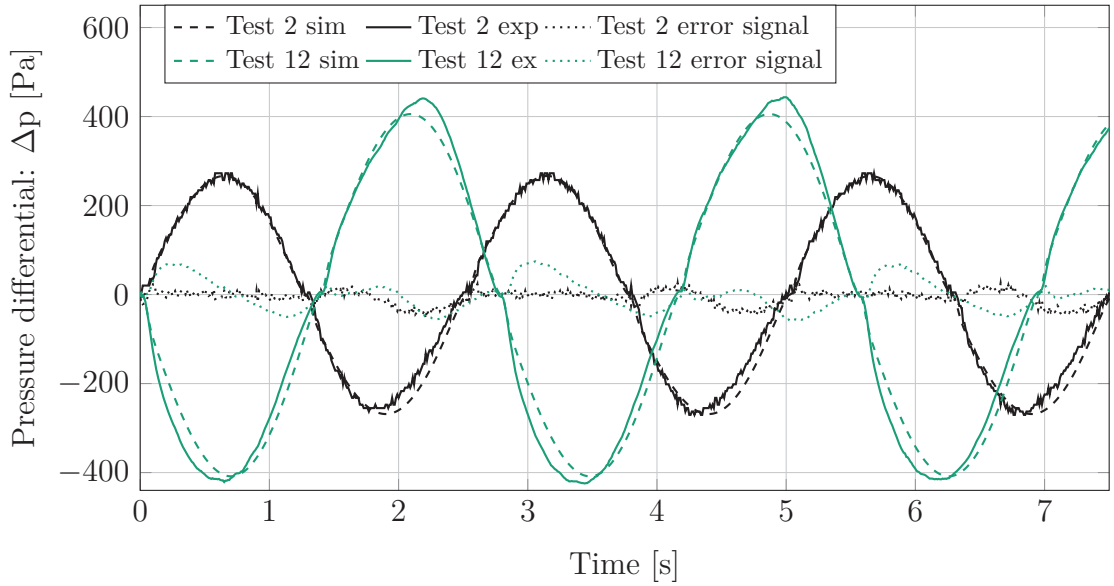

Figure 5.3: Pressure differential. Test 2: Surface SWEC error of 9%. Test 12: Submerged SWEC error of 11%.

Figure 5.1 shows the $z(t)$ predictions and experimental results which resulted in low errors. Experimental results are marked 'ex' and simulation results are marked 'sim'. Figure 5.1 shows a good fit between the simulation and experimental data. This suggests that the predicted inner chamber surface level with errors of up to 10% predict the measured results relatively accurately.

Figure 5.2 shows that with an error of 20% both the Surface and Submerged SWEC simulation models are still able to predict the measured data to a degree. There are two main aspects which contribute to the error signal produced by the simulation models. The first is how well the models predict the amplitude of the sinusoidal function and the second is how well they predict the form and period of the measured sinusoidal function.

Figure 5.2 shows that the Submerged SWEC simulation model is unable to predict the kink that is present in the measured data. Figure 5.3 shows the pressure differential predictions and experimental results which resulted in low errors. Figure 5.3 shows that the simulation results match the measured results with a relatively high level of accuracy even though the errors are near to 11%.

Notice the noise present in Figure 5.3. The impact of the noise was considered small enough to ignore and therefore the reason behind the noise was not investigated. There were very few other cases of noise found when investigating the measured results. Figure 5.4 shows the pressure differential predictions and experimental

results which resulted in high errors. Notice that the error signal has been omitted from this graph to make the graph more legible.

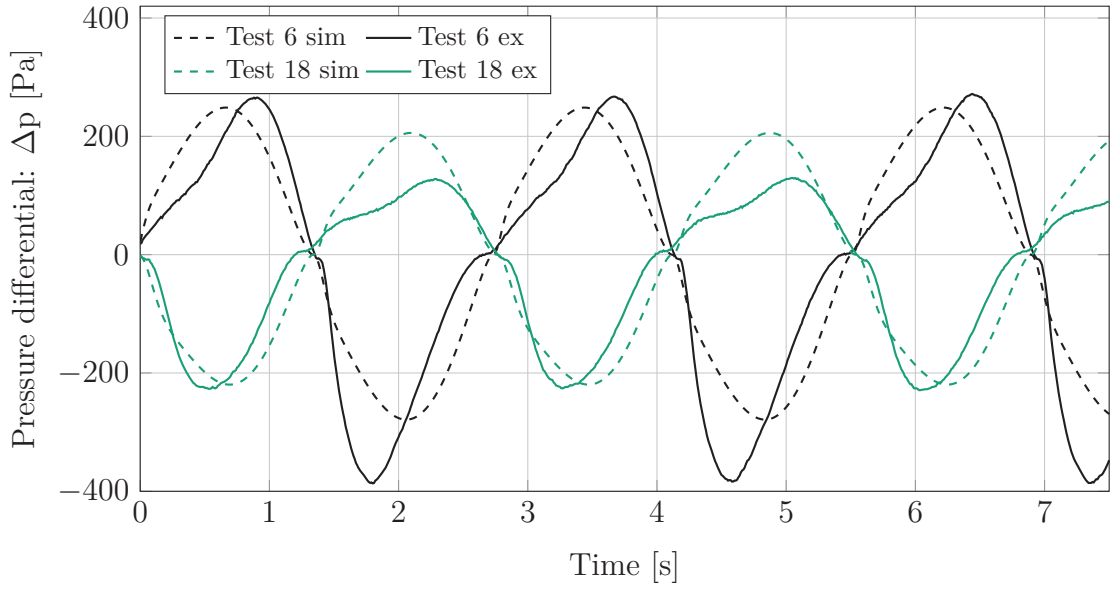

Figure 5.4: Pressure differential. Test 6: Surface SWEC error of 39%. Test 18: Submerged SWEC error of 46%.

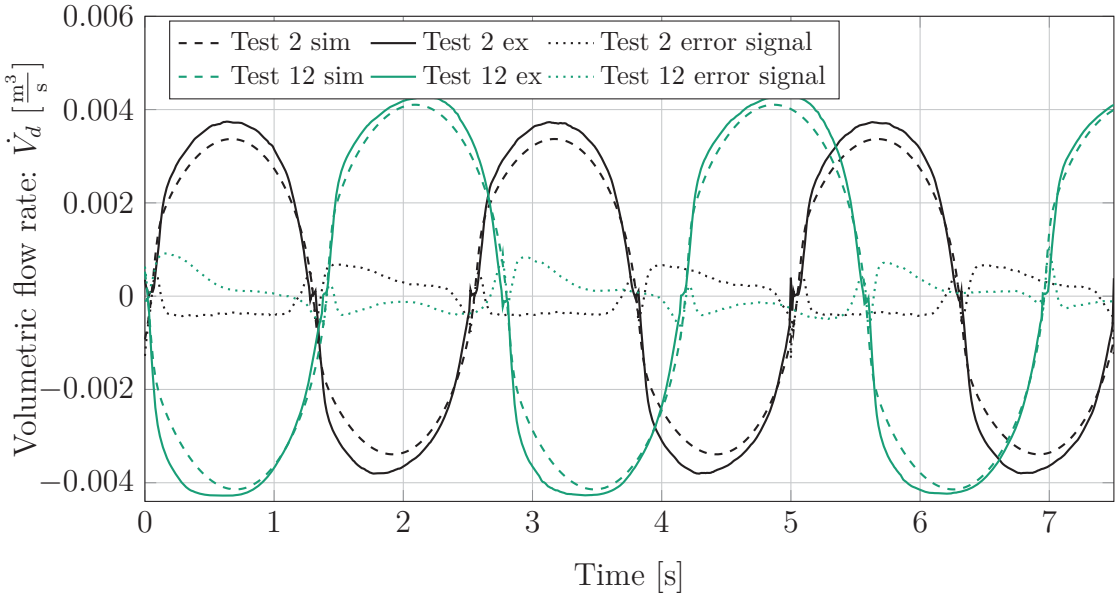

Figure 5.5: Volumetric flow rate. Test 2: Surface SWEC error of 12%. Test 12: Submerged SWEC error of 10%.

The results in Figure 5.4 show that the simulation models were unable to predict both the form and amplitude to a certain degree. The Surface SWEC model did not predict the shift in crest and trough peak whilst also underestimating the trough

amplitude. The Submerged SWEC model predicted the trough amplitude and form to a certain degree of accuracy but was unable to predict the shift in crest peak. Both sets of measured results were produced by waves with 2.75 s periods and therefore it suggests that a longer wave period distorts the form of the measured sinusoidal data.

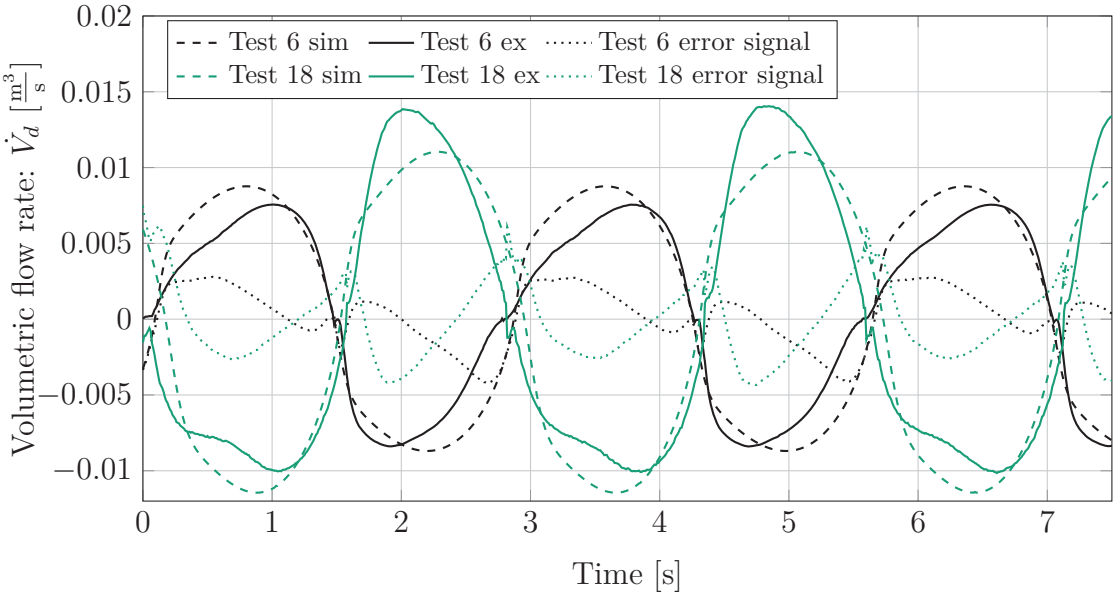

Figure 5.6: Volumetric flow rate. Test 6: Surface SWEC error of 34%. Test 18: Submerged SWEC error of 27%.

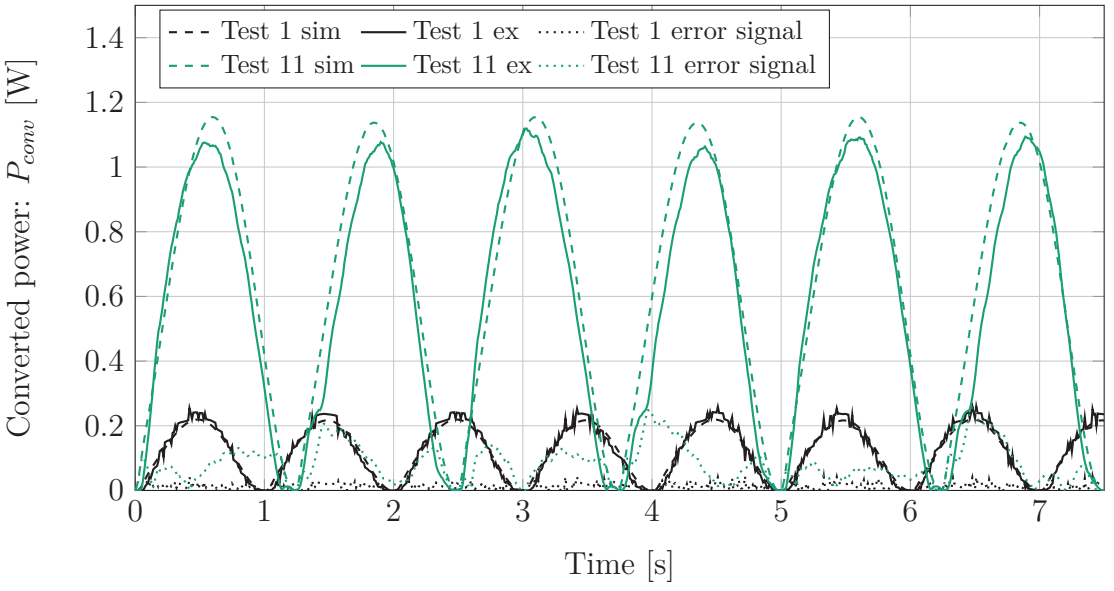

Figure 5.7: Converted power. Test 1: Surface SWEC error of 11%. Test 11: Submerged SWEC error of 11%.

Figure 5.5 shows a time-dependent plot of the volumetric flow rate through the

orifice flow meter. The results in Figure 5.5 produced errors of 12% for the Surface SWEC and 10% for the Submerged SWEC. The simulation models show the ability to predict both the amplitude and form of the measured results relatively accurately.

Volumetric flow rate results which resulted in high errors can be seen in Figure 5.6. The simulation results are deformed in the correct manner but not to the same degree as the measured results. This suggests that there is room for improvement with regard to modelling the losses in the system. See Figure 5.7 for measured and predicted values of converted power.

Figure 5.7 shows that both models are able to predict the converted wave power relatively accurately. Another aspect which Figure 5.7 shows is that the models are able to make accurate predictions for both low and high magnitudes of converted power. Figure 5.8 shows measured and predicted values of converted power which resulted in high errors, once again the error signal is omitted for the sake of legibility.

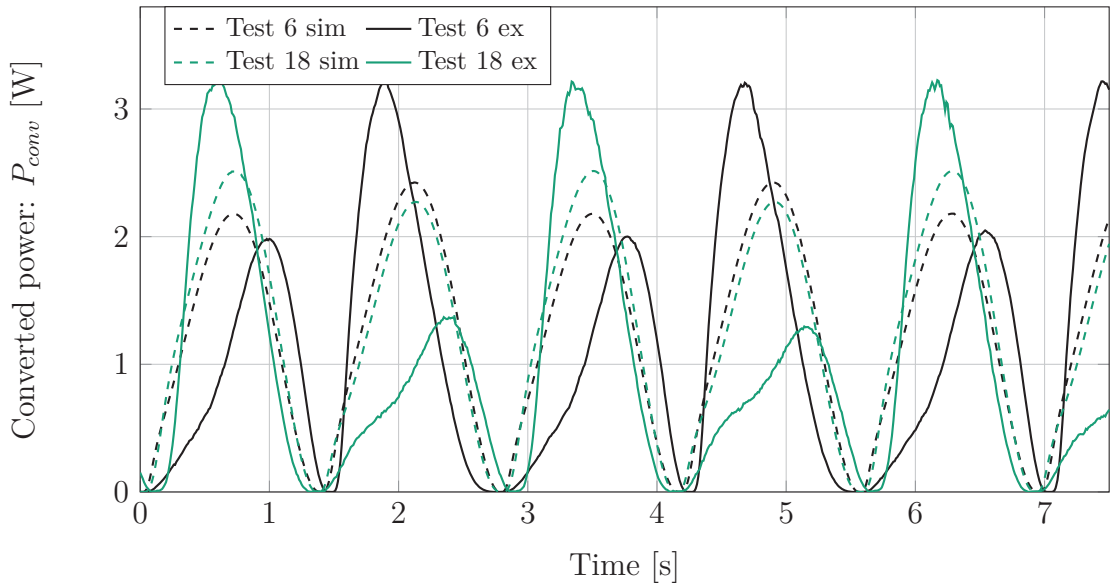

Figure 5.8: Converted power. Test 6: Surface SWEC error of 48%. Test 18: Submerged SWEC error of 48%.

Converted power is the product of volumetric flow rate and pressure differential. Higher errors as a result of combined error can therefore be expected. Figure 5.8 shows that the converted power goes through high and low power cycles. This is due to the oscillatory nature of the system where the system converts more power when the air is flowing in a certain (positive) direction. Figure 5.8 shows that although the simulation models do predict a higher power conversion when the air is flowing in the positive direction, the models are unable to accurately predict the magnitudes of the high and low power cycles.

Both the Surface and Submerged SWEC models prove to have difficulty predicting the distorted form of the time-dependent measured results at long wave periods (longer than 2.75 seconds). The deformation of the measured results at long wave periods is a result of deformed input waves which is assumed to occur due to the interaction with the SWEC chamber and flume walls.

The plots presented in this section demonstrate both the abilities and inabilities of the simulation models to predict time-dependent variables. The simulation models are validated in Section 5.3 using the predicted transmissibility and conversion efficiency results. Transmissibility and conversion efficiency are calculated by taking the average of the time-dependent variables discussed in this section.

5.2 Transmissibility and conversion efficiency

The experimental and simulation results for transmissibility and conversion efficiency for the Surface and Submerged SWEC configurations are presented in this section. Only the most important results are presented.

Each experimental test ran for 150 seconds and the last 120 seconds of each test was used to record the results. The first 30 seconds of captured data was discarded, this was done to ensure that the system had reached a steady-state. Each test required seven measurement channels, three pressure transducer measurements and four wave probe measurements. The various Matlab scripts which were written in order to process this data effectively are briefly explained and presented in Appendix C.

The Surface SWEC results presented in this section were produced at a single wave height of 0.06 m and a wave height of 0.09 m for the Submerged SWEC. The 0.06 and 0.09 m wave heights are used as they are closest to the expected operating conditions. A full set of results for all other wave heights tested is available in Appendix C.

As previously mentioned, the orifice plate sizes are referenced by the ratio of the specific plate area to the chamber's cross sectional area. Five plates were tested with 0.25%, 0.5% and 1% proving to be on average most efficient, therefore the simulation models were only run for these plates.

5.2.1 Transmissibility results

The transmissibility results are presented first. Transmissibility refers to the ratio of incoming wave amplitude to recorded chamber surface displacement amplitude $\left[\frac{a_i}{a}\right]$, where a_i is the inner chamber amplitude and a is the incident wave height. The transmissibility of the device is dependent on the chambers geometry and how effective it is at absorbing energy from the incoming wave. The transmissibility is also largely dependent on the orifice plate used. The smaller the orifice hole the 'stiffer' the system becomes and the larger the orifice hole the less 'stiff' the system becomes. Varying the orifice plate size allows the system to be 'tuned' in the efforts to find the most efficient balance between the mass flow rate and differential pressure in the system.

Surface SWEC

Figure 5.9 shows the transmissibility results for the Surface SWEC facing the waves head on for the three orifice plates at a single wave height and eight wave periods. Also note that all Surface SWEC tests were carried out in orientation 1, see Figure 5.13 for the various orientations.

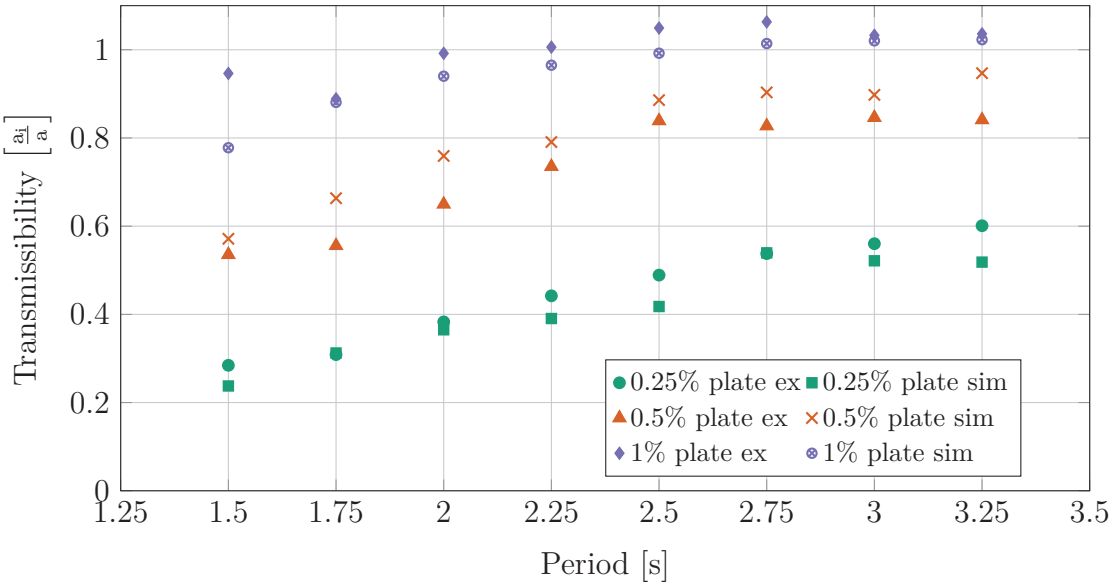

Figure 5.9: Surface SWEC transmissibility, H = 0.06 m.

The experimental data used for these graphs was recorded using the wave probe positioned in front of the chamber and the wave probe which recorded the inner chamber surface amplitude. When comparing the various plates it is clear that transmissibility is at a maximum with the 1% plate and at a minimum with the 0.25% plate. This is due to the fact that a smaller orifice hole leads to a 'stiffer' system which allows less water into the chamber.

Another trend which is present is that larger wave heights result in a decreased transmissibility. This suggests that the system translates input wave height to inner chamber wave height less efficiently when dealing with larger waves. When testing plates smaller than the 1% plate, transmissibility proved to decrease as input frequencies increased. This suggests that the response time of the inner surface level is relatively slow and does not react fast enough to match the incoming wave height at high frequencies. This being said, the conversion efficiency results show that higher frequencies do not necessarily result in lower conversion efficiencies.

The predicted transmissibility results compare relatively well with the experimental results. The transmissibility results are evaluated by referring to a transmissibility error, $t_{err}\%$ which is defined by Equation 5.4.

$$t_{err}\% = \frac{|t_{ex} - t_{sim}|}{t_{ex}} \times 100 \tag{5.4}$$

Where t_{ex} is the experimentally determined transmissibility and t_{sim} is the transmissibility produced by the simulation model. Table 5.5 shows the range of transmissibility errors produced by the simulation models for the various orifice plates.

Submerged SWEC

Figure 5.10 shows the transmissibility results for the Submerged SWEC facing the waves head on for the three orifice plates at a single wave height and eight wave periods.

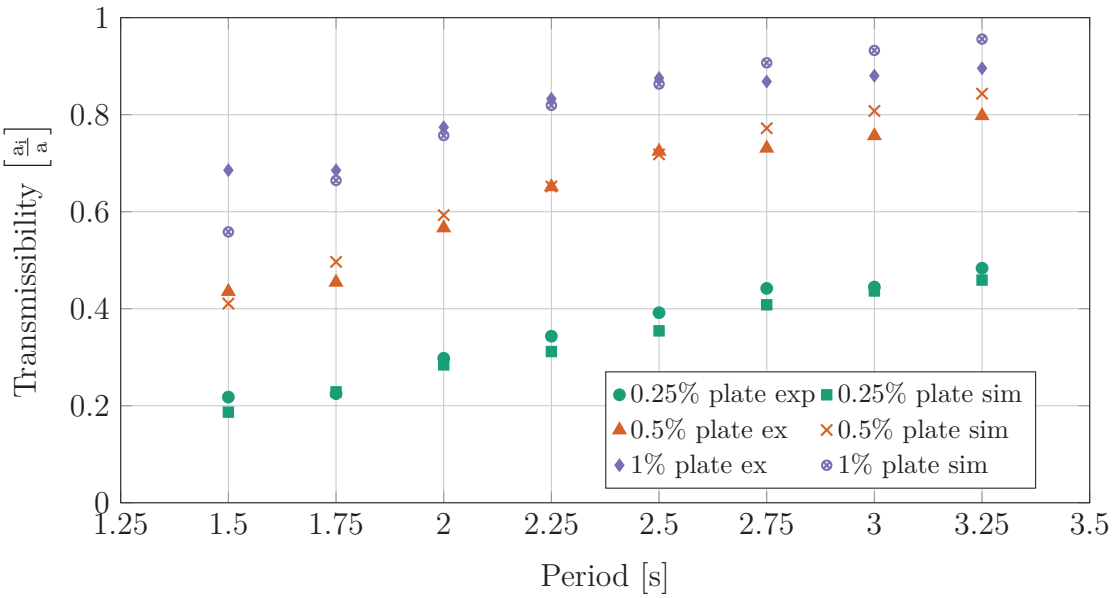

Figure 5.10: Submerged SWEC transmissibility, H = 0.09 m.

A full set of transmissibility results for the Submerged SWEC configuration is available in Appendix C along with results from a repeatability test. The repeatability tests were carried out three weeks apart and the fact that the results are comparable supports the repeatability of the test procedure. An overall average error of 3.5% occurred between the repeated test results. This average was calculated by substituting t_{sim} in Equation 5.4 with the repeated test results. This supported the test procedure as being repeatable and as well as the experimental results as being reliable.

There is an overall decrease in transmissibility for the Submerged configuration when compared to the Surface configuration transmissibility. The overall decrease in transmissibility is due to the fact that the chamber is submerged and the opening of the chamber is further away from the surface. The movement of the water particles decreases as the reference point moves downwards from the flume surface towards the floor. With the reference point on the floor of the flume, the orbital particles movement reduces strictly to a lateral particle movement in the x-plane. This phenomenon is seen in Figure 2.5 for shallow water waves. There is less energy available to the chamber for absorption due to there being less energy in the water

Table 5.5: Transmissibility errors for the Surface and Submerged SWEC configurations.

Orifice plate	Configuration	Range of errors
0.25%	Surface SWEC	0% to 16%
0.5%	Surface SWEC	0% to 26%
1%	Surface SWEC	0% to 17%
0.25%	Submerged SWEC	0% to 14%
0.5%	Submerged SWEC	0% to 16%
1%	Submerged SWEC	0% to 20%

particles, and therefore the transmissibility decreases. Table 5.5 shows the range of errors produced by the simulation models for the various orifice plates.

5.2.2 Conversion efficiency results

Conversion efficiency refers to the ratio of converted power measured over the orifice plate defined by Equation 3.2, to incoming wave power defined by Equation 2.11, $\left[\frac{P_{conv}}{P_w}\right] \times 100\%$. The conversion efficiency is one of, if not the most important aspect that was analysed. It describes the ability of the SWEC to convert wave energy into pneumatic energy.

Surface SWEC

The measured and predicted conversion efficiencies for the Surface SWEC configuration are presented first, see Figure 5.11. The results in Figure 5.11 provide insight into the power conversion capability of the SWEC as well as the optimal and worst-case wave conditions for power conversion.

Thiruvenkatasamy and Neelamani (1997) show the maximum conversion efficiency of an OWC WEC to be around 65% whilst using a 0.81% orifice plate with three chambers connected in an array. Joubert (2013) found that a 0.71% orifice plate proved to be most efficient when experimentally testing a similar type of device. These results are supported by the results found in Figure 5.11 as the 0.5% and 1% plates prove to be the most efficient. The results produced by these sources support the theory that a 0.75% orifice plate along with more than one chamber in an array would greatly increase the efficiency of the device.

The predicted conversion efficiencies are evaluated by calculating a conversion efficiency error, $ce_{err}\%$, see Equation 5.5.

$$ce_{err}\% = \frac{|ce_{ex} - ce_{sim}|}{ce_{ex}} \times 100\% \tag{5.5}$$

Where ce_{ex} is the experimentally determined conversion efficiency and ce_{sim} is the conversion efficiency predicted by the simulation model.

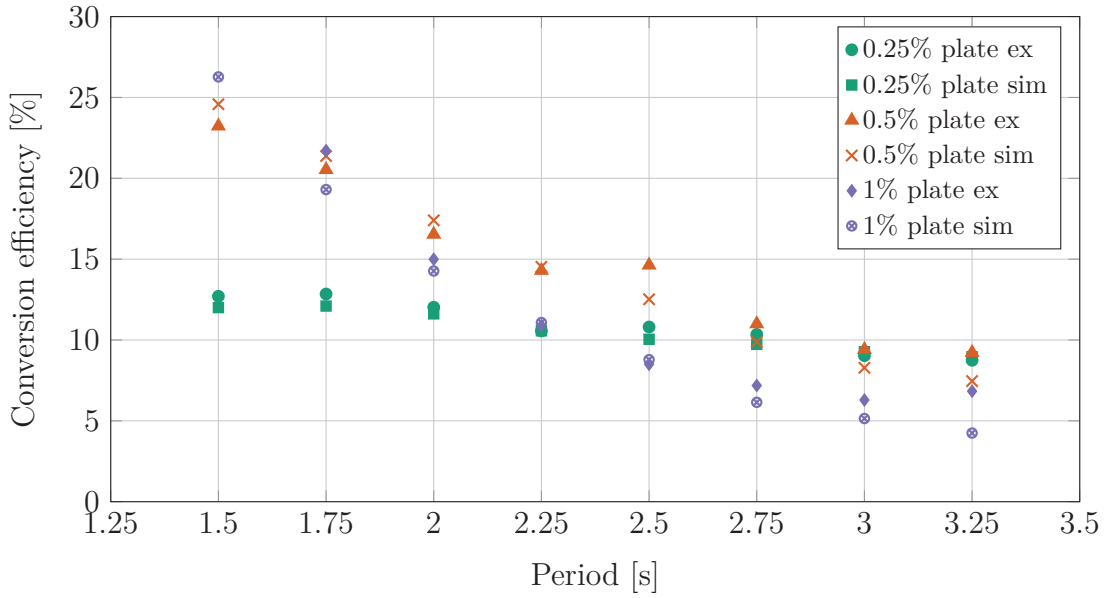

Figure 5.11: Surface SWEC conversion efficiency, H = 0.06 m.

Submerged SWEC

As previously mentioned the Submerged SWEC is the main focus of this study and was therefore put through additional testing. The additional testing includes testing the chamber in four additional orientations; the conversion efficiency for the various orientations was investigated and is presented in this section. See Figure 5.12 for the conversion efficiency of the Submerged SWEC in orientation 1. The repeatability tests showed an average error of 10% when substituting ce_{sim} with the repeated test results, this error was deemed low enough to define the results as reliable.

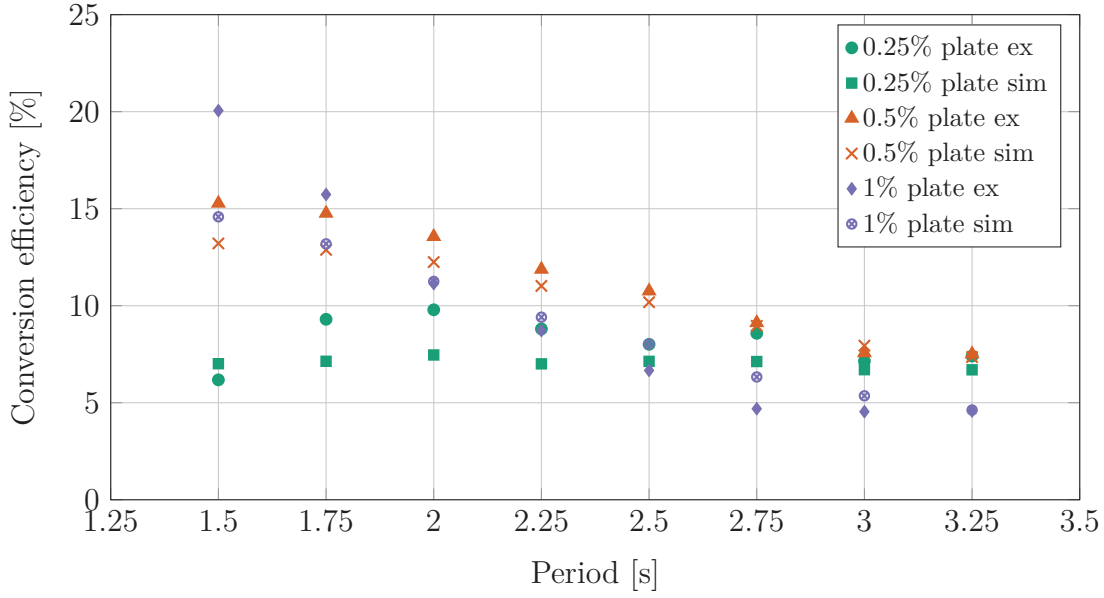

Figure 5.12: Submerged SWEC conversion efficiency, H = 0.09 m.

Similar trends are visible between the results for the two configurations with an overall decrease in conversion efficiency for the Submerged configuration. This is due to the depth of the Submerged SWEC. As previously mentioned the water particle velocity decreases as the reference point moves towards the floor of the flume. This results in less power being available for the chamber to absorb. Due to the fact that the absorbed power is compared to the power in the wave at the surface, the conversion efficiency drops. This phenomenon is described in Figure 2.5.

Table 5.6: Conversion efficiency errors for the Surface and Submerged SWEC configurations.

Orifice plate	Configuration	Range of errors
0.25%	Surface SWEC	0% to 42%
0.5%	Surface SWEC	1% to 19%
1%	Surface SWEC	0% to 37%
0.25%	Submerged SWEC	0% to 25%
0.5%	Submerged SWEC	0% to 13%
1%	Submerged SWEC	1% to 43%

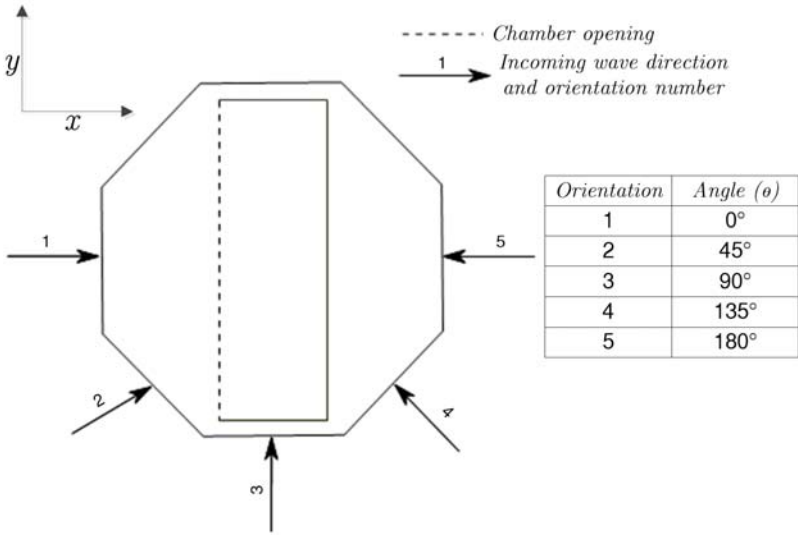

Figure 5.13: Various experimentally tested orientations.

Retief *et al.* (1982) state that the Submerged SWEC was designed to absorb no more than 30% of the incoming wave energy. The 30% absorption target was set with the intention of not affecting the natural form of the waves to a great extent. Thiruvenkatasamy and Neelamani (1997: 63) refer to Whittaker and Stewart (1993) and state that "the maximum power output [of an OWC WEC in an array] can increase by a factor of two when compared to a device in isolation".

Joubert (2013) also shows that an array of chambers greatly increases the conversion efficiency of a similar device compared to an isolated chamber. If these statements

prove true for the SWEC and the efficiencies increased by a factor of two, the conversion efficiencies in Figure 5.12 would reach the 30% mark. See Table 5.6 for the range of conversion efficiency errors produced by the simulation models for the various orifice plates.

The original SWEC device was designed by Retief *et al.* (1982) to face the incoming waves at an angle of 45°. The device was therefore tested in 4 additional orientations in order to evaluate its response to various incoming wave angles. Figure 5.13 presents a graphical representation of the orientations and their respective angle relative to the oncoming waves.

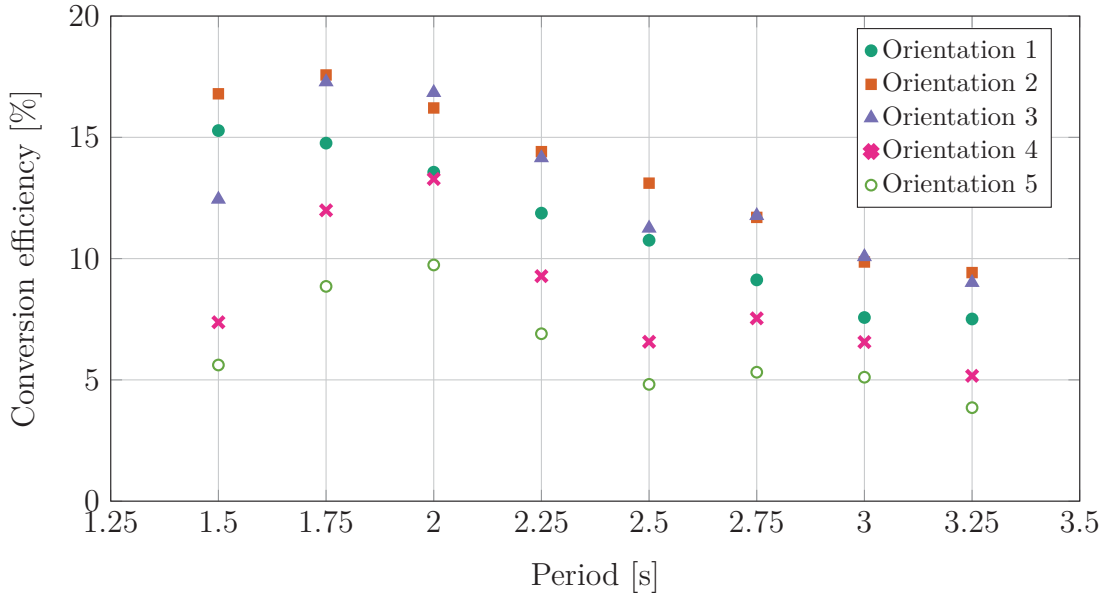

Figure 5.14: Submerged SWEC 0.5% plate experimental conversion efficiency in various orientations, H = 0.09 m.

The 0.5% plate was used in the additional testing due to it having the best average conversion efficiency in orientation 1. This resulted in the 0.5% plate being tested with three wave heights, eight wave periods in four extra orientations. The results for the 0.09 m wave height for all five orientations is shown in Figure 5.14. A full set of results for orientations 2,3,4 and 5 is available in Appendix C.

The conversion efficiency results show that orientation 2 converts power most efficiently. It must be noted that the magnitude of the converted power is similar to the magnitude of converted power in orientation 1 but due to the device being at an angle a shorter wave front comes into contact with the device. This leads to less available wave power P_{wave} and therefore an increased ratio of converted power to available wave power.

See Table 5.7 for the conversion magnitudes and efficiencies for the tests graphed in Figure 5.14. The maximum values are highlighted, notice that the maximum conversion magnitude and efficiency is never found in the same orientation.

The results show orientations 2 and 3 as being the most efficient with the overall highest conversion efficiency at a wave period of 1.5 s, wave height of 0.065 m in

Table 5.7: Conversion magnitude and efficiency, H=0.09 m.

			Submerged SWEC									
			Conversion magnitude [W]					Conversion efficiency [%]				
		Orientation / T [s]	1	2	3	4	5	1	2	3	4	5
Orifice plate	0.5%	1.5	0.84	0.63	0.39	0.53	0.34	15	17	12	7	6
		1.75	1.12	0.89	0.66	0.91	0.70	15	18	17	13	9
		2	1.04	0.78	0.56	0.88	0.65	14	16	17	12	10
		2.25	1.20	0.98	0.71	0.89	0.69	12	14	14	10	7
		2.5	1.06	0.89	0.57	0.72	0.45	11	13	11	5	5
		2.75	0.98	0.84	0.74	0.86	0.51	9	12	12	6	5
		3	0.94	0.75	0.53	0.77	0.55	8	10	10	6	5
		3.25	0.87	0.74	0.51	0.77	0.41	8	9	9	4	4

orientation 2, with a value of 22.4%. The proposed operating conditions are waves with a period of 12.3 seconds and a height of 2 m, which corresponds to a scaled period of 2.46 seconds and a height of 0.08 m. The maximum conversion efficiency for these conditions occurs in orientation 2 with an efficiency of 13.1%.

The simulation model was derived with the aim of predicting the converted power and transmissibility in orientation 1 and does not accommodate the SWEC in other orientations. Adapting the simulation model to allow for a variable chamber orientation is one of the recommendations for further research. Section 5.3 presents a discussion of the most influential and important results.

5.3 Discussion and model validation

This section starts by discussing the viability of the SWEC device as a WEC and concludes with a discussion on the accuracy of the developed simulation models.

5.3.1 The SWEC as a viable WEC

As previously discussed, the three main aspects that define the viability of a WEC device include the survivability, capital cost and conversion efficiency of the device. Although investigating the survivability and capital cost of the technology is a crucial step in the development and implementation of the SWEC, it was outside the scope of this project. Therefore any conclusion on the SWEC as a viable WEC is based solely on its ability to convert wave energy into pneumatic energy.

The experimentally determined conversion efficiencies for the single Surface SWEC chamber range from 10% at long wave periods to 26% at short wave periods. The Surface SWEC achieved a conversion efficiency of 15% at the expected operating conditions. This relates to a full scale average power output of 50 kW per chamber. A Surface SWEC unit made up of 24 chambers would thus have an average power output of 1.2 MW at expected operating conditions.

As previously mentioned Whittaker and Stewart (1993) state that an OWC WEC device such as the SWEC can potentially increase its maximum power output by a factor of two when comparing an array of chambers to a chamber in isolation. The conversion efficiency is also expected to increase by using an orifice plate with an area ratio between 0.5% and 1% as previous studies have shown. This supports the 30% conversion efficiency target defined by Retief *et al.* (1982) and a potential average power output of 2.4 MW per device.

Another valuable aspect to investigate is the Surface SWEC's converted power to area ratio. This value is often used to evaluate solar power technologies and the same can be done for the SWEC. The Surface SWEC achieved a converted power to area ratio of 695 W/m^2 (scaled up). This is comparable to the solar constant (1.3 kW/m^2) which expresses the maximum solar radiation entering the atmosphere.

An important aspect to be noted about the Surface SWEC is that it can act as a breakwater as well as a WEC. This is because the device protrudes out of the surface of the ocean and when multiple chambers are connected it forms a wall-like structure. Using the Surface SWEC as a hybrid WEC-breakwater would make it more cost effective as the budget for the breakwater would be merged with the WEC budget. The major difficulty that a project like this faces is the fact that breakwaters are usually built to guard harbours which are purposely built in sheltered areas with low wave energy resource. For this reason, a hybrid project like the one proposed may only work in special breakwater cases where the location of the breakwater is fixed in a position with substantial wave energy.

The experimentally determined conversion efficiencies for the single Submerged SWEC chamber range from 5% at long wave periods to 22% at short wave periods. The Submerged SWEC achieved a conversion efficiency of 13% at the expected operating conditions in orientation 2, this supports the orientation proposed by Retief *et al.* (1982). The 13% conversion efficiency relates to a full scale average power output of 70 kW per chamber operating in most prominent wave conditions of South Africa's west cost. A full scale Submerged SWEC unit made up of 24 cham-bers would thus have an average power output of 1.68 MW at expected operating conditions.

Note that the Submerged SWEC operating conditions include larger wave heights compared to the Surface SWEC conditions. This is due to the Surface SWEC being designed for deployment near to the shore whilst the Submerged SWEC was designed for off-shore deployment. Again the study by Whittaker and Stewart (1993) and the use of a more efficient PTO mechanism for the full scale model suggests the efficiency could be significantly increased. These values support the 30% conversion efficiency target defined by Retief *et al.* (1982) and could lead to an average power output of 3.36 MW per device.

The Submerged SWEC device proved to have overall lower conversion efficiencies compared to the Surface SWEC, this is due to two reasons. Firstly the Submerged SWEC was exposed to larger input wave conditions; the experimental results have shown that the SWEC converts power more efficiently with smaller waves. The second reason is that the Submerged SWEC lies beneath the ocean surface. At this

level, the wave particle energy is lower than the wave particle energy at the surface.

The Submerged SWEC achieved a converted power to area ratio of 970 W/m^2 (scaled up). This is again competitive with the solar constant value of 1.3 kW/m^2. It is assumed that once the SWEC has been put through a certain amount of optimisation, the converted power to area ratio would definitely surpass the power to area ratio of incoming solar. This sheds light on one of the main advantages of wave energy which is that it has a very high energy density.

Although the Submerged SWEC does not have the capability of being deployed in a hybrid breakwater configuration, it does have a unique feature in the fact that it is positioned on the sea floor. As mentioned, survivability is one of the most important aspects for WECs. Located on the sea floor, the Submerged SWEC is able to be deployed in areas with high wave energy resource with a greater chance of survival. This is due to the device being unexposed to destructive breaking waves.

5.3.2 Simulation model validation

The aim of the time-domain simulation models developed for this study was to predict the internal surface elevation, volumetric flow rate, differential pressure, converted power, transmissibility and conversion efficiency of the SWEC. The model uses linear wave theory and assumes that the expansion and compression of the air is an isentropic process and allows for air compressibility. The effects of turbulence, diffraction, viscosity and vortex shedding at the wall tips are not modelled directly. Instead, a damping coefficient of 10% of the critical damping value is used, much like Gervelas *et al.* (2011).

The four time-dependent output variables which were investigated included the chamber water level $z(t)$, pressure differential $\Delta p(t)$, volumetric flow rate through the orifice flow meter $\dot{V}_d(t)$ and the converted pneumatic power $P_{conv}(t)$. Transmissibility and power conversion are calculated using these time-dependent variables and are defined as the most important outputs of the models. For this reason, the simulation models are validated by inspecting their ability to predict transmissibility and conversion efficiency. Errors of up to 10% are deemed acceptable.

Surface SWEC model

The transmissibility and conversion efficiency errors for the simulations can be seen in Table 5.8. The error results are colour coded in order to simplify the validation process. Table 5.8 shows that the Surface SWEC model struggled to accurately predict the transmissibility of the device for the 0.25% and 1% orifice plates in high frequency input waves (T=1.5 s).

The 0.5% plate lead to a maximum transmissibility error at a wave height of 0.09 m and period of 3.25 s. A general increase in transmissibility error with increase in wave height is also present. The model demonstrated the ability to accurately predict the

transmissibility of the device for the 0.25% plate and 1% plate for most of the input wave conditions.

Conversion efficiency is the most important output produced by the simulation model and the results carry similar trends to the transmissibility errors. The model struggles to accurately predict the conversion efficiency for all three plates for long wave periods and large wave heights (T=3.25 s and H=0.09 m). In general the model was able to predict the conversion efficiency to a good degree of accuracy as seen in Table 5.8.

Submerged SWEC

The transmissibility and conversion efficiency errors for the Submerged SWEC are presented in the right half of Table 5.8. Similar trends are visible between the Surface and Submerged SWEC errors. The Submerged SWEC transmissibility errors prove to be very low with the model only struggling at high frequency wave inputs for the 1% and 0.25% plates. The Submerged SWEC model proves to accurately model the transmissibility of the device as most of the errors are lower than 5%.

The conversion efficiency errors produced by the Submerged SWEC model are generally a lot higher compared to the Surface SWEC model. The biggest difference is the high errors produced for all wave heights at low wave periods for the 0.25% plate. The 0.5% plate simulations produced accurate results while the 1% plate simulations struggled in similar areas to the Surface SWEC model. This suggests that the losses associated with the auxiliary volume were not modelled with great accuracy and that larger wave inputs generally lead to larger errors.

Table 5.8: Transmissibility and conversion efficiency error table.

			Surface SWEC						Submerged SWEC					
			Transmissibility error%			Conversion efficiency error%			Transmissibility error%			Conversion efficiency error%		
		H [m] / T [s]	0.03	0.06	0.09	0.03	0.06	0.09	0.065	0.09	0.11	0.065	0.09	0.11
Orifice plate	0.25%	1.5	15	16	15	9	5	3	13	14	14	25	13	22
		1.75	0	1	0	9	5	3	2	1	0	23	23	20
		2	4	4	5	1	3	0	3	4	4	22	23	21
		2.25	9	11	8	3	0	4	7	9	9	19	20	18
		2.5	13	14	16	7	7	3	8	9	10	20	10	17
		2.75	10	0	4	6	5	7	3	7	6	11	16	12
		3	7	6	1	0	2	21	1	1	2	9	6	3
		3.25	13	13	5	5	2	42	1	5	5	6	9	0
	0.5%	1.5	0	6	8	4	5	10	5	5	4	4	13	6
		1.75	1	19	25	2	4	8	16	9	10	13	12	9
		2	3	16	19	7	5	11	9	4	6	9	9	2
		2.25	1	7	11	9	1	13	8	0	0	5	7	6
		2.5	3	5	3	18	14	7	6	0	1	4	5	4
		2.75	2	9	18	2	10	7	12	5	4	6	1	1
		3	4	6	20	6	11	13	10	6	7	8	4	8
		3.25	3	12	26	3	19	13	11	5	6	2	2	0
	1%	1.5	17	17	17	28	22	20	17	18	20	22	27	27
		1.75	1	0	0	7	11	10	0	3	4	7	16	20
		2	4	5	5	5	4	6	0	2	3	7	1	3
		2.25	3	4	5	0	1	3	1	1	4	18	7	1
		2.5	1	5	8	19	3	7	2	1	3	31	20	11
		2.75	5	4	14	3	14	2	6	4	0	43	34	22
		3	0	1	2	6	18	10	7	5	0	36	17	6
		3.25	2	1	1	11	37	34	7	6	2	18	1	10

Key
0-5%
6-10%
11-15%
16-20%
>20%

Chapter 6

Conclusions and recommendations

This chapter presents the most significant conclusions drawn from the results of this study. It starts with conclusions on the conversion efficiency of the SWEC. The chapter goes on to present conclusions made on the evaluation and validation of the simulation models and concludes with an overview of the project objectives.

6.1 Conversion efficiency of the SWEC

Both the Surface and Submerged SWEC proved to successfully convert incident wave energy to pneumatic energy. The ability of the device to convert wave energy into pneumatic energy proved to be highly dependent on the incoming wave characteristics as well as the PTO mechanism. Conclusions made on the conversion efficiency of the device are stated below:

- The Surface SWEC proved to have a conversion efficiency of 15% when tested in the expected operating wave conditions, (T=2.5 s, H=0.06 m).
- The Surface SWEC achieved a peak conversion efficiency of 26% using the 0.5% orifice plate at a wave height of 0.03 m and wave period of 1.5 seconds.
- The Submerged SWEC proved to have a conversion efficiency of 13% when tested in the expected operating wave conditions in orientation 2, (T=2.5 s, H=0.09 m).
- The Submerged SWEC achieved a peak conversion efficiency of 22% using the 0.5% orifice plate at a wave height of 0.065 m and wave period of 1.5 seconds in orientation 2.
- Orientations 2 and 3 proved to be most efficient, suggesting that the Submerged SWEC operates more efficiently when the incident wave angle is between 45° and 90° with respect to the chamber.

Recommendations

The following recommendations are made:

- The Surface and Submerged SWEC configurations should be tested in a coupled configuration with multiple chambers.
- Multiple additional orifice plates should be tested, the area of the orifice holes should range between 0.5% and 1% of the chambers free water surface area.

6.2 Simulation model evaluation and validation

The simulation models developed for this project were evaluated and validated on their ability to predict the transmissibility and conversion efficiency for the Surface and Submerged SWEC devices. The accuracy of the transmissibility predictions demonstrates the abilities of the hydrodynamic part of the models; whilst the accuracy of the conversion efficiency predictions demonstrates the abilities of the thermodynamic aspect. The following conclusions are made:

- The Surface SWEC model accurately predicted the transmissibility for most input wave conditions with the exception of the 0.5% plate at a wave height of 0.09 m. The transmissibility errors ranged from 0% to 26% with the majority of the errors being less than 10%. This supports the conclusion that the model can accurately predict the transmissibility of the Surface SWEC.
- The Surface SWEC model accurately predicted the conversion efficiency for most input wave conditions with the exception of the 1% plate at very long, and very short wave periods (T=1.5 s and T=3.25 s). The conversion efficiency errors ranged from 0% to 42% with the majority of the errors being less than 10%. This supports the conclusion that the model can accurately predict the conversion efficiency of the Surface SWEC.
- The Submerged SWEC model demonstrated great accuracy when predicting the transmissibility for almost all wave input conditions with the exception of the 0.25% and 0.1% plates with short wave periods (T=1.5 s). The transmissibility errors ranged from 0% to 20% with the majority of the errors being less than 5%. This supports the conclusion that the model can accurately predict the transmissibility of the Submerged SWEC.
- The Submerged SWEC model predicted the conversion efficiency with a moderate degree of accuracy for most input wave conditions. Both the 0.25% and 1% orifice plate simulations struggled with very short wave periods (T=1.5 s). The conversion efficiency errors ranged from 0% to 43% with the majority of the errors being less than 15%. This supports the conclusion that the model provides valuable insight on the ability of the Submerged SWEC but still has room for improvement.

In general the simulation models are able to accurately predict the transmissibility and conversion efficiency in the SWEC system. The predictions become less accurate

when the input waves have either very short or very long periods (T<1.5 s and T>3 s), as well as large wave heights (H>0.11 m). The major discrepancies between the experimental and predicted results are due to the following aspects:

- Inaccurate modelling of the turbulent losses.
- Inaccurate representation of the input wave characteristics.
- Assuming that the system is both adiabatic and reversible.

Recommendations

The following recommendations are made:

- The simulation models could be used to optimise the SWEC chamber.
- The simulation models could be adapted to allow for various chamber orientations.
- The hydrodynamic and thermodynamic models should be run separately whilst using measured time-dependent data as input. For example, the hydrodynamic model should use the measured wave height in front of the chamber as an input whilst the thermodynamic model should use the recorded inner chamber height as an input.
- The simulation models could be adapted to allow for irregular wave input conditions.

6.3 Project objectives

The five main objectives for this project are restated:

- Experimental testing of the Surface SWEC configuration using relevant wave conditions.
- Experimental testing of the Submerged SWEC configuration in various orientations using relevant wave conditions.
- Simulation modelling of both configurations.
- Verification and evaluation of both models.
- Experimentally supported conclusions made on energy conversion efficiency, operating orientation and optimal test conditions.

All five objects were accomplished with the evaluation and validation of the simulation models supporting the ability of the models to describe the SWEC to a good degree of accuracy. The simulation models also provide a better understanding of the SWEC system. Light is shed on the various losses which occur in the system as well as how the wave energy is converted into pneumatic energy. However, the models also show that there is still room for improvement.

References

Ackerman, P. H. 2009. *Air turbine design study for a wave energy conversion system.* MSc thesis, Department of Civil Engineering Stellenbosch University.

Airy, G. B. 1845. Tides and waves. *Encyclopedia Metropolitana.* London, Scientific, 5: 241–396.

Amirault, S. B. 2015. *Fluid Mechanics: Head Loss*. [Online]. Available: http://-goo.gl/tuwzon. [2015, March 20].

Brennen, C. E. 1982. *A review of added mass and fluid inertia forces* (tech. rep. No. N62583-81-MR-554). Naval Engineering Laboratory Port Hueneme California.

CEM. 2006. *Coastal engineering manual*. US Army Corps, Part 2 Chapter 1: Water wave mechanics.

Cengel, Y. A. & Cimbala, J. M. 2006. *Fluid mechanics*. New York: McGraw Hill.

Chanson, H. 1999. *The hydraulics of open channel flow: an introduction*. Oxford: Elsevier Butterworth-Heinemann.

Cruz, J. 2008. *Ocean wave energy current status and furture perspectives*. New York: Springer.

Dizadji, N. & Sajadian, S. E. 2010. Modeling and optimization of the chamber of owc system. *Energy*, 36: 2360–2366.

Dong, R. G. 1978. *Effective mass and damping of submerged stuctures* (tech. rep. No. UCRL-52342). University of California.

Drew, B., Plummer, A. R. & Sahinkaya, M. N. 2009. *A review of wave energy converter technology.* MSc thesis, Department of Mechanical Engineering University of Bath.

Evans, D. V. 1976. A device for wave-power absorption by oscillating bodies. *Journal of Fluid Mechanics*, 77: 1–25.

Evans, D. V. 1982. Wave-power absorption by system of oscillating surface pressure distribution. *Journal of Fluid Mechanics*, 114: 481–499.

Fairhurst, J. 2013. *Testing and evaluation of a submerged SWEC chamber* (tech. rep. No. NA). Department of Mechanical and Mechatronic Engineering Stellenbosch University.

Falnes, J. 2005. *Presentation on wave energy for Norges University* (tech. rep. No. NA). Norges University. Trondheim.

Folley, M., Whittaker, T. & Osterried, M. 2004. *The oscillating wave surge converter* (tech. rep. No. 2004-JSC-377). School of Civil Engineering, Queen's Univeristy Belfast.

Friis-Madsen, E. 2005. *Wave Dragon*. [Online]. Available: http://goo.gl/7bams1. [2015, 13 April].

Garrison, T. 1996. *Oceanography: an invitation to marine science*. Boston: Wadsworth Publishing Company.

Gervelas, R., Trarieux, F. & Patel, M. 2011. A time-domain simulator for an oscillating water column in irregular waves at model scale. *Ocean Engineering*, 38: 1007–1013.

Heath, T. 2012. A review of oscillating water columns. *Philosophical Transactions of the Royal Society*, 370: 235–245.

Helmholtz, M. & Hermann, L. 1895. *Sensations of tone as a physiological basis for the theory of music*. London: Longmans, Green and Co.

Holthuijsen, L. H. 2007. *Waves in oceanic and coastal waters*. Cambridge: Cambridge University Press.

Holtz, M. W. 2007. *Modelling and design of a novel air-spring for a suspension seat* MSc thesis, Department of Mechanical Engineering Stellenbosch University.

HR Wallingford Ltd. 2009. *Wave generation system for a flume*. Oxford: HR Wallingford Ltd.

ISO. 2003. *Measurement of fluid flow by means of pressure differential devices inserted in circular-cross section conduits running full* (tech. rep. No. 5167-2). SAI Global. Sydney.

Jenkinson, R. W. 2014. *Pipe expansions and contractions* (tech. rep. No. NA). Department of Mechanical Engineering University of Waterloo.

Joubert, J. R. 2008. *An investigation of the wave energy resource on the South African coast, focusing on the spatial distribution of the South West coast.* MSc thesis, Department of Civil Engineering Stellenbosch University.

Joubert, J. R. 2013. *Design and development of a novel wave energy converter.* PhD dissertation, Department of Mechanical and Mechatronic Engineering Stellenbosch University.

Kim, M. H. & Koo, W. 2011. Nonlinear time-domain simulation of a land based oscillating water column. *Journal of waterway, port and coastal engineering*, 136: 276–285.

Kooverji, B. 2011. *Pneumatic power measurement of an oscillating water converter model.* MSc thesis, Department of Mechanical and Mechatronic Engineering Stellenbosch University.

McCormick, M. E. 1981. *Ocean wave energy conversion.* Hoboken: Wiley - Interscience.

Meyer, I. 2012. *Modelling the air and water flow in an oscillating water column device* (tech. rep. No. NA). Department of Mechanical and Mechatronic Engineering Stellenbosch University.

Miles, J. W. 1957. On the generation of waves by shear flows. *Journal of Fluid Mechanics*, 7: 469–478.

Patel, M. 1978. Hydrostatic analysis of marine vehicles with trapped air cavities. *International Shipbuilding Progress*, 34: 64–74.

Patel, M. & Harrison, J. 1985. The mechanics of a compliant motion suppression-system for semisubmersiblesmodel scale. *Sound and Vibration*, 106: 491–507.

Pelamis Wave Power Ltd. 1998. *Pelamis wave power.* [Online]. Available: http://www.pelamiswave.com. [2014, October 9].

Phillips, O. M. 1957. On the generation of waves by turbulent winds. *Journal of Fluid Mechanics*, 2: 417–445.

Potter, M. & Wiggert, D. 2002. *Mechanics of fluids.* Wadsworth: Brooks Cole.

Retief, G. F., Prestige, G. K., Muller, F. P. J., Guestyn, L. C. & Swart, D. H. 1982. Detailed design of a wave energy conversion plant. *ICCE*, 1: 2546–2562.

Revill, S. P. 1978. *A simple analytical model for a fixed oscillating water column device* (tech. rep. No. PR8). National Engineering Laboratory. Glasgow.

Rodrigues, L. 2006. *Wave power conversion system for electrical energy production* (tech. rep. No. NA). Department of Electrical Engineering Faculty of Science and Technology Nova University of Lisbon.

SAPA. 2012. *Peak power demand to hit highest level.* [Online]. Available: http://-goo.gl/z5cndw. [2014, September 20].

Sarmento, A. J. N. A. & Falcao, A. F. 1985. Wave generation by an oscillating surface-pressure and its application in wave-energy extraction. *Journal of Fluid Mechanics*, 150: 467–485.

Sea Grant. 2004. *Conversion of wave characteristics to actual electric energy/-power potentials* (tech. rep. No. NA). Oregan State University.

Szumko, S. 1982. Mechanical model for oscillating water column with compressibility. *Journal of Engineering Mechanics*, 115: 1851–1866.

Tedd, J. 2007. *Testing, analysis and control of wave dragon, wave energy converter.* PhD dissertation, Department of Civil Engineering Aalborg University.

Thiruvenkatasamy, K. & Neelamani, S. 1997. On the efficiency of wave energy caissons in array. *Applied Ocean Research*, 19: 61–72.

Westhuysen, A. 2002. *The application of the numerical wind wave model swan to a selected field case on the South African coast.* PhD dissertation, Department of Mechanical Engineering Stellenbosch University.

Whittaker, T., Beattie, W., Folley, M., Boake, C., Wright, A., Osterried, M. & Heath, T. 2004. *The limpet wave power project - the first years of operation* (tech. rep. No. NA). Faculty of Engineering, Queen's University Belfast.

Whittaker, T. & Folley, M. 2011. Nearshore oscillating wave surge converters and the development of oyster. *Philosophical transactions of the royal society*, 370: 345–364.

Whittaker, T. & Stewart, T. 1993. An experimental study of nearshore and shoreline oscillating water columns with harbours. *European Wave Energy Symposium*, 1: 283–294.

Yang, S. J. 2013. *Sjyang wave generation - own work*. [Online]. Available: http://-goo.gl/ghrchy. [2014, November 12].

Yemm, R., Pizer, D., Retzler, C. & Henderson, R. 2011. Pelamis: experience from concept to connection. *Philosophical Transactions of the Royal Society*, 370: 365–380.

Zevenbergen, L., Lagasse, P. & Edge, B. 2004. *Tidal hydrology, hydraulics and scour at bridges*. Washington: U.S. Department of Transportation.

Zhang, Y., Zou, Q. & Greaves, D. 2012. Air water two-phase flow modelling of hydrodynamic performance of an oscillating water column device. *Renewable Energy*, 41: 159–170.

Appendix A

Experimental set-up

A.1 Existing experimental set-up

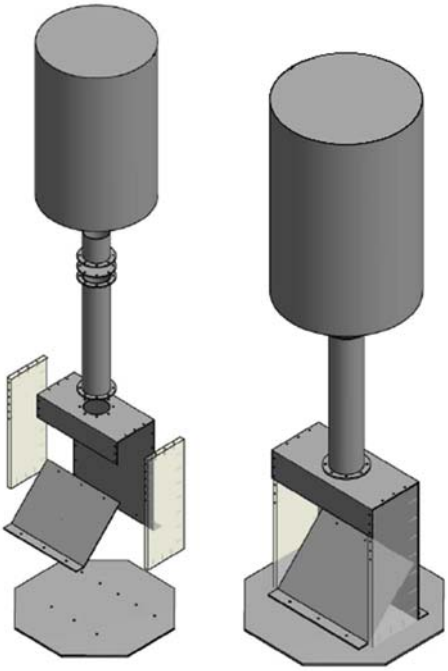

Figure A.1: Existing scale model (Fairhurst, 2013).

A.2 SWEC dimensions and operating conditions

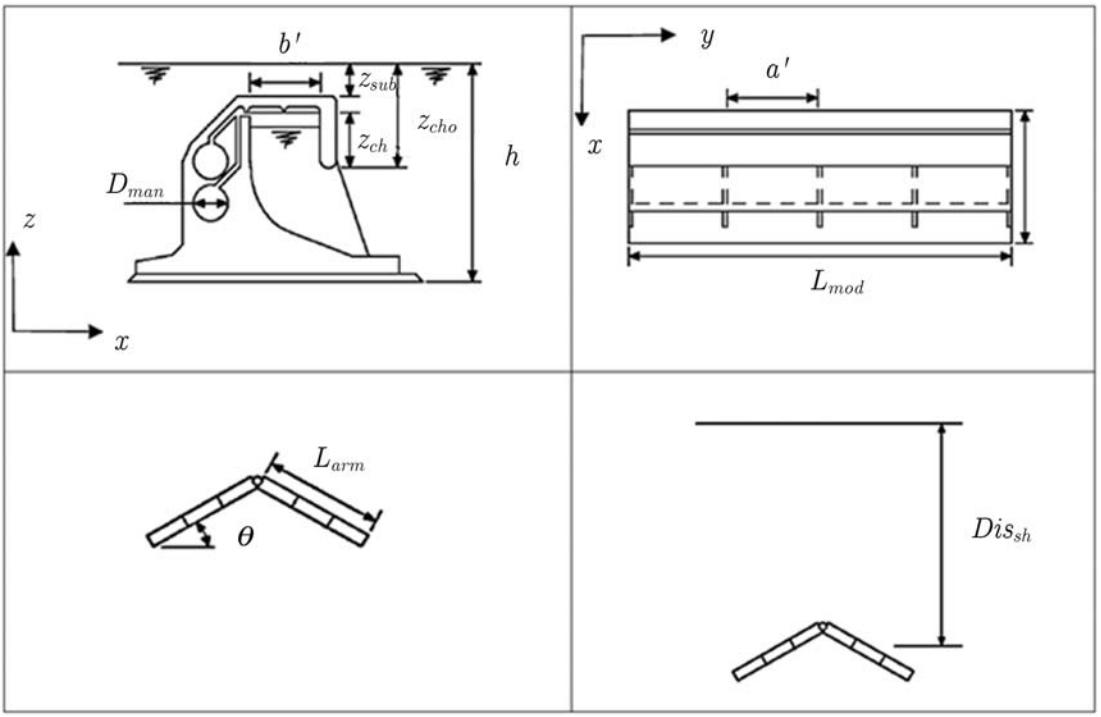

Figure A.2: Dimensions of the SWEC adapted from Ackerman (2009).

Table A.1: SWEC dimension set (Ackerman, 2009).

Dimension	Value
D_{man}	3 m
b'	6 m
Z_{sub}	2 m
Z_{cho}	5.5 m
Z_{ch}	3 m
h	15-20 m
a'	12 m
L_{mod}	53.33 m
N_{ch}	4
θ	45 °
L_{arm}	160 m
N_{mod}	3
Dis_{ah}	1.5 km

Table A.2: Range of SWEC operating conditions (Ackerman, 2009).

Parameter	Value
Significant wave height (m)	0.5, 1, **2**, 3, 4, 5
Water depth (m)	15, 16, **17.5**, 18, 19, 20
Chamber submergence (m)	2, 3, 4, 5, **5.5**, 6, 7
Wave approach angle (°)	225, 230, 235, **240**, 245, 250, 255
Wave periods (s)	10, 11, **12.3**, 13, 14
Wavelength(m)	115.6, 130.1, 144.4, **148.6**, 158.5, 172.4

Table A.3: Froude scaling (Chanson, 1999).

Aspect	Symbol	Formula	Value
Dimensions	L_r	N/A	25
Wave period	t_r	$\sqrt{L_r}$	5
Pressure	p_r	L_r	25
Power	P_r	$L_r^{3.5}$	78125

Table A.4: Scaled SWEC dimension set.

Dimension	Value
D_{man}	0.12 m
b'	0.24 m
Z_{sub}	0.08 m
Z_{cho}	0.22 m
Z_{ch}	0.12 m
h	0.6-0.8 m
a'	0.48 m
L_{mod}	2.133 m
N_{ch}	4
θ	45 °
L_{arm}	6.4 m
N_{mod}	3
Dis_{ah}	0.06 km

Table A.5: Scaled operating conditions.

Parameter	Value
Significant wave height (m)	0.08
Water depth (m)	0.6-0.8
Wave periods (s)	2.46
Wavelength(m)	5.94

A.3 HBM differential pressure transducers

Figure A.3: HBM differential pressure transducers.

A.4 Helmholtz resonance frequency

Helmholtz resonance frequency : f_H
Speed of sound through air : $c_s = 340.29\,\frac{\text{m}}{\text{s}}$
Area of orifice flow meter duct : $A_d = \pi 0.0625^2 \text{m}^2$:
Chamber volume : $V_c = 6.912 \times 10^{-3} \text{m}^3$
Auxiliary volume : $V_{aux} = 5\,\text{m}^3$
Equivalent length : $L_{eq} = L_d + 0.6D_h = 1.331\,\text{m}$

Calculation for chamber volume:

$$f_H = \frac{c_s}{2\pi}\sqrt{\frac{A_d}{V_c L_{eq}}} = \frac{340.29}{2\pi}\sqrt{\frac{\pi 0.0625^2}{6.912 \times 10^{-3} \times 1.331}} = 65.5\,\text{Hz} \tag{A.1}$$

Calculation for auxiliary volume:

$$f_H = \frac{c_s}{2\pi}\sqrt{\frac{A_d}{V_{aux} L_{eq}}} = \frac{340.29}{2\pi}\sqrt{\frac{\pi 0.0625^2}{5 \times 1.331}} = 2.33\,\text{Hz} \tag{A.2}$$

A.5 Auxiliary volume calculation

Maximum theoretical decrease in volume: $V = 0.12 \times 0.24 \times 0.48 = 0.014\,\text{m}^3$
Water height: $h = 0.75\,\text{m}$
Submergence: $d_1 = h - 0.553 = 0.197\,\text{m}$

Heat capacity ratio: $\gamma = 1.4$
Density of water: $\rho_w = 1000\,\frac{\text{kg}}{3}$
Heat capacity ratio: $\gamma = 1.4$
Duct volume : $V_{duct} = \pi \times \frac{0.125}{2}^2 \times 1.256\text{m}^3$
Auxiliary volume : $V_{aux} = 0.166\,\text{m}^3$
Static pressure before volume decrease : $p_1 = \rho \times g \times d_1 = 1.928\,\text{kPa}$
Volume before volume decrease : $V_1 = V + V_{duct} + V_{aux} = 0.195\,\text{m}^3$
Volume after volume decrease : $V_2 = V_1 - V = 0.181\,\text{m}^3$
Static pressure after volume decrease : $p_2 = p_1(\frac{V_1}{V_2})^\gamma\text{kPa}$
Pressure increase percentage : $p_{increase} = \frac{p_2 - p_1}{p_1} \times 100 = 11\%$

A.6 Orifice flow meter exploded view and calibration curves

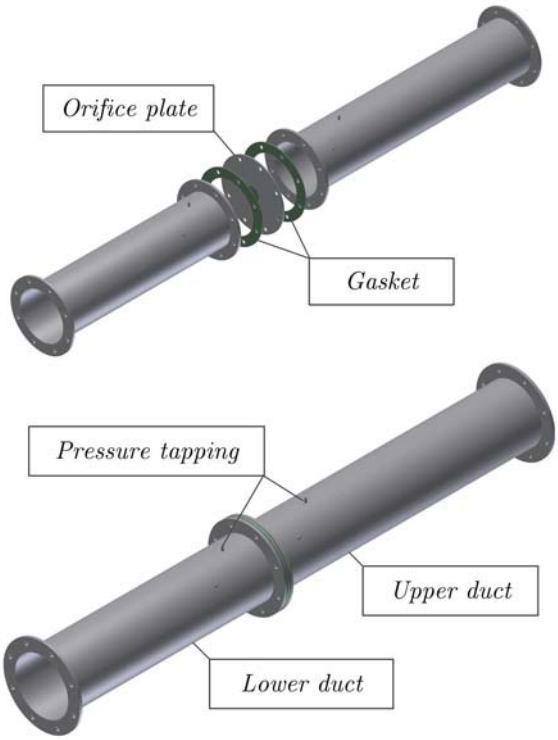

Figure A.4: Top: Exploded view of orifice flow meter. Bottom: Orifice flow meter assembly.

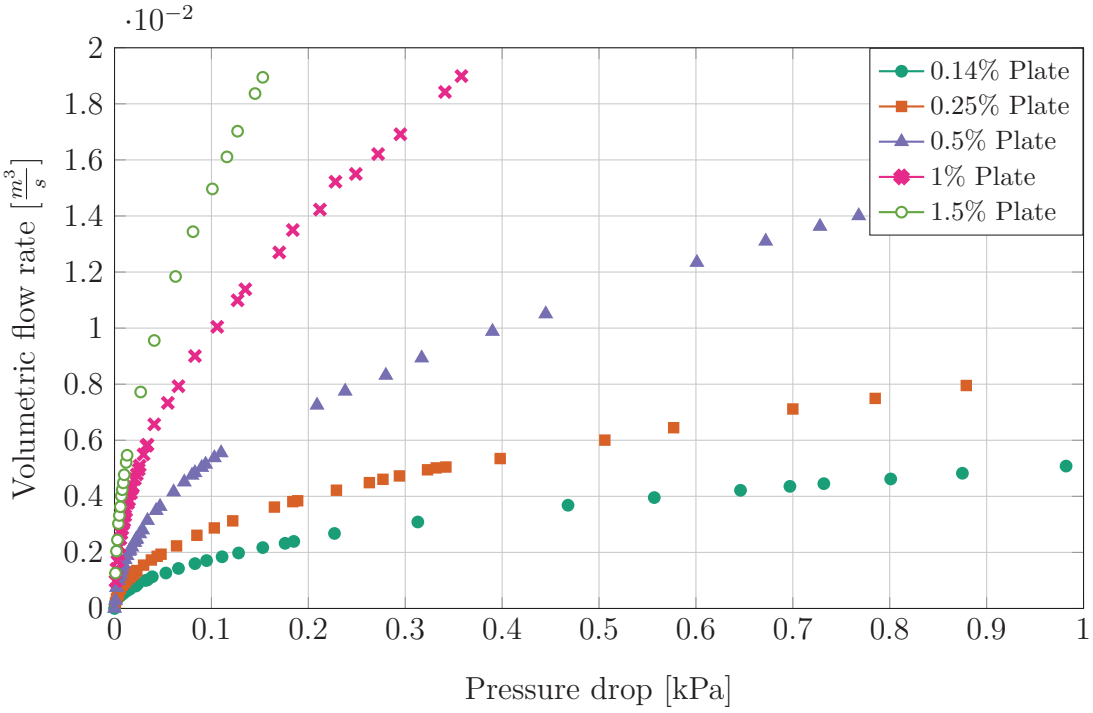

Figure A.5: Orifice plate calibration curves.

A.7 Flow meter calibration, DAQ unit and instrument schematic layout.

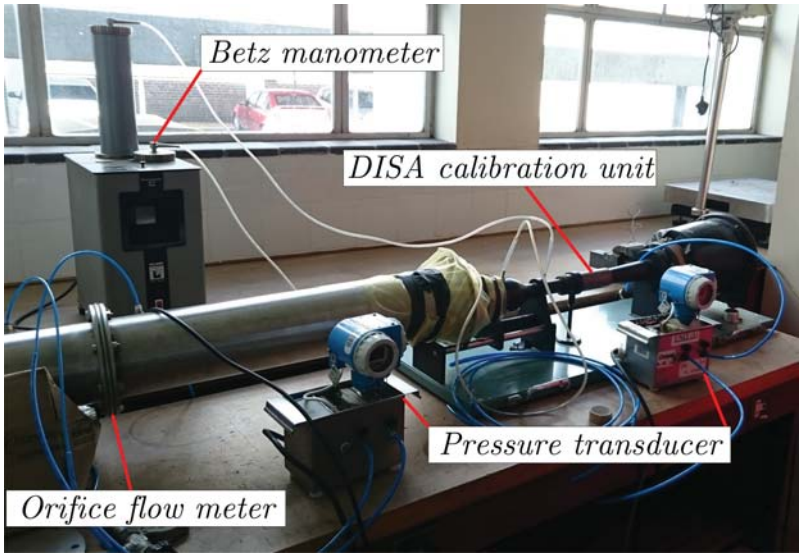

Figure A.6: Orifice flow meter calibration.

Figure A.7: HR Wallingford data acquisition unit.

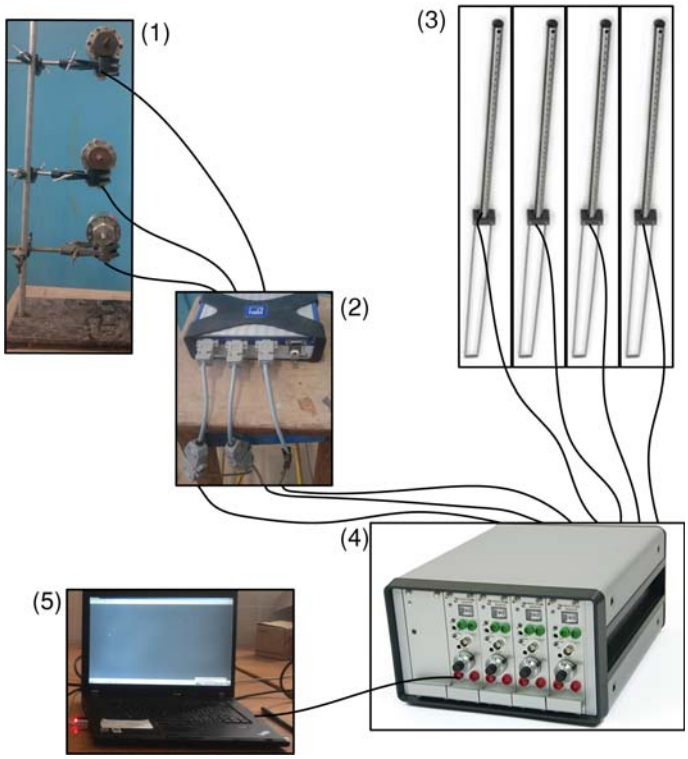

Figure A.8: Instrument schematic layout.

A.8 Measured and predicted wavelengths

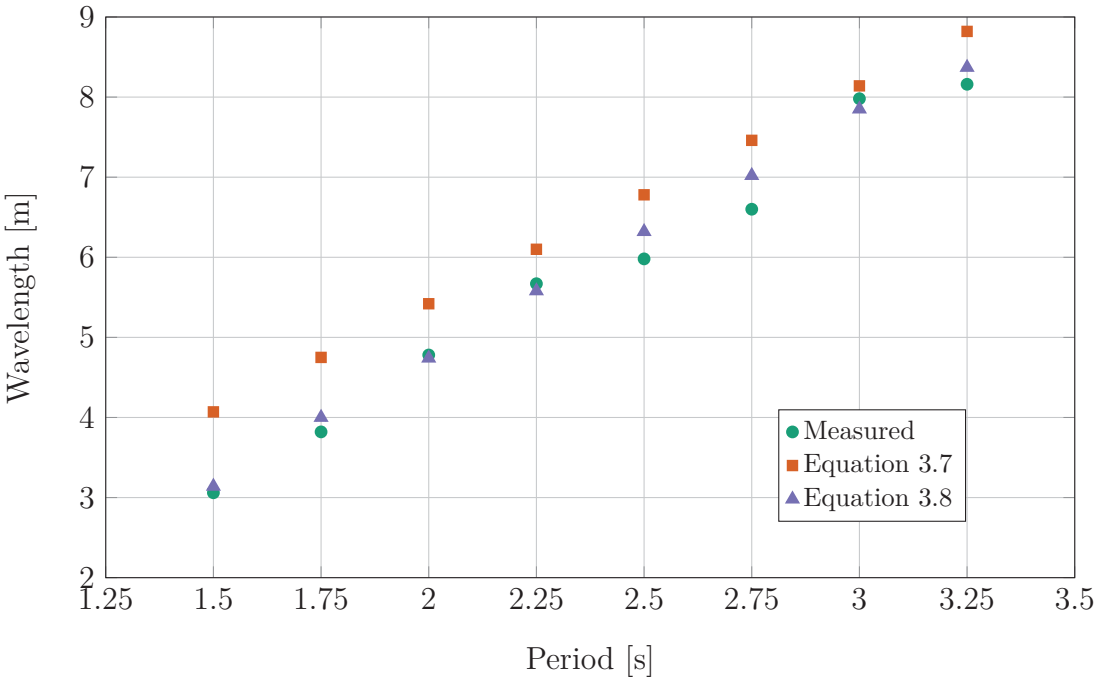

Figure A.9: Measured and predicted wavelengths.

Appendix B

Simulink model diagrams

Newtons second law model

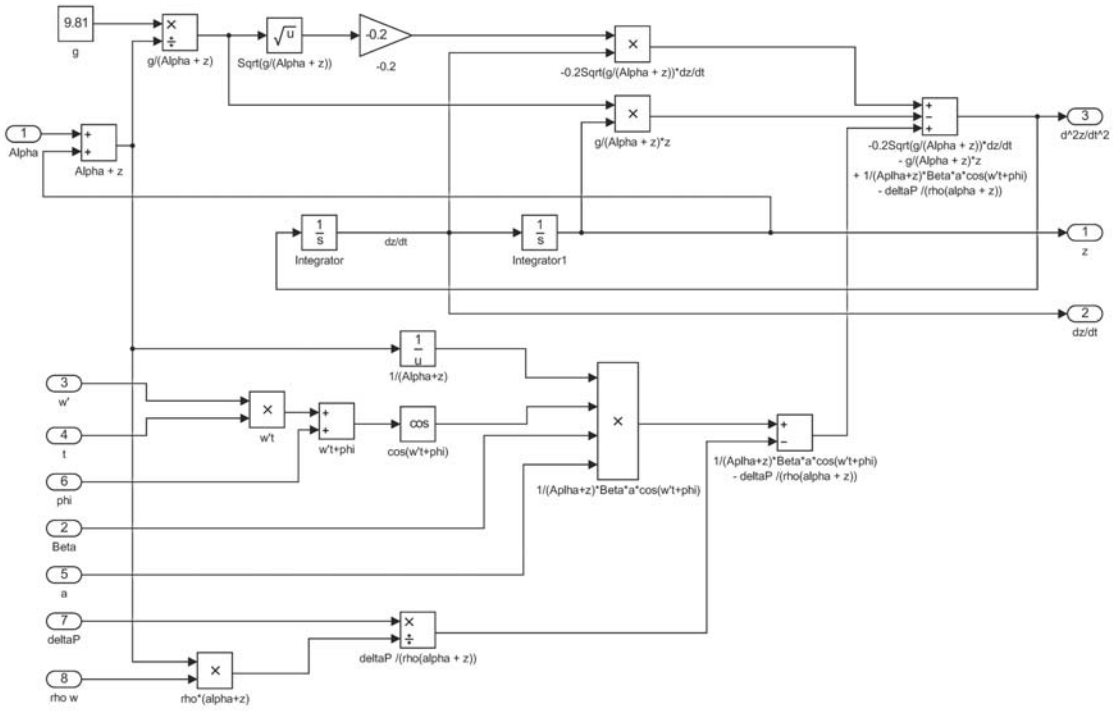

Figure B.1: Newtons second law model diagram.

Added mass model

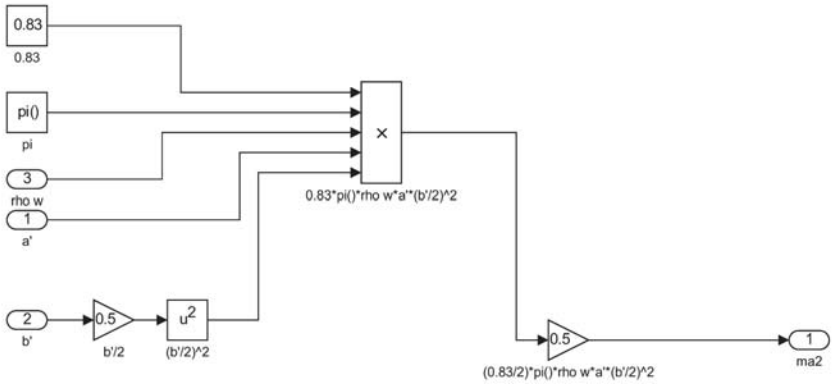

Figure B.2: Added mass model diagram.

Aplha and Beta model

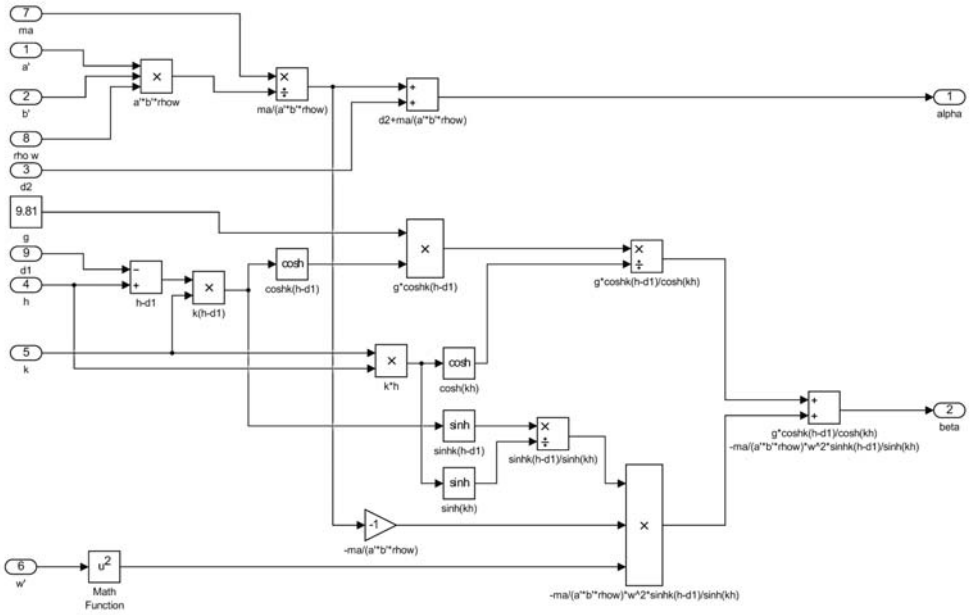

Figure B.3: Alpha and Beta model diagram.

Ideal gas law

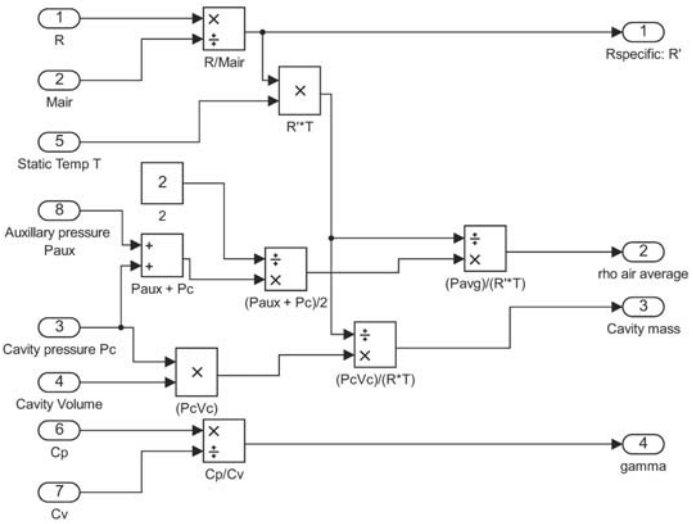

Figure B.4: Ideal gas law model.

Auxiliary chamber model

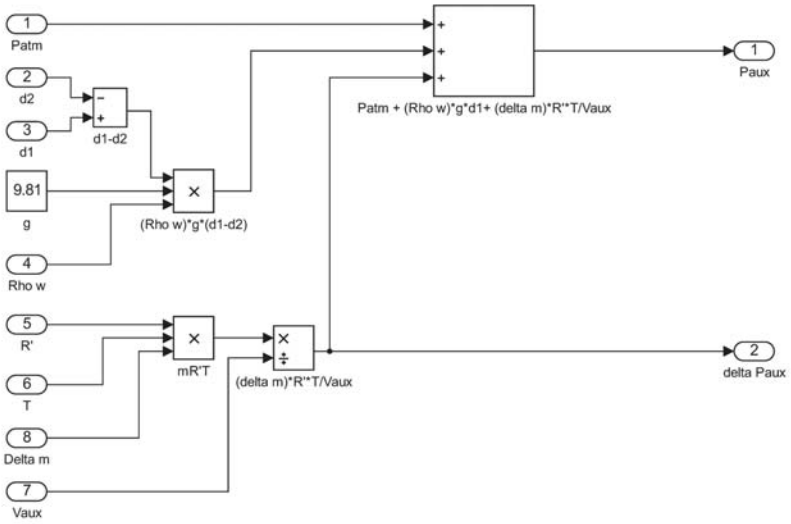

Figure B.5: Auxiliary chamber model.

Differential pressure model

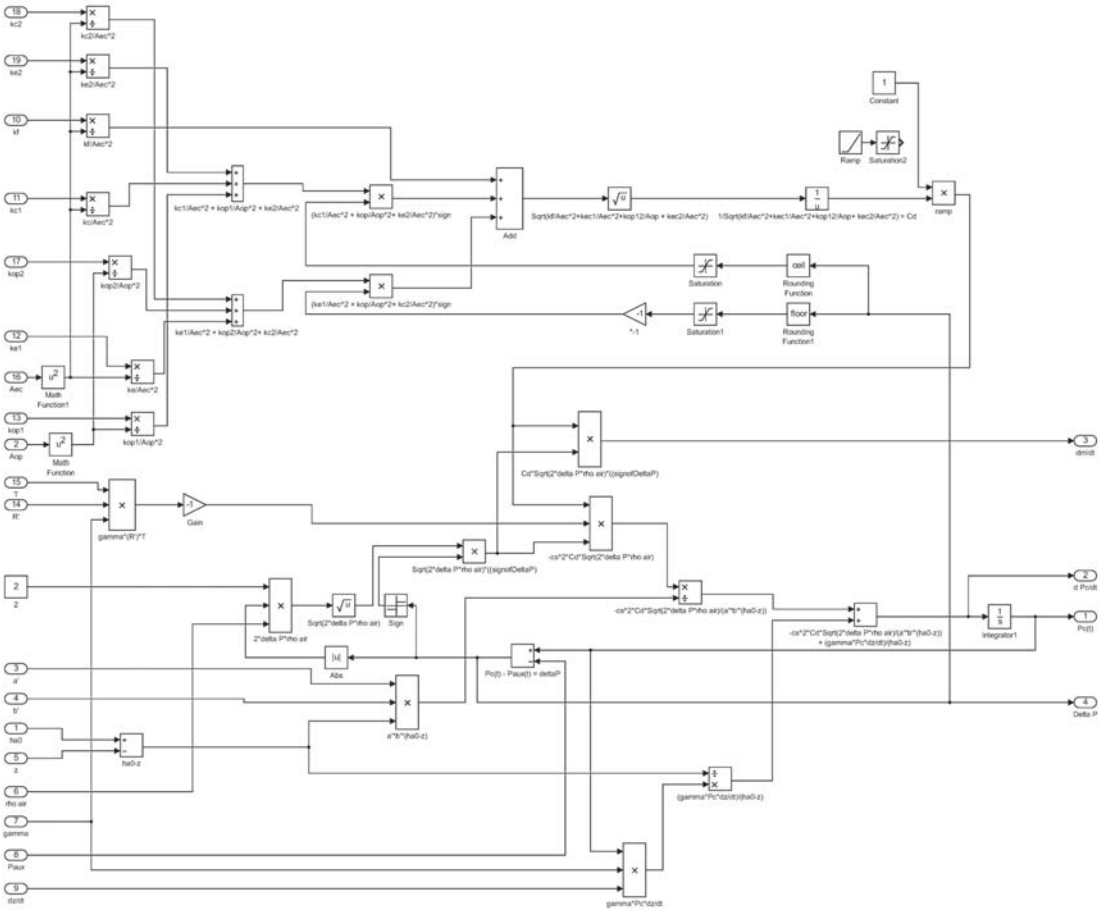

Figure B.6: Differential pressure model.

Submerged SWEC full model diagram

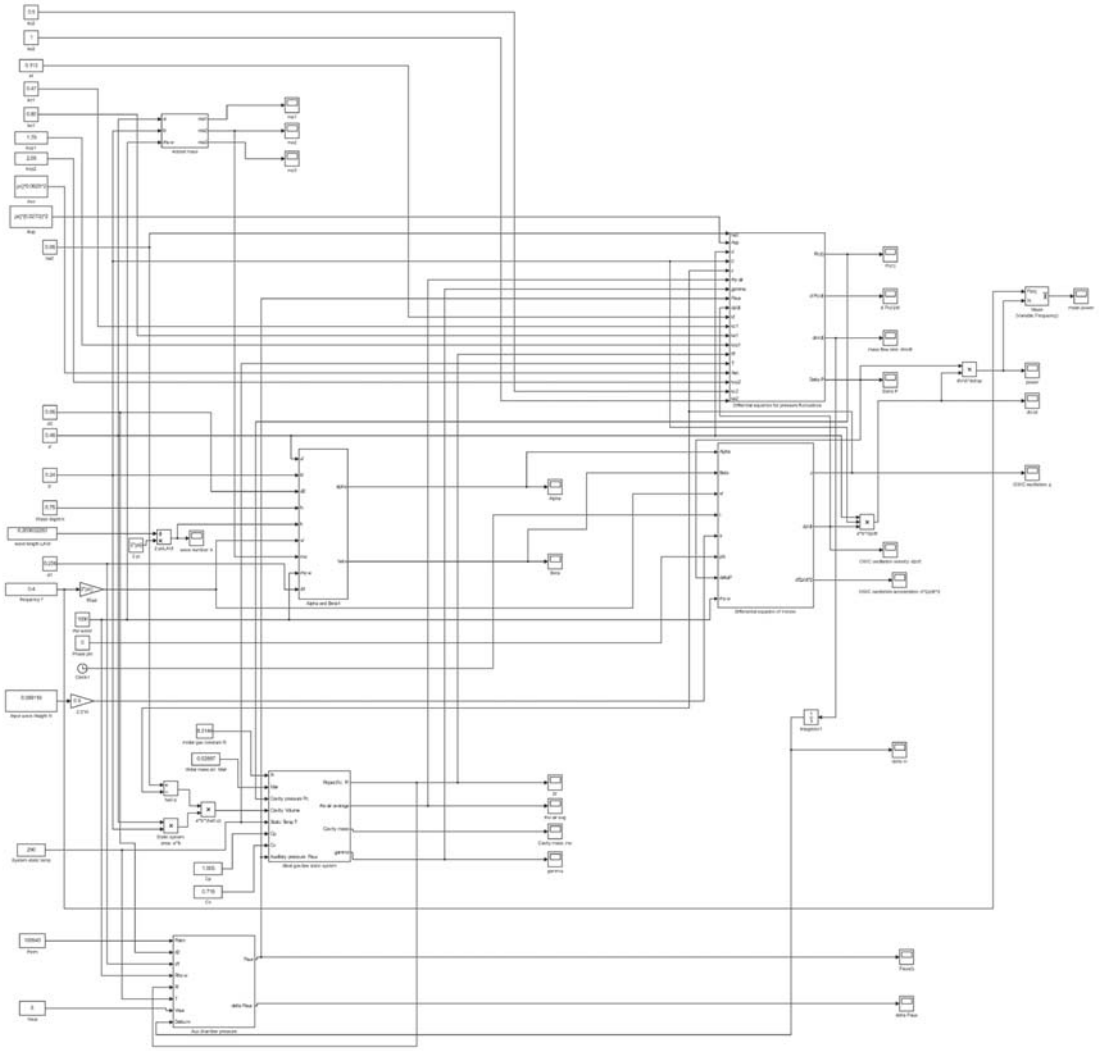

Figure B.7: Full simulation model diagram.

Appendix C

Matlab scripts and results

C.1 Matlab scripts

Real period return

'Real period return' was written with the aim of returning the average period of a set of waves. This was required in order to ensure that the wave being created by the wave paddle complied with the specified period. The script accessed the data recorded by the wave probe closest to the chamber and analysed the time between points in phase. The average period was then calculated and returned.

```
function period = RealPeriodReturn(num)
    c1=1;
    c2=1;
    timestamp=0;
    for t = 40:0.01:80.9
        count=round(t/0.01+1);

        if(sign(num(count,2))==-sign(num(count+1,2))&&num(count+1,2)<0)
            timestamp(c1)=t;

            if(c1>1)
                period(c2)=timestamp(c1)-timestamp(c1-1);
            end

            c1=c1+1;
        end

    end


period=mean(period);

end
```

Wavelength approximation

'Wavelength approximation' was written with the aim of numerically solving λ in Equation 3.8. This was done in efforts to produce a more accurate estimate for the wavelength, rather than using the less complex Equation 3.7. The wavelengths produced by this script are compared with actual recorded wavelengths, this comparison is presented in Section 3.2.

```
function waveLength = WaveLengthApproximator(f,h)
g=9.81;
T=1/f;
LAM=sqrt(9.81*h)*T;
inc=0.000001;
error=0.00001;

g*T^2/(2*pi())*tanh(2*pi()*h/LAM)-LAM;

while(abs(g*T^2/(2*pi())*tanh(2*pi()*h/LAM)-LAM)>error)

    if(abs(g*T^2/(2*pi())*tanh(2*pi()*h/(LAM+inc))-(LAM+inc))<abs(g*T^2/(2*pi())*tanh
        LAM=LAM+inc;
        g*T^2/(2*pi())*tanh(2*pi()*h/LAM)-LAM;
    else
        LAM=LAM-inc;
        g*T^2/(2*pi())*tanh(2*pi()*h/LAM)-LAM;
    end

end

error=g*T^2/(2*pi())*tanh(2*pi()*h/LAM)-LAM;
waveLength=LAM;
end
```

Inner chamber amplitude

A method was required to calculate the average amplitude of the inner chamber surface level. This was solved by writing the script 'Inner chamber amplitude' which assessed the chamber level recordings. 'Real period return' allowed the average amplitude to be calculated by analysing the difference in wave height between each consecutive crest and trough. The amplitude was calculated by dividing the difference in wave height by two.

```
clearvars
for x = 4:11

s1='';
s2=int2str(x);
s3='\0.5O5_' ;
s4='_ID1_Ch3_Channel 3.csv';
s5=horzcat(s1,s2,s3,s2,s4)
```

```
num=xlsread(s5,'D3:E15002');


T=RealPeriodReturn(num);
f=1/T;

phaseCount=1;


count=0;
probe1=0;
probe2=0;
phaseDif=0;
max1=0;
min1=0;
waveCount1=1;

t1=0;

for t = 40:0.01:120

        count=round(t/0.01+1);
        if(num(count,2)>max1)
            max1=num(count,2);
        end

        if(num(count,2)<min1)
            min1=num(count,2);
        end

        if(t1>T && t>40)
            waveHeight1(waveCount1)=max1-min1;
            max1=0;
            min1=0;
            waveCount1=waveCount1+1;
            t1=0;
        end

        t1=t1+0.01;


 end

A1=mean(waveHeight1)/2

end
```

Chamber height and power

'Chamber height and power' was written with the aim of accessing each test folder and its corresponding recorded channels in order to calculate the average converted power. Graphs of the volumetric flow rate and chamber height displacement were

also plotted. This was done by cycling through various concatenated string variables which enabled the script to automatically access each test folder and the recorded channels. The power was calculated by applying the corresponding calibration curve for each orifice plate and multiplying the volumetric flow rate by the differential pressure present.

```
clearvars
for y = 208:215
s1='';
s2=int2str(y);
s3='\0.5O5_' ;
s4='_ID1_Ch3_Channel 3.csv';
s5=horzcat(s1,s2,s3,s2,s4)

s6='_ID1_Ch5_Channel 5.csv';
s7=horzcat(s1,s2,s3,s2,s6);

s8='_ID1_Ch6_Channel 6.csv';
s9=horzcat(s1,s2,s3,s2,s8);

s10='_ID1_Ch7_Channel 7.csv';
s11=horzcat(s1,s2,s3,s2,s10);

num1=xlsread(s5,'D3:E15002');
num2=xlsread(s7,'D3:E15002');
num3=xlsread(s9,'D3:E15002');
num4=xlsread(s11,'D3:E15002');

vFlowEq =@(x)-0.193*abs(x/1000)^4+0.34*abs(x/1000)^3-0.206*abs(x/1000)^2+0.062*abs(x/1

for t = 0:0.01:149.99
   count=round(t/0.01+1);
   if(num2(count,2)>=0)
   vFlow(count)=vFlowEq(num3(count,2));
   else
   vFlow(count)=-vFlowEq(num4(count,2));
   end
   power(count)=abs(vFlow(count)*num2(count,2));
end


t = 0:0.01:149.99;

figure
subplot(2,1,1)
hold on
plot(t,num1(:,2));
title('Chamber height')
xlabel('t')
ylabel('m')

subplot(2,1,2)
plot(t,num2(:,2))
title('Delta P')
xlabel('t')
```

```
ylabel('Pa')

savefig('Chamber height and pressure')

figure
subplot(2,1,1)
plot(t,vFlow(:))
title('Volumetric flow rate')
xlabel('t')
ylabel('m^3/s')

subplot(2,1,2)
plot(t,power(:))
title('Power')
xlabel('t')
ylabel('W')

savefig('Chamber flow rate and power')
mean(power(4003:10003))
end
```

C.2 Experimental results

C.2.1 Transmissibility

Surface SWEC

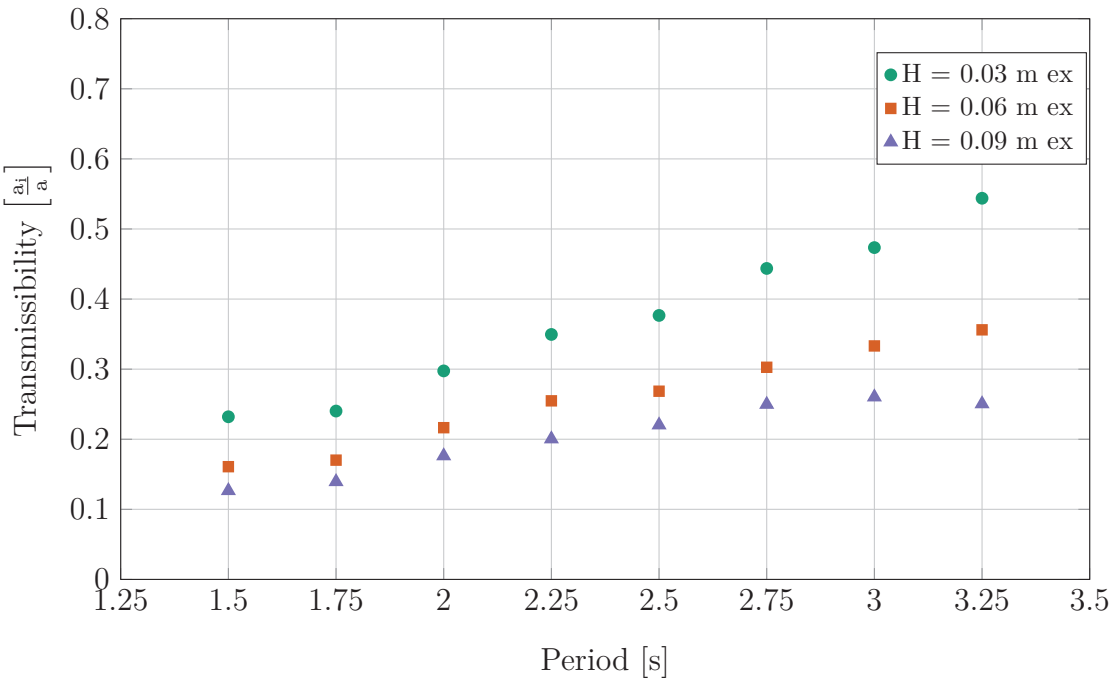

Figure C.1: Surface SWEC 0.14% orifice plate transmissibility.

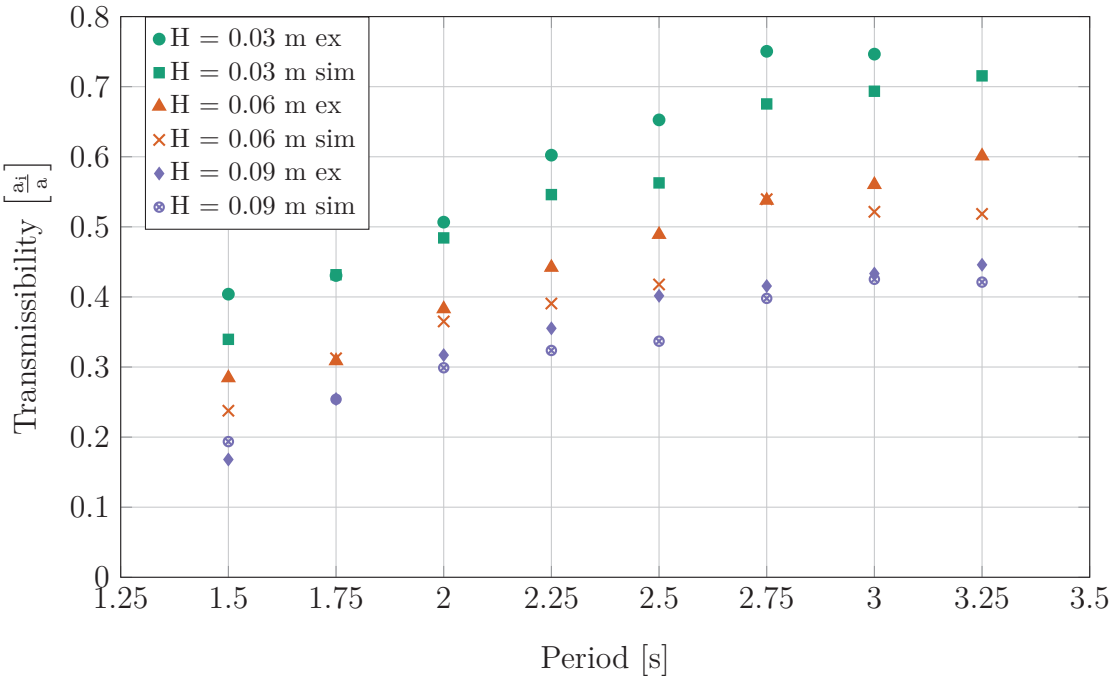

Figure C.2: Surface SWEC 0.25% orifice plate transmissibility.

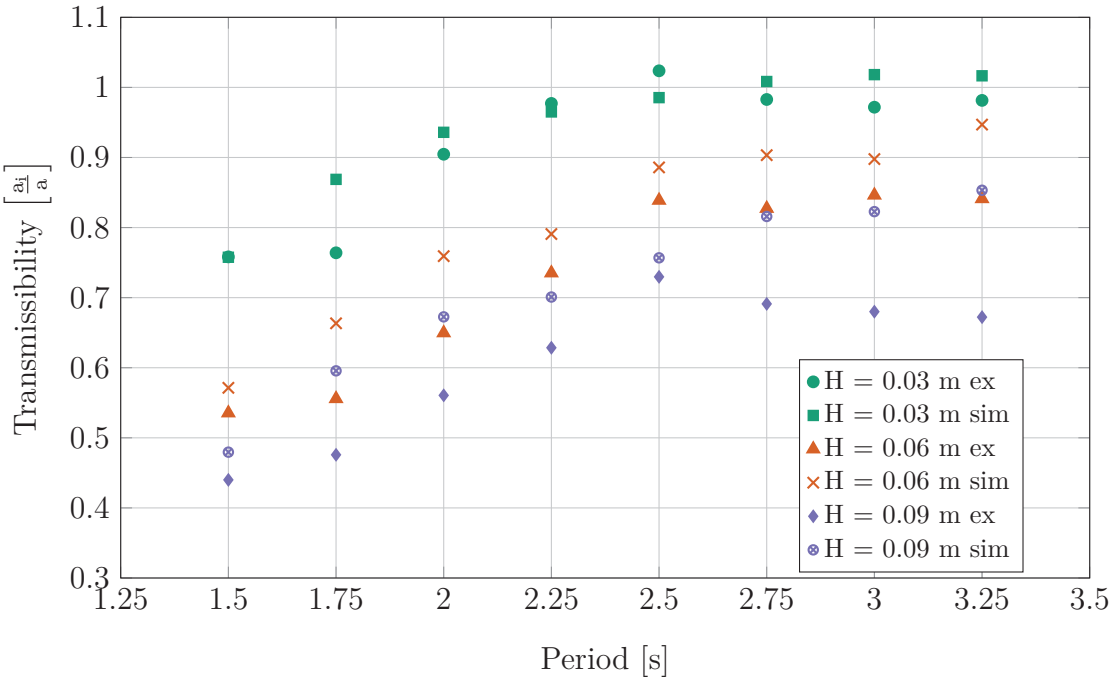

Figure C.3: Surface SWEC 0.5% orifice plate transmissibility.

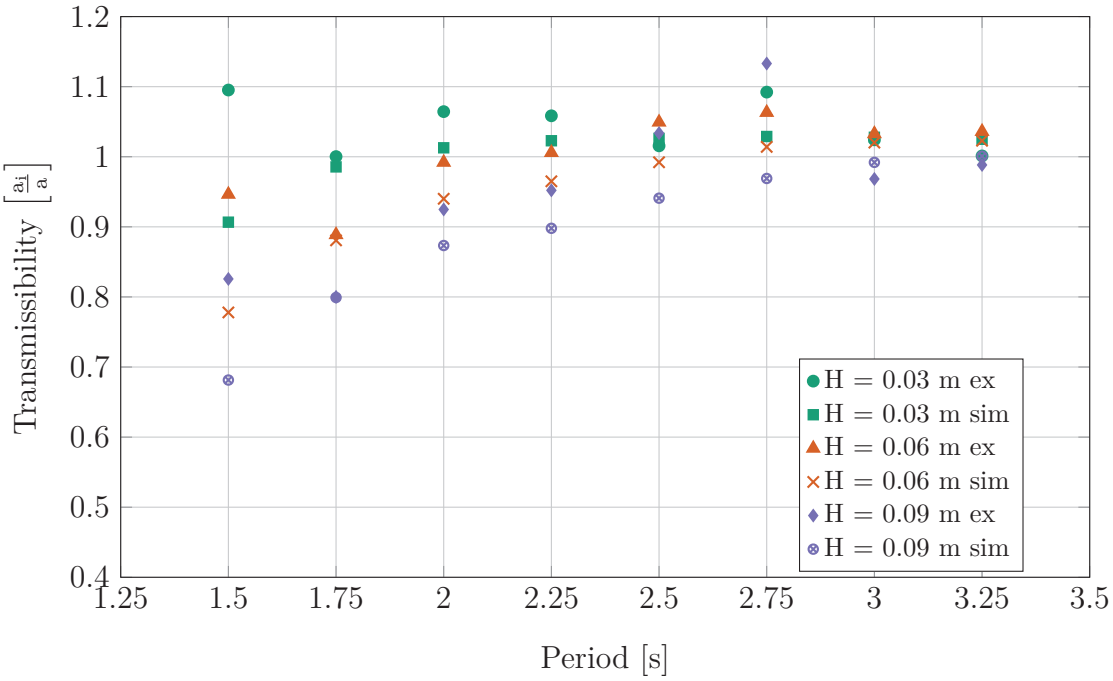

Figure C.4: Surface SWEC 1% orifice plate transmissibility.

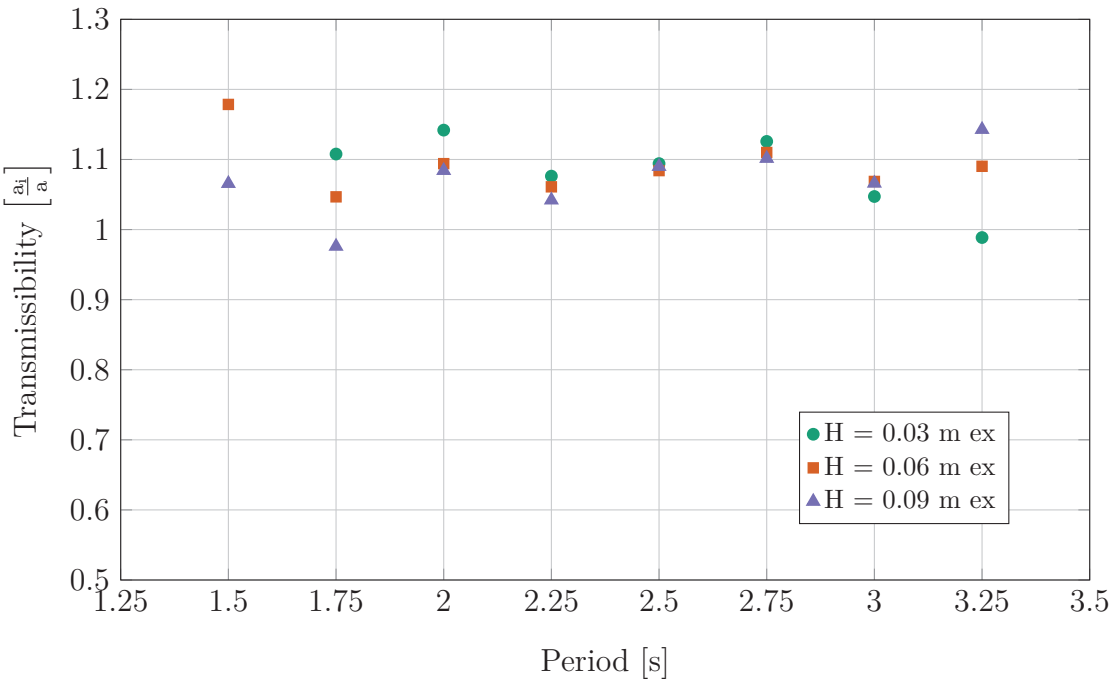

Figure C.5: Surface SWEC 1.5% orifice plate transmissibility.

Submerged SWEC

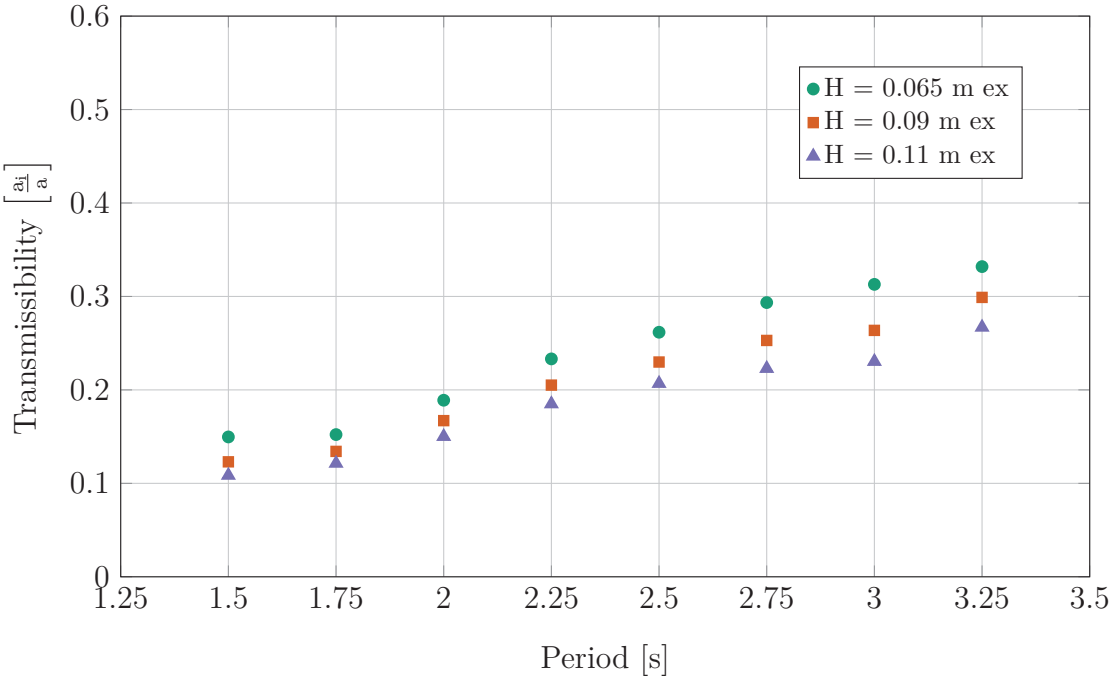

Figure C.6: Submerged SWEC 0.14% orifice plate transmissibility.

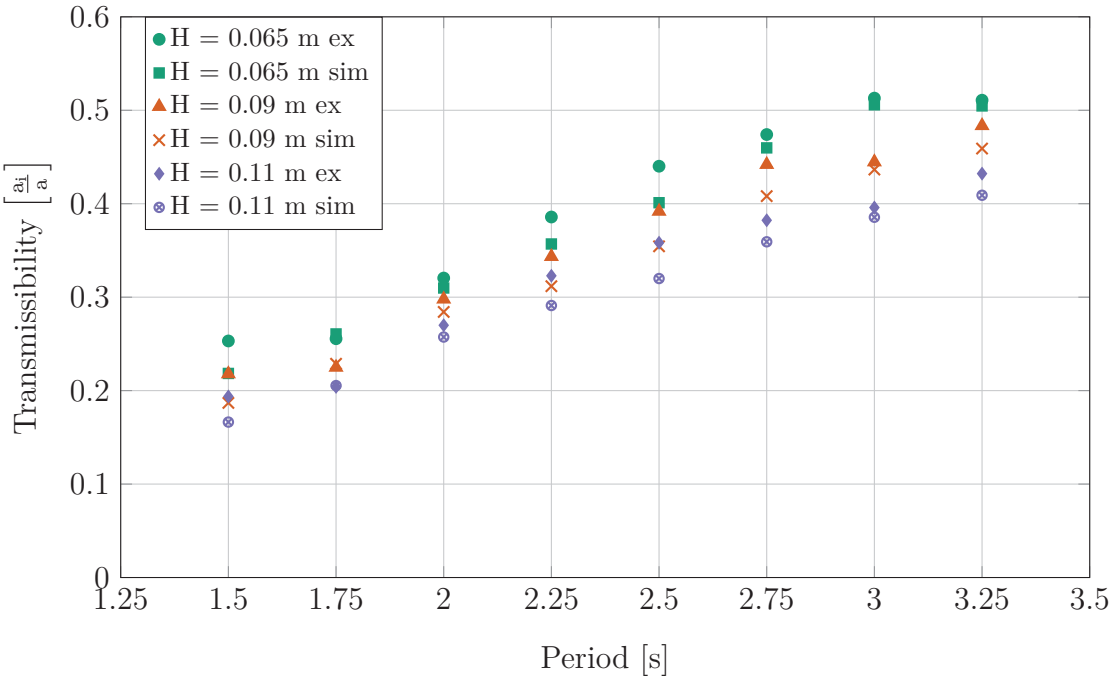

Figure C.7: Submerged SWEC 0.25% orifice plate transmissibility.

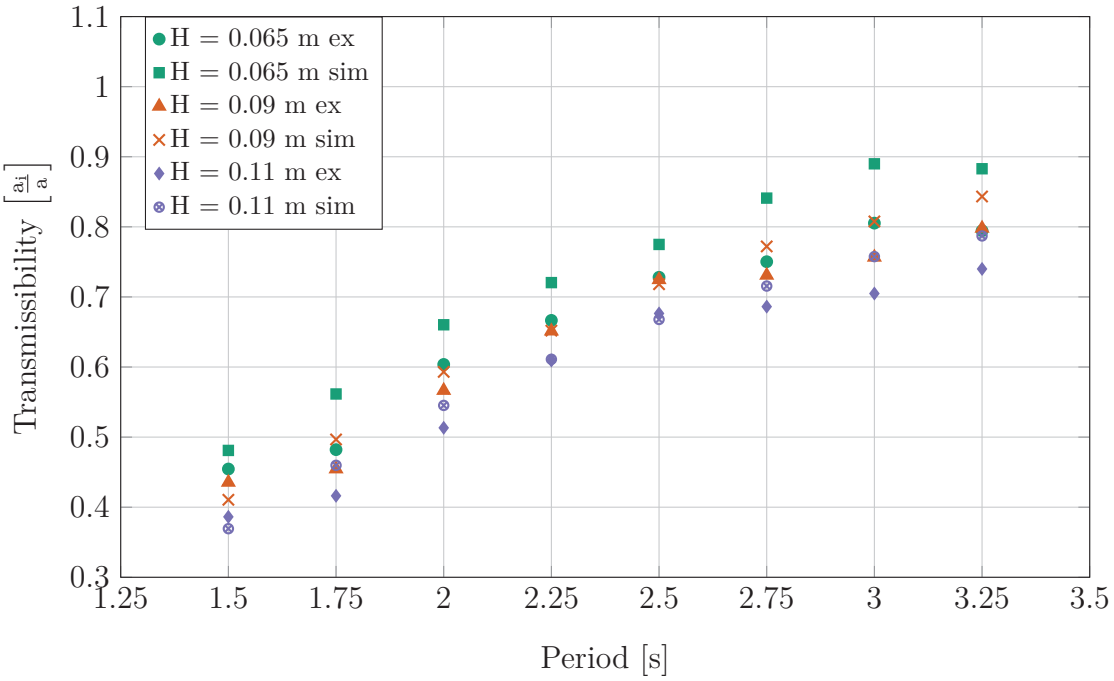

Figure C.8: Submerged SWEC 0.5% orifice plate transmissibility.

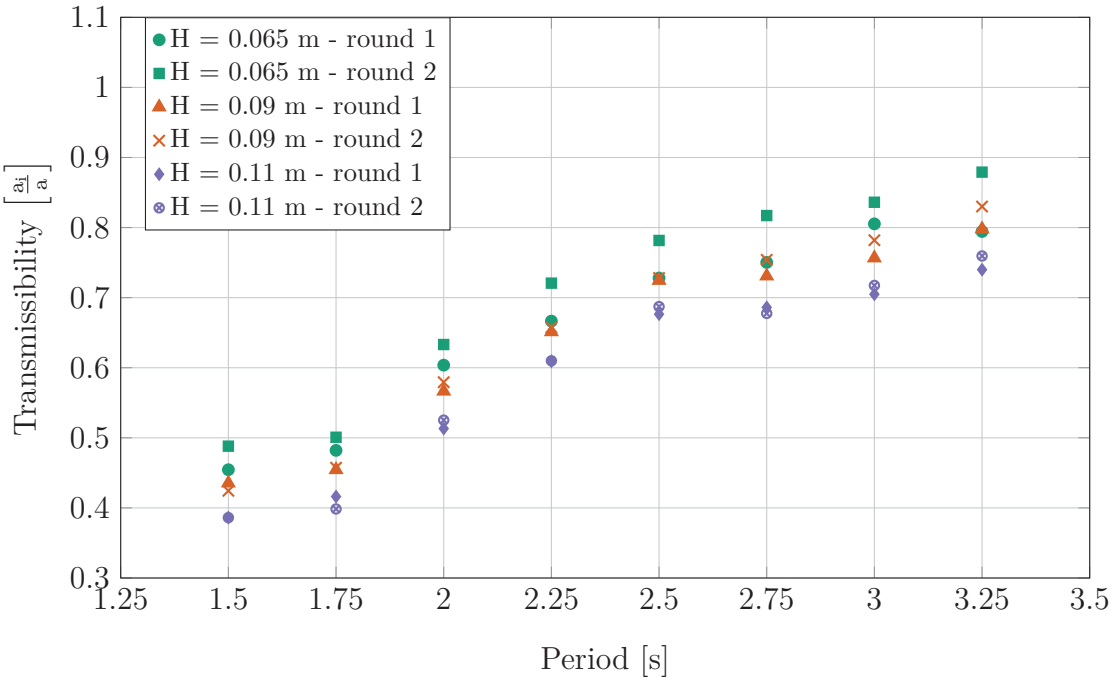

Figure C.9: Submerged SWEC 0.5% orifice plate transmissibility repeatability test.

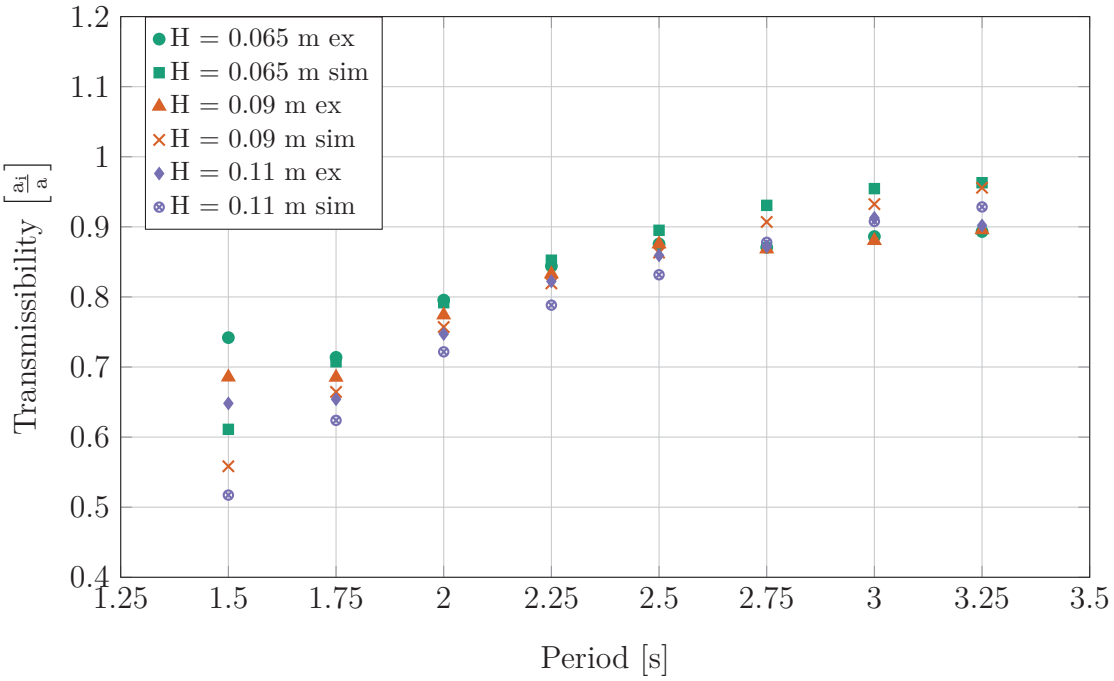

Figure C.10: Submerged SWEC 1% orifice plate transmissibility.

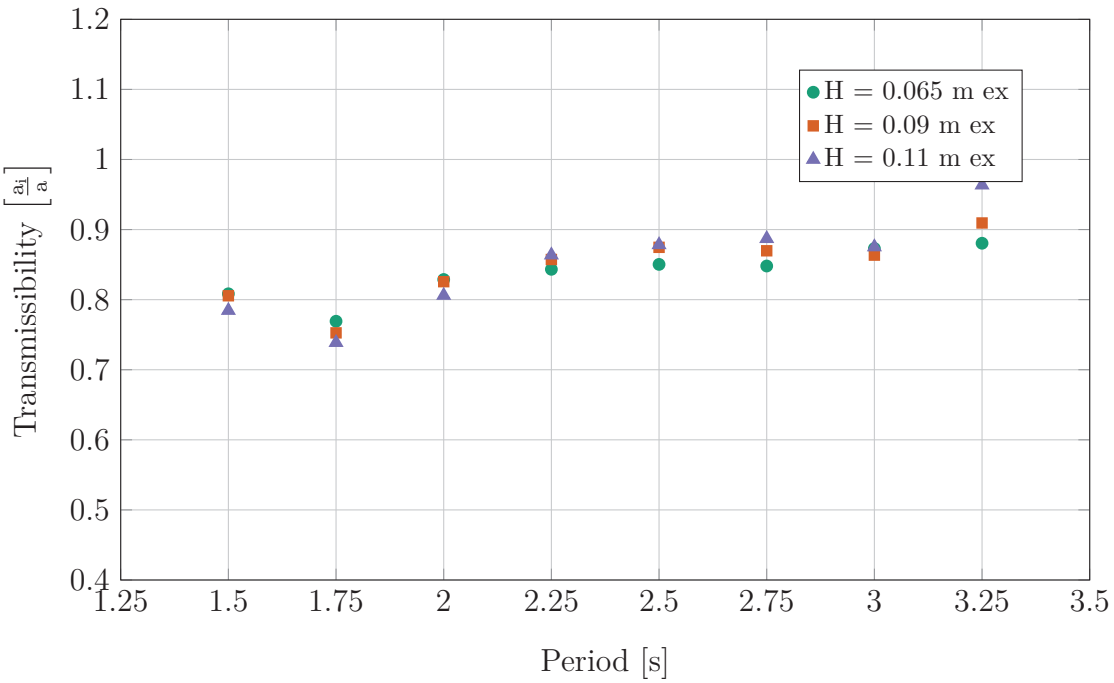

Figure C.11: Submerged SWEC 1.5% orifice plate transmissibility.

C.2.2 Conversion efficiency

Surface SWEC

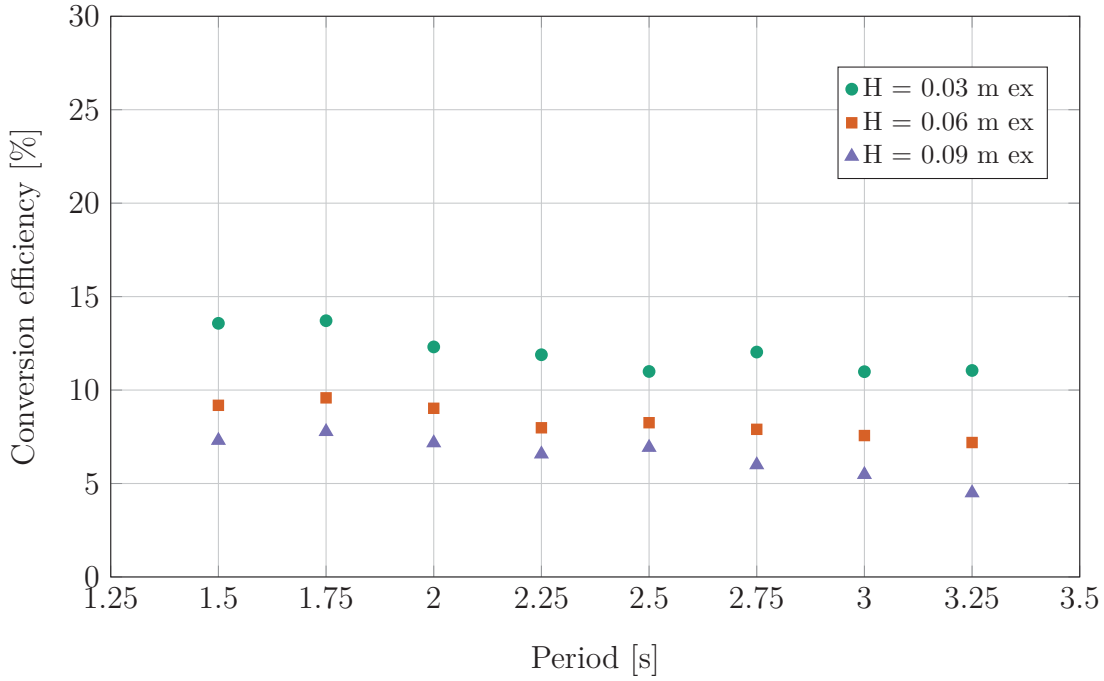

Figure C.12: Surface SWEC 0.14% orifice plate conversion efficiency.

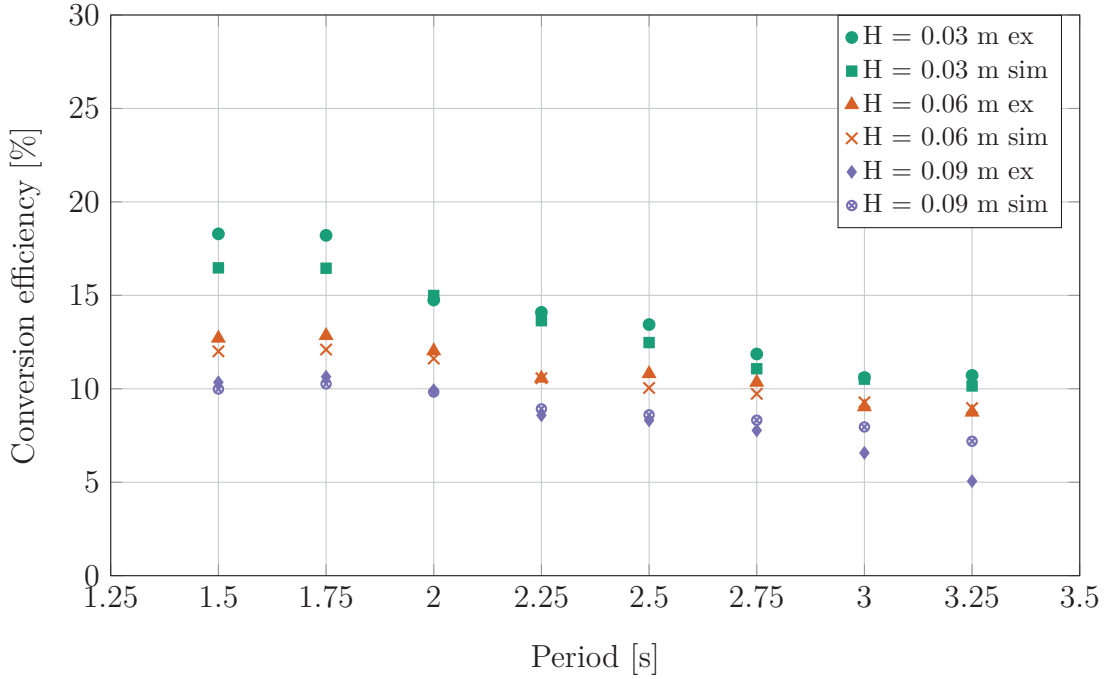

Figure C.13: Surface SWEC 0.25% orifice plate conversion efficiency.

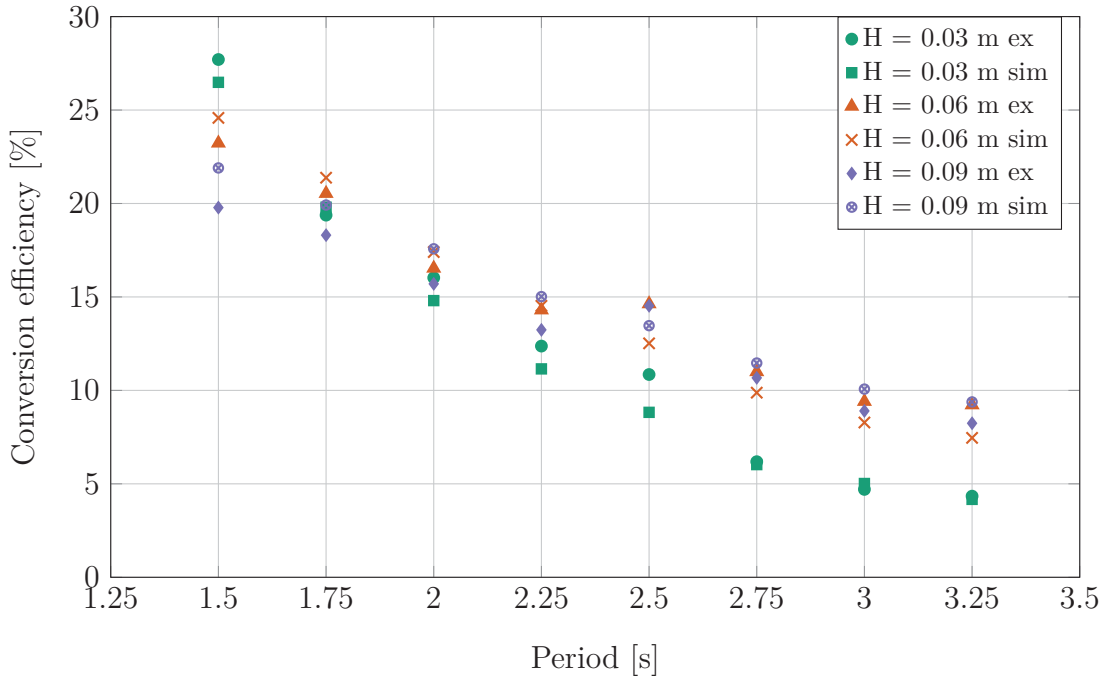

Figure C.14: Surface SWEC 0.5% orifice plate conversion efficiency.

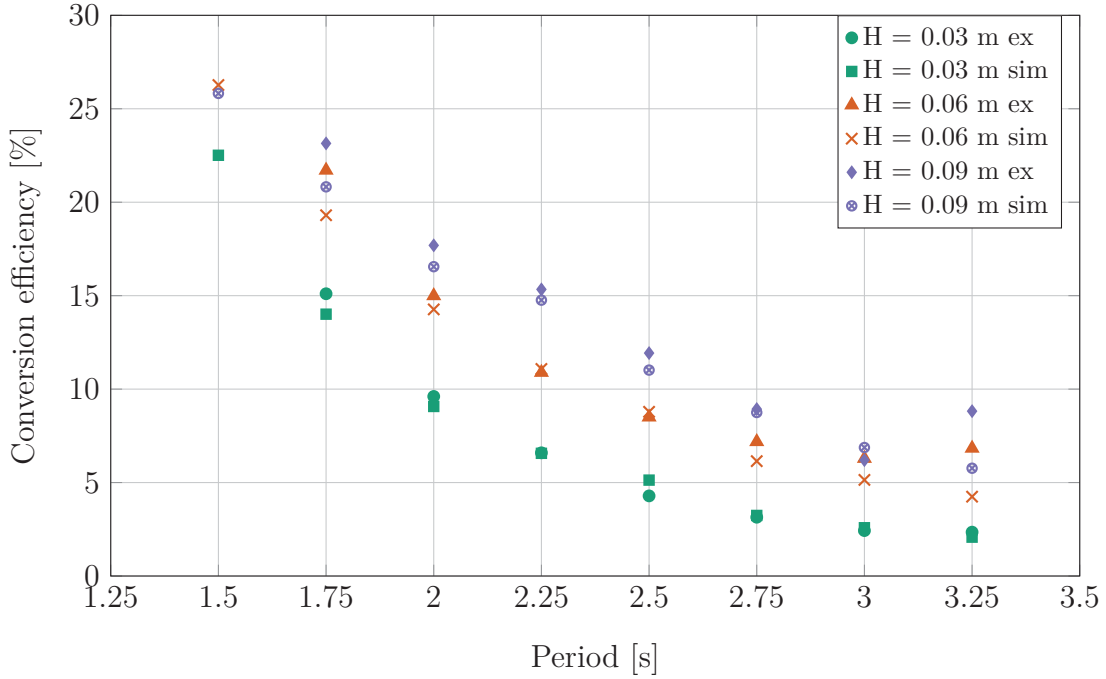

Figure C.15: Surface SWEC 1% orifice plate conversion efficiency.

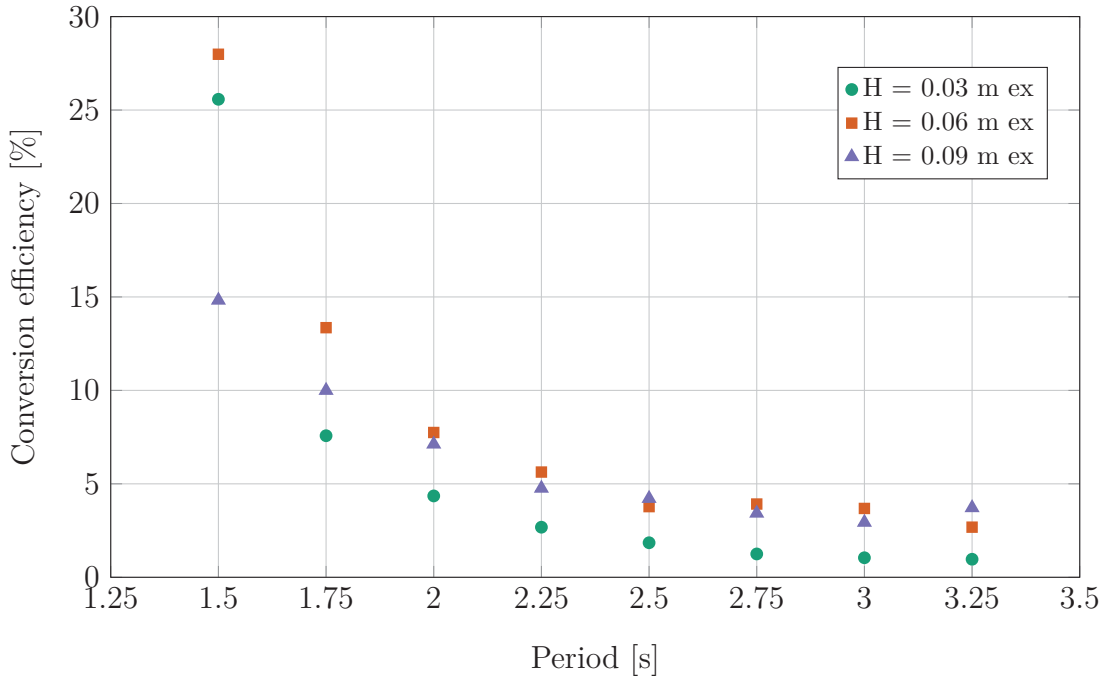

Figure C.16: Surface SWEC 1.5% orifice plate conversion efficiency.

Submerged SWEC

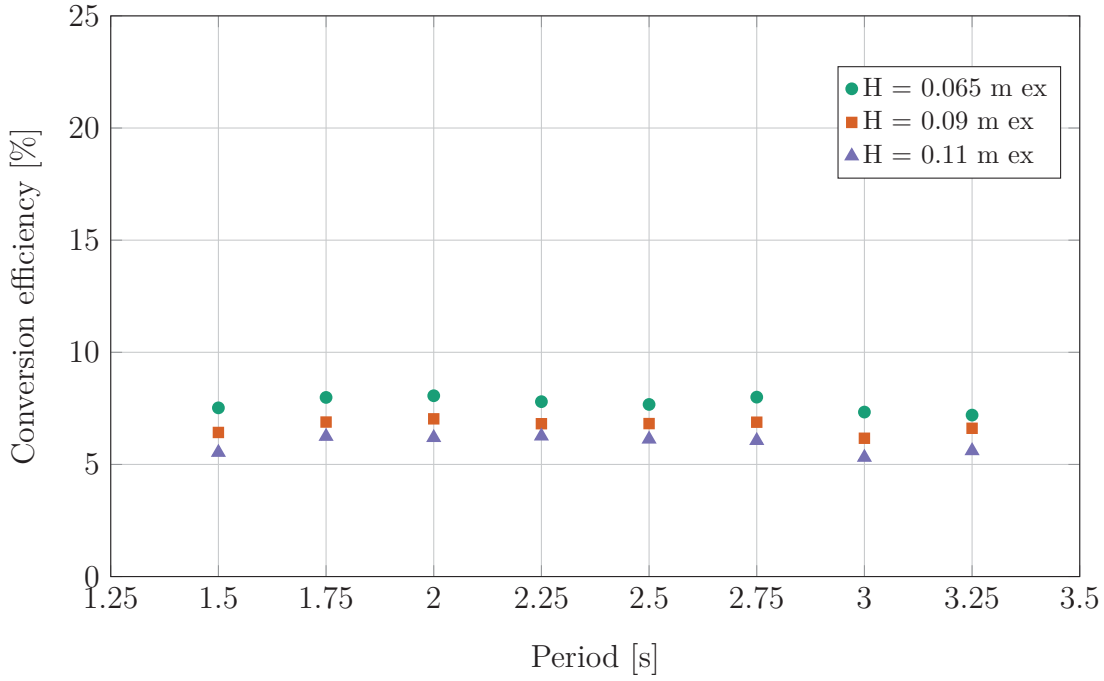

Figure C.17: Submerged SWEC 0.14% orifice plate conversion efficiency.

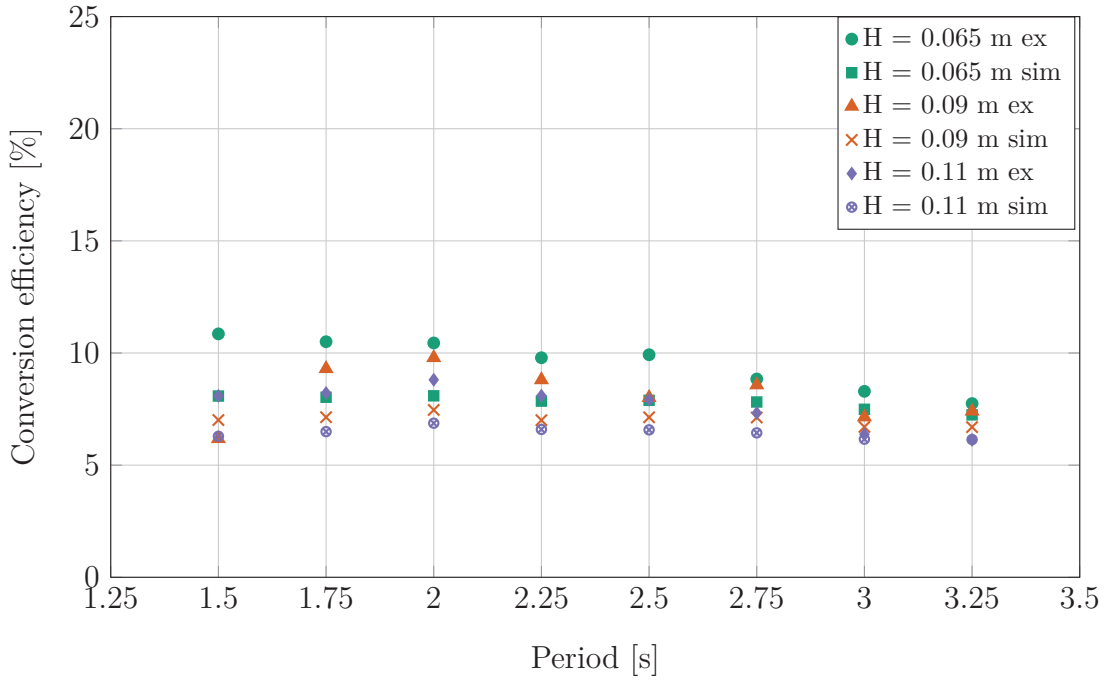

Figure C.18: Submerged SWEC 0.25% orifice plate conversion efficiency.

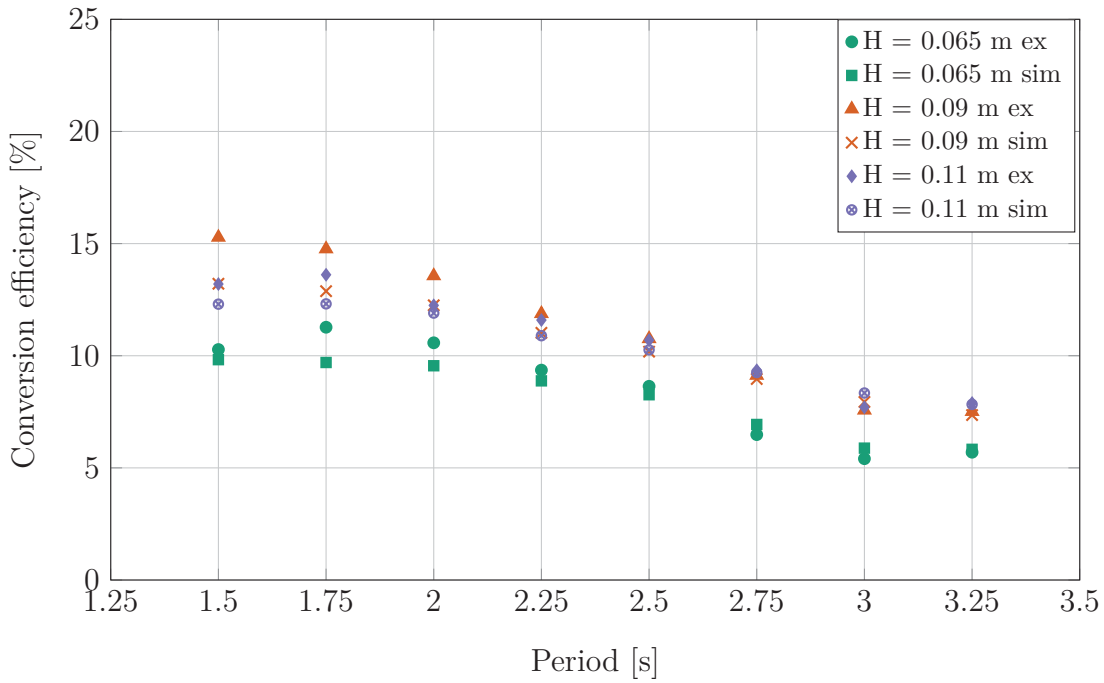

Figure C.19: Submerged SWEC 0.5% orifice plate conversion efficiency.

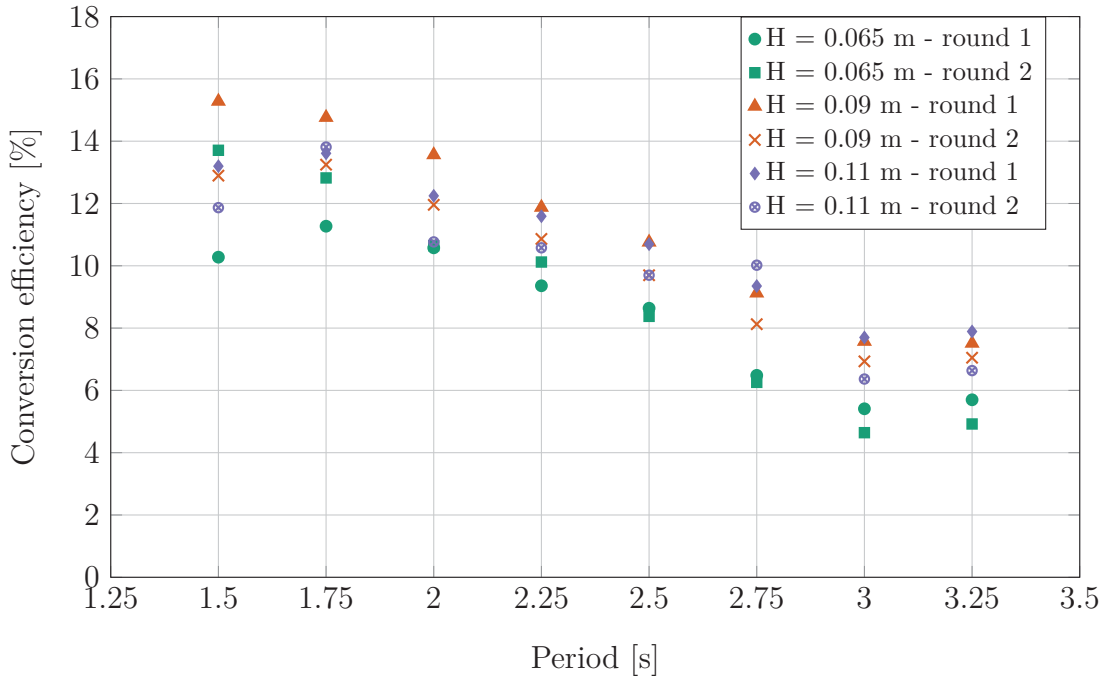

Figure C.20: Submerged SWEC 0.5% Orifice plate conversion efficiency - repeatability test.

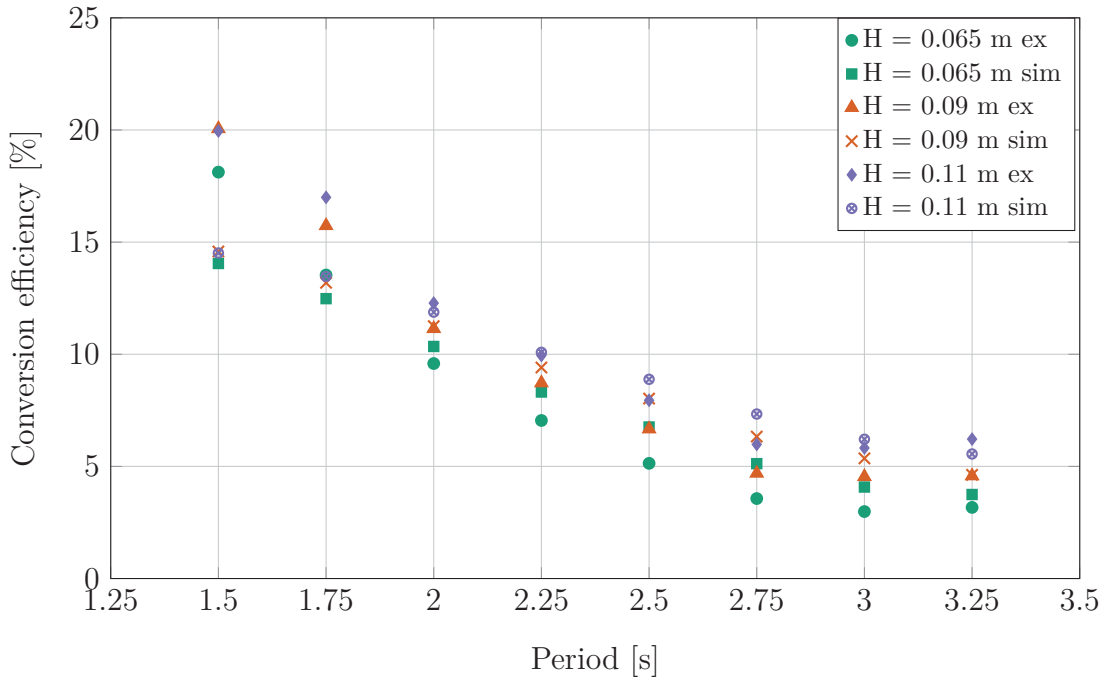

Figure C.21: Submerged SWEC 1% orifice plate conversion efficiency.

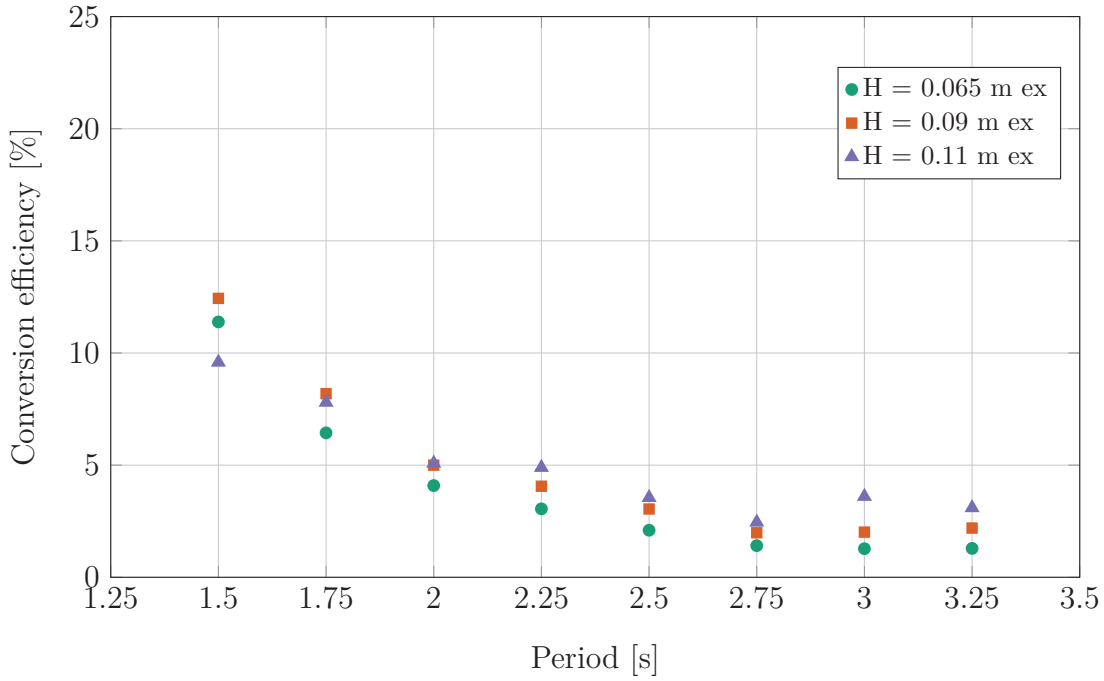

Figure C.22: Submerged SWEC 1.5% orifice plate conversion efficiency.

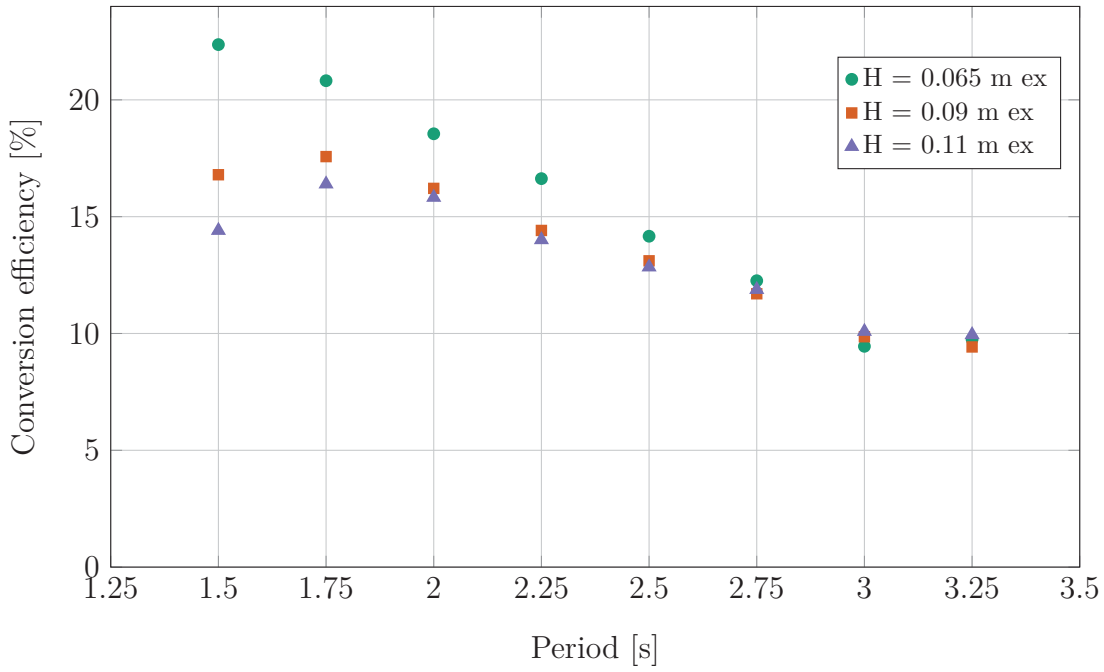

Figure C.23: Submerged SWEC 0.5% orifice plate conversion efficiency orientation 2.

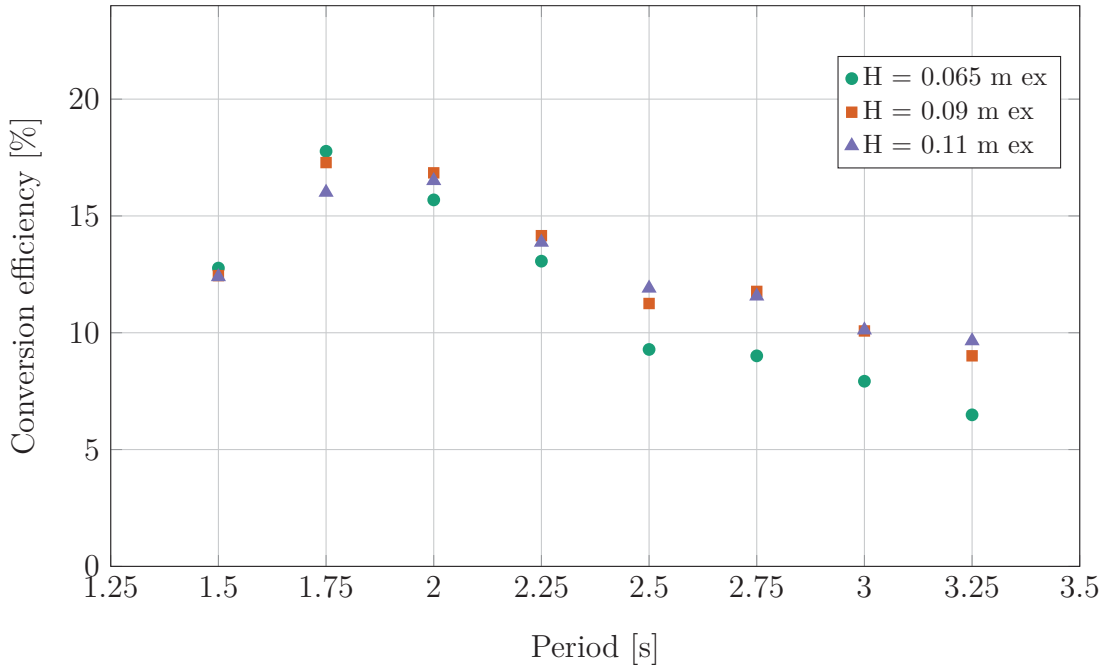

Figure C.24: Submerged SWEC 0.5% orifice plate conversion efficiency orientation 3.

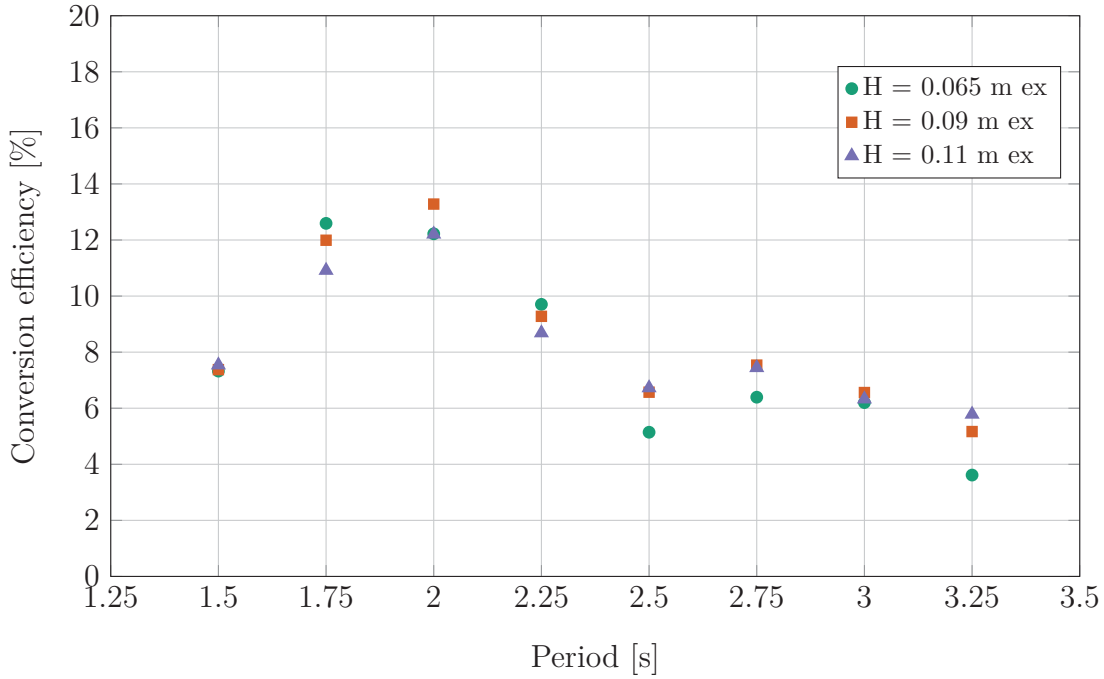

Figure C.25: Submerged SWEC 0.5% orifice plate conversion efficiency orientation 4.

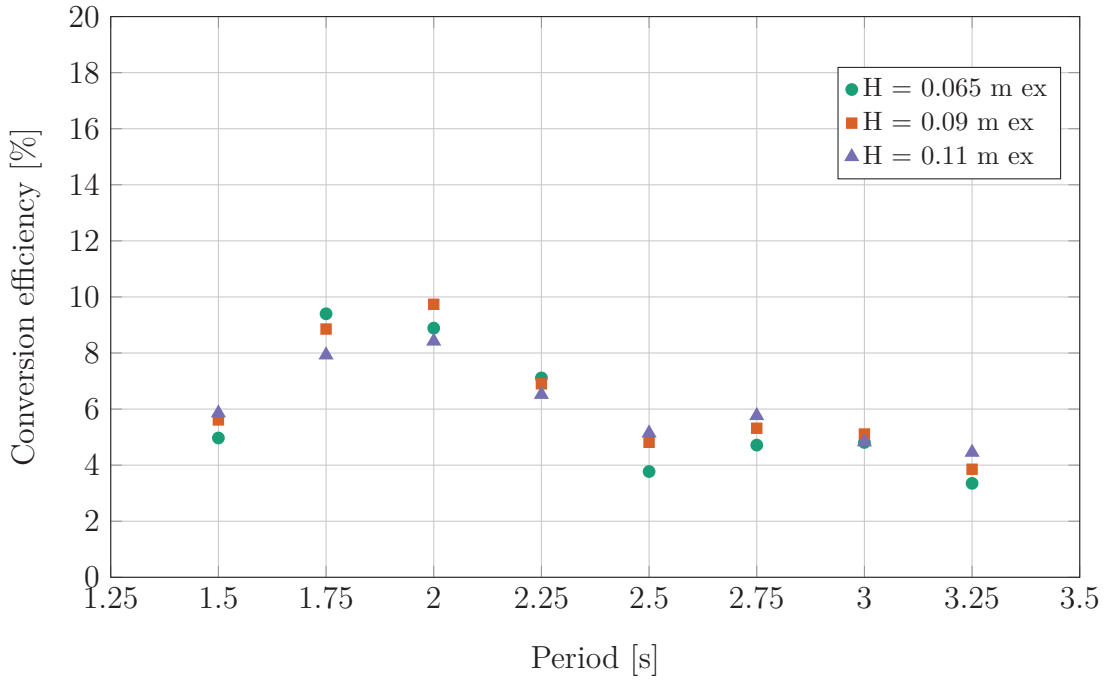

Figure C.26: Submerged SWEC 0.5% orifice plate conversion efficiency orientation 5.